The geometry and mechanics of wrinkling patterns in biological plywoods and cholesteric liquid crystals

Ziheng Wang

Master of Engineering

Department of Chemical Engineering

McGill University

Montréal, Québec

October 10, 2019

A thesis submitted to McGill University in partial fulfillment of the requirements of the degree of Master of Engineering

DEDICATION

To my parents and my beloved family for their unconditional love.

ACKNOWLEDGEMENTS

I would like to express my gratitude to my supervisors Dr. Alejandro D. Rey and Dr. Phillip Servio for their guidance and help in both academic research and daily life. Their kindness and patience helped me during all the time I spent in Montréal. It was an honor for me to be supervised by two of the greatest professors in the world. I would also like to thank my group members Jonathan Monahan, Oscar Matus Rivas, Samuel Mathews, Sayyed Ahmad Khadem, Shaden Daghash, Sina Mirzaeifard and Thomas Vlasic for their help and bringing so much memorable moments to our MMRG lab. I wish to acknowledge the Naturals Science and Engineering Research Council of Canada (NSERC) for the grant and Compute Canada for computational resources and technical support. In the end, I would like to thank all my friends for making my life in Montréal full of fun, and my precious family, especially my beloved mother, and Michaël Massussi, for being the light of my life.

ABSTRACT

Biological plywoods are multifunctional fibrous composites materials found in plants (cellulosic), insect cuticles (chitin) and bones and cornea tissues in mammals (collagen). Despite the different precursors' biochemistries of nature's fibrous composites, the rigidity, chirality and large length-to-diameter aspect ratio of the fibres produces architectures analogous of those of chiral liquid crystals. A biomimetic pathway to multifunctional synthetic plywoods must then be based on nature's green manufacturing based on liquid crystal self-assembly. Fruitful past work focused on mechano-optical functionalities arising from the 3-D bulk plywood structures. In this thesis, we focus on theory and simulation of surface nanostructuring of chiral liquid crystalline precursors for emerging potential optical, tribological, and mechanical functionalities. The goal and scope of this thesis is to reveal and characterize the fundamental mechanisms that control the emergence of nano-wrinkling as chiral liquid crystals assemble at free surface with the ultimate goal of reproducing nature's multiscale wrinkles surfaces such as lotus leaves, beetle exocuticles, tulip petals, and sharkskin using self-assembly at ambient temperatures and water-based solvents. Taken together with the new results presented in this thesis show how surface self-assembly in soft matter, chirality, and anchoring create simple and multiple wrinkling with active surface stress fields, of interest to biomimetics of nature's functional surfaces.

ABRÉGÉ

Les composés fibreux ordonnés biologiques sont des matériaux multifonctionnels trouvés dans les plantes (cellulose), cuticules d'insectes (chitine) et dans les ossements et cornée chez les mammifères (collagène). Malgré les différentes réactions biochimiques des précurseurs des composés fibreux présentes dans la nature, la rigidité, la chiralité et le rapport élevé entre la longueur et le diamètre des fibres produisent des architectures semblables à celles des cristaux liquides chiraux. Un parcours biomimétique menant à des composés fibreux ordonnés synthétiques multifonctionnels doit être basé sur l'auto-assemblage de cristaux liquides tel qu'observé dans la nature. Les travaux passés portent sur les fonctions mécano-optiques des structures composites fibreuses en trois dimensions. Cette thèse se penche plutôt sur la théorie et la simulation des nanostructures de surfaces de précurseurs de cristaux liquides chiraux, avec regard sur les possibles fonctions optiques, tribologiques et mécaniques. Elle cherche à révéler et caractériser les mécanismes fondamentaux qui contrôlent l'émergence de nano-rides lors de l'assemblage de cristaux liquides chiraux à surface libre, dans le but de reproduire les surfaces à rides à échelles multiples se trouvant dans la nature, tel que les fleurs de lotus, les exocuticules de coccinelle, les pétales de tulipe ainsi que la peau de requin, utilisant des techniques d'auto-assemblage à température ambiante avec solvants à base d'eau. Les résultats présentés dans cette thèse montrent de quelles façons l'auto-assemblage de surface en matière molle, chiralité et ancrage créer des rides simples et multiples ainsi que des champs de contraintes sur les surfaces actives.

Contribution of Authors

This is a manuscript-based thesis consisting of two journal articles, whose title, name of the authors and their contributions are:

(1) **Surface Anchoring Effects on the Formation of Two-Wavelength Surface Patterns in Chiral Liquid Crystals.**

Ziheng Wang, Pardis Rofouie and Alejandro D. Rey[a)]

[a)]Department of Chemical Engineering, McGill University, 3610 University Street, Montreal, QC H3A 2B2, Canada;

Crystals (Open Access), 2019, **9**, 190 DOI Link

Author contributions:

Ziheng Wang: Derived the shape equation and capillary model equations, made the graphs and wrote the manuscript.

Pardis Rofouie: Wrote the introduction and conclusion, revised the graphs and paper.

Alejandro D. Rey: Derived the governing equation, derived the linear model approximation, revised the paper and supervised the whole project.

(2) **Mechano-Geometry of Nano-wrinkling in Cholesteric Liquid Crystal Surfaces.**

Ziheng Wang, Phillip Servio and Alejandro D. Rey[a)]

[a)]Department of Chemical Engineering, McGill University, 3610 University Street, Montreal, QC H3A 2B2, Canada;

Article under review

Author contributions:

Ziheng Wang: Derived the equations and completed the proofs, made the graphs and wrote the manuscript.

Phillip Servio: Revised the manuscript and co-supervised the whole project.

Alejandro D. Rey: Derived the governing equations, revised the paper and supervised the whole project.

TABLE OF CONTENTS

LIST OF TABLES

LIST OF FIGURES

Figure page

CHAPTER 1
Introduction

1.1 Introduction

Biological plywoods such as cellulosics, chitin and collagens are multifunctional fibrous composite materials ubiquitous in nature. Biological plywoods have the same architecture as cholesteric liquid crystals and are chiral at the macroscopic scale. Currently, intense efforts to biomimicry of these bulk and surface structures are being made using various in-vitro materials and processes.

For example, collagen-based plywoods are biocompatible materials which have high potential in tissue engineering applications, which are often used as the substrate for nurturing cell tissues [1]. The growth of cell tissue is not only a function of the temperature and pressure, but also highly depends on the geometry and mechanical behaviour of the substrate [2]. Especially, high curvature regions usually correspond to high surface tension, thus promoting the growth of cells, which reduces the production time for tissue engineering or even drive reversible transition between cells [3, 4]. Using this property, it is possible to control the growth of cells by manipulating the geometry of the surface [5].

Beside surface tension, whose direction is along the surface tangent, the surface bending stress also shows influences on the growth of cells. Combining stretching and bending stresses, which is shown in Fig. 1–1, a designed substrate with certain geometry can contain rich mechanical stress information of both stretching and

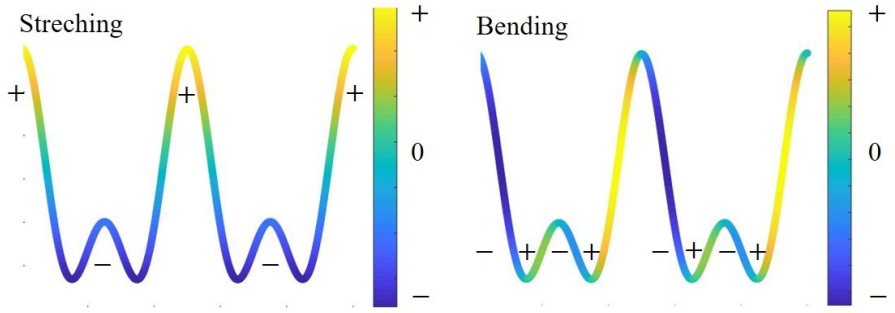

Figure 1–1: Example of stress behavior on a sinuous surface profile found in the simulations of this thesis. The color represents the intensity of stress whose magnitude is shown as the color bar on the right. The sign of stretching stress represents shrinkage or expanding behavior, and that of bending stress represents bending upwards or downwards. The figure clearly demonstrates that co-existing complex wrinkling and rich stress fields create functional substrates for tissue engineering.

bending stress, offering rich possibilities to be utilized in tissue engineering. Hence, understanding the geometry and the mechanics of wrinkling patterns in biological plywoods helps scientists to design and apply the wrinkled surface of biocompatible materials as a compatible substrate in tissue engineering. Many other potential surface functionalities of plywoods and liquid crystals are identified throughout the thesis.

1.2 Biological Plywoods

The biological plywood fibre architecture has a twisted structure which can be ubiquitously observed in many organics such as the chitin crystallites of insects, collagen in tendons and skin [6]. Fig. 1–2 shows the collagen fibrils and fibril bundles observed in rat lamellar bone. We can see that the alignment of fibrils shows a preferred orientation, whose directions are represented by arrows in Fig. 1–2(a).

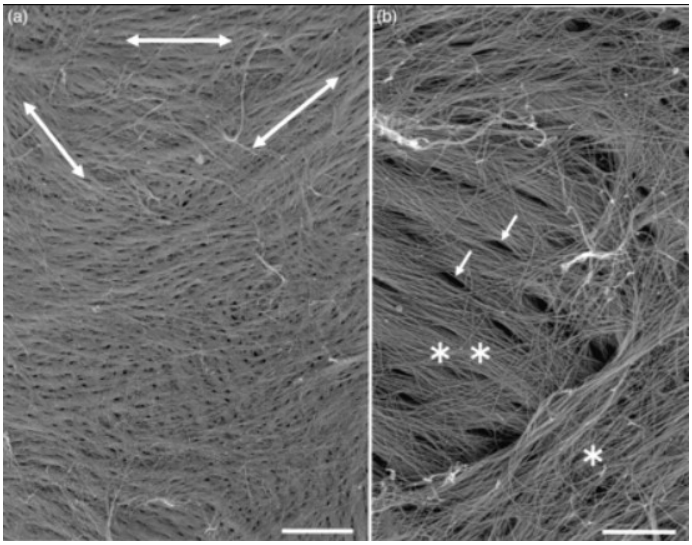

Figure 1–2: Scanning electron micrographs of the inner bone surface, where (a) shows how collagen fibrils and fibril bundles are aligned in similar directions (arrows, scale bar: 10 µm) and (b) loosely assembled fibrils (∗) cover the fibril bundles (∗∗), leaving oval pores (arrows, scale bar: 2 µm). Adapted with permission from ref. [7].

These fibrils and fibrils bundles interweave with each other, and form the complex structure in large scale, allowing them to exhibit unique properties.

This twisted structure can be described by the helicoidal model, which allows the plywood to be analyzed accurately thus further can be utilized via a biomimetic approach [8]. The concept of twisted plywood structure is naturally linked to cholesteric liquid crystals [6].

1.3 Cholesteric Liquid Crystals

The biological plywoods found in nature are solid analogues of cholesteric liquid crystals and liquid crystallinity is a precursor state of these nature's composites. The molecules of liquid crystals are rod-like molecules. The preferred macroscopic orientation of the molecules is known as director field $\mathbf{n}$, which is a unit vector. The

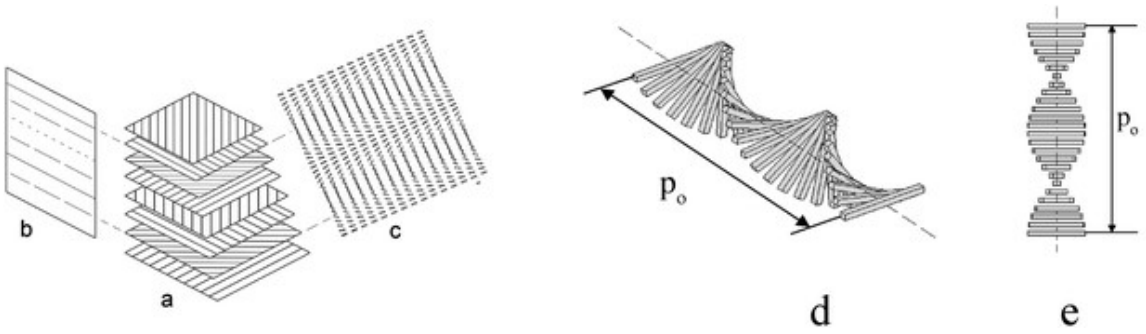

Figure 1–3: Periodic structure of cholesteric liquid crystal in different cross-sectional planes (a,b,c) and viewing angles (d,e). P_0 is the micron-range helix pitch representing the length scale of the periodicity of CLCs. The sign of P_0 can be $+$ or $-$. Adapted with permission from ref. [11].

director field can be a function position vector $\mathbf{x}$. There are three types of liquid crystals: nematics, cholesterics and smectics. For spatially homogeneous nematic liquid crystals, the director field $\mathbf{n}$ is a constant, which does not depend on $\mathbf{x}$. In contrast, cholesteric liquid crystals (CLCs) have a periodic director field $\mathbf{n} = \mathbf{n}(\mathbf{x})$, such that display macroscopic chirality. The cholesteric liquid crystal organization can be widely found in nature such as in plywoods and collagens, and this periodic configuration allows CLCs to have some unique properties such as optical [9] and tribological response [10].

The unique periodic configuration of cholesterics is characterized by the orientation of the helix vector and the pitch (periodicity) length P_0, which is shown in Fig. 1–3. The sign of pitch P_0 represents the handedness $(+/-)$ and is dependent on chemical and electromagnetic fields. It gives the possibility to be the source of a rich sensor/actuator capabilities [12]. In this thesis, we show that the periodic director field of cholesteric liquid crystals is the cause of surface wrinkling.

1.4 Wrinkling in Nature

Surface wrinkling plays an important role in determining materials properties, such as optical, tribological and mechanical. Biomimicking nature's wrinkled surfaces is a very active area of research. It can be observed not only on the surface of tulip epoxy casts [13], but also on the surface of microspheres [14] and others [15, 16]. Fig. 1–4 shows the wrinkled surface found in tulip epoxy casts. We can observe that in Fig. 1–4(c) there exists a pretty flat bottom region, which can be predicted by the model we develop and solve in this thesis. Different processes are used to create wrinkling, typically using high temperatures/pressures, and aggressive solvents. In this thesis, we simulate wrinkling processes using phenomena and mechanisms close to those used in natures plywoods, such as by chiral liquid crystal self-assembly, which occurs at ambient temperature and pressure conditions, in water-based solvents.

The interface between liquid crystal and air has a large impact on director field [17], which is the well-known anchoring phenomenon. Surface anchoring is a material surface property with a range of practical applications such as optical control [18]. Surface anchoring is an effect that generates preferred surface orientation to minimize or lower the interfacial energy. The anchoring energy is the anisotropic component of the surface energy and is usually 10% of the magnitude of the isotropic contribution of the surface energy. In this thesis, we show that nano-wrinkling is the results of the product of the ratio of these two energies (approximately equal to 0.1) and the internal length scale of the material (chiral pitch P_0) which is in the micron range. In this thesis, we show that even if anchoring is significantly lower than surface tension, it is sufficiently strong to creates nano-folds during self-assembly.

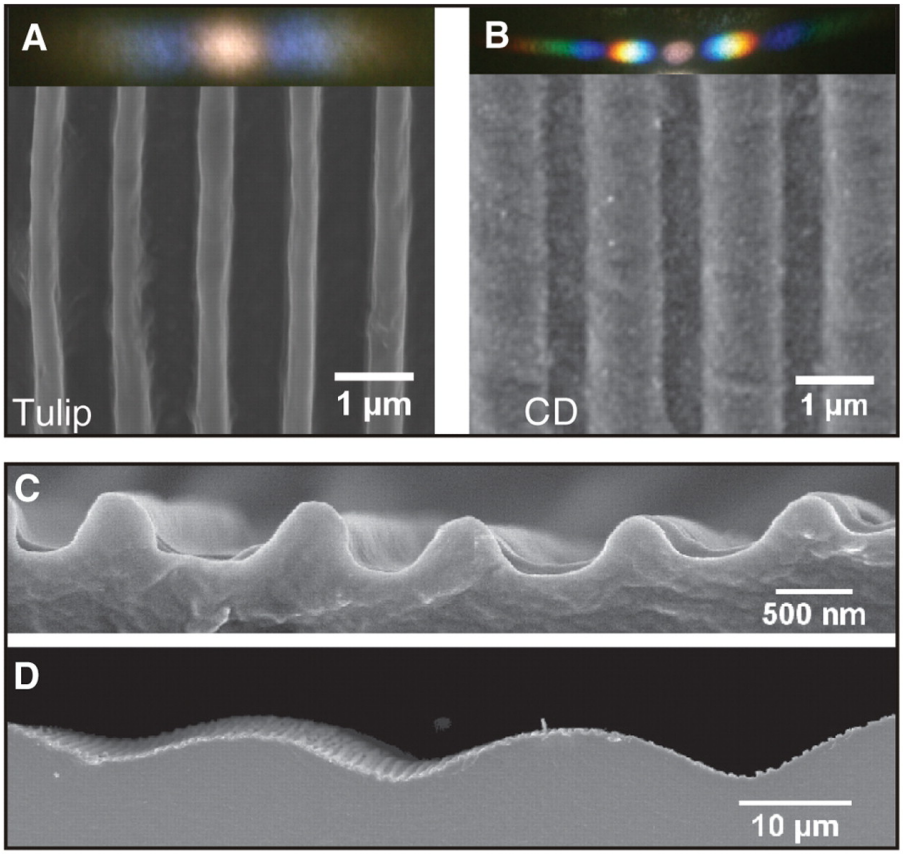

Figure 1–4: SEM images of tulip epoxy casts. (A) Top view of the petal surface, (B) Top view of an epoxy cast of a disassembled CD, (C) Side view of the structure from (A), (D) undulations of surface wrinkling. Adapted with permission from ref. [13].

1.5 Shape Equation

To describe surface geometry mathematically, a shape equation is necessary. Usually, the shape equation is the normal component of the force balance equation at the surface and depending on the nature of surface elasticity, such as bending and/or anchoring it can be algebraic or a partial differential equation for surface curvature. In this work, we neglect bending energy throughout and focus exclusively on anchoring. The shape equation that describes surface geometry in the cholesteric liquid crystal is based on the following assumptions:

- The CLC surface is an infinite 1-D manifold where the Gaussian curvature vanishes;
- The model is time-independent. We only focus on equilibrium patterns instead of transients that may include convective, Marangoni or backflows;
- The surface director field $\mathbf{n}(\mathbf{x})$ is known a priory and based on our previous work and experimental data [19, 20];
- Bulk elasticity arising from inhomogeneities in the interior of the liquid crystal is negligible;

The form of shape equation itself represents the mechanics of surface wrinkling in terms of capillary pressure, and its solutions give the possible patterns we can observe in nature.

1.6 Mechanics and Geometry

The mechanics of liquid crystal plays an important role in its applications. For example, in tissue engineering, surface tension promotes the growth of cell tissues, while bending stress changes the dynamic behaviour of cell tissues. The mechanics

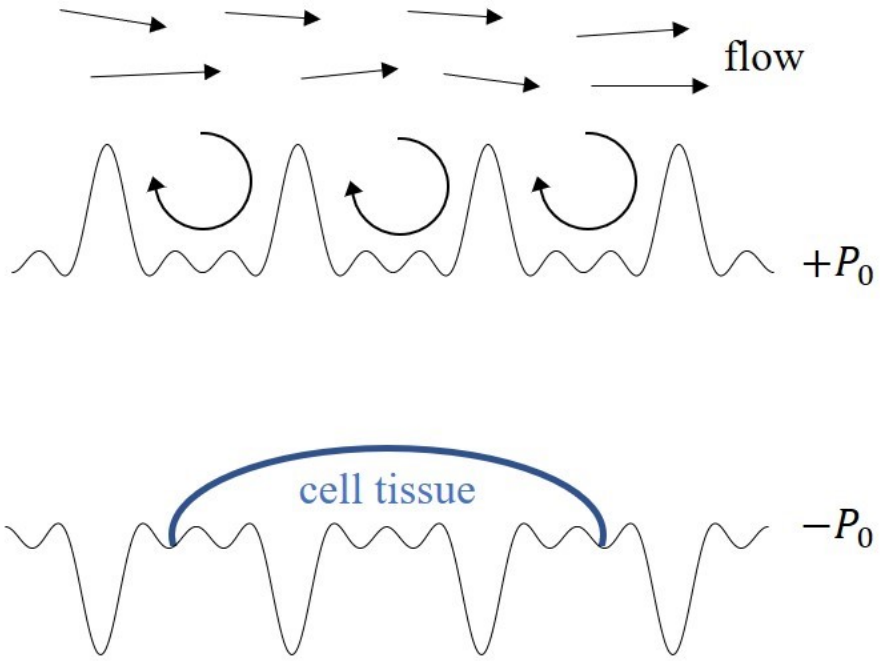

Figure 1–5: Reflection symmetry of the geometry affects the mechanical behavior, and can be used for different applications. The top diagram for a + pitch show a typical tribological application, where rugosity affects fluid flow patterns. The bottom diagram for a − pitch is a mirror symmetry of the top and has potential applications in tissue engineering. In principle an interchange from top to bottom or vice versa requires chirality reversal, as done by adding a chiral dopant.

of surface is highly dependent on the geometry. Anisotropic geometry allows stress concentration, which is the main consideration in fracture mechanics [21].

Fig. 1–5 shows two different surface patterns created by opposite sign chirality. The top surface profile (positive skewness with peaks pointing upwards) has sharp peaks, thus stress is easier to concentrate around those peaks. What is more, large valleys allow this surface to trap flows passing through. However, the bottom surface profile (negative skewness) does not show those properties. The figure reveals an

important fact in characterizing surface wrinkling: lower moments of the surface profile distribution do not capture the required information for real applications. Hence, information from the higher-order moment (skewness and kurtosis) of the surface profile is necessary, which will be discussed in Chapter 3 below.

The discovery of the relationship between mechanics and geometry is crucial in the target application of liquid crystals as sources of biomimetic inspiration. It also helps us to convert one problem into another, which sometimes simplifies analysis and provides an in-depth understanding of wrinkling phenomena, as shown in Chapter 2 and 3.

1.7 Objectives of the Thesis

The objectives of the thesis are:

- Derive the governing shape equation model for cholesteric liquid crystals such that we can analyze the geometry of the wrinkling surface; explain the crucial role that director field plays in the wrinkling behaviour through the pitch P_0;
- Use conservation methods (Lagrangian, least action) to develop equivalent shape equations emphasizing wrinkling driving forces and conserved quantities;
- Develop complementary models Maxwell-Lamé and least action method that lead to the shape equation shall be discussed, providing more physical insights;
- Use linearization and superposition to obtain linear shape equations that can be solved in closed form and that can yield accurate wrinkling scaling laws in terms of the critical material parameters;

- Characterize the geometry of wrinklings, such as the normal angle, surface profile, curvature distribution as well as a statistical result, including the second-order information (arithmetical mean value or standard deviation), the third-order moment (skewness) and the fourth-order moment (kurtosis) from the surface profile;
- Use capillary pressures and capillary vectors to explain the wrinkling mechanics;
- Elucidate the relationship between capillary pressures (mechanics) and curvature (geometry), to highlight the capillary forces behind wrinkling;
- Present an integrated geometro-mechanics characterization in terms of curvature and surface stress ratio, and the matrix representation;
- developed a comprehensive, integrated and quantitative model of surface wrinkling that can be used to design and control biomimetic surfaces.

In partial summary, the objective of this thesis is to provide a complete model to evaluate the surface wrinkling geometry as well as the coupled wrinkling mechanics. Then we quantify the relationship between geometry and mechanics, providing deeper physical insights and potential applications.

1.8 Thesis Organization

The detailed organization of the thesis and flow of information is shown in Fig. 1–6.

Fig. 1–6 shows the organization of this thesis. In Chapter 1 we discuss the basic background and objectives of this thesis. In Chapter 2, we evaluate the surface relief and its derivatives, then we use capillary pressures, which are defined by capillary

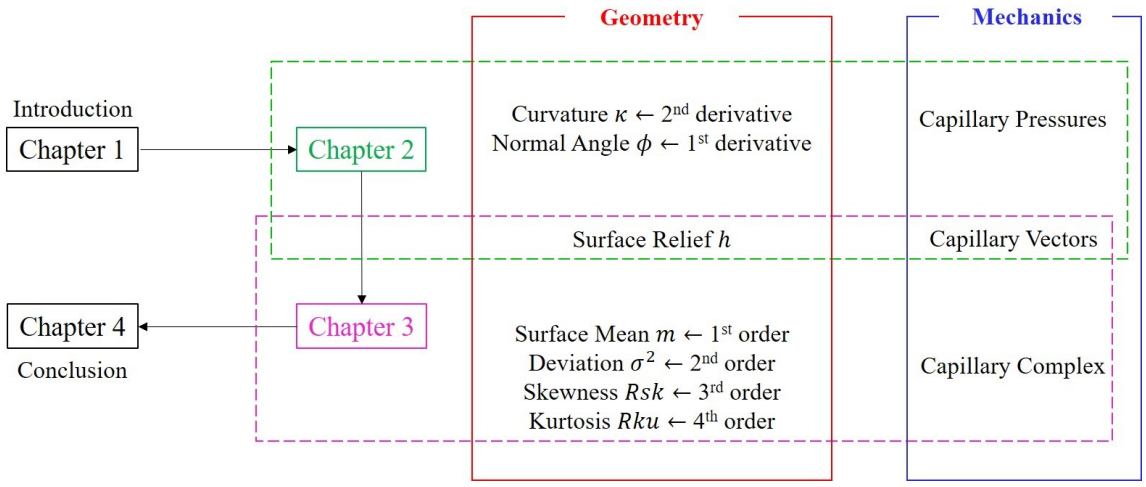

Figure 1–6: Flowchart of the organization of this thesis, where the content inside the green dash square represents parameters that will be discussed in Chapter 2, and that inside the magenta represents those of Chapter 3. Parameters inside the red square are the geometric parameters, and those inside the blue square are the mechanical parameters.

vectors, to elucidate the mechanics of surface wrinkling. In Chapter 3, we evaluate higher-order moment of the surface relief to obtain the statistical properties of surface wrinkling, whose magnitude are commonly used in the application in engineering such as manipulating skewness and kurtosis to change surface friction for tribological purpose. Then we illustrate how the capillary complex number, which is also defined by capillary vectors, impose effects on surface wrinkling geometry. Finally, we summarize our results in Chapter 4.

REFERENCES

[1] S. Mizuno J. Glowacki. Collagen scaffolds for tissue engineering, biopolymers. *Biopolymers*, 89:338–344, 2008.

[2] C. M. Bidan, K. P. Kommareddy, M. Rumpler, P. Kollmannsberger, P. Fratzl, and J. W. C. Dunlop. Geometry as a factor for tissue growth: Towards shape optimization of tissue engineering scaffolds. *Adv. Healthc. Mater.*, 2:186–194, 2013.

[3] M. Paris, A. Götz, I. Hettrich, C.M. Bidan, J. W. C. Dunlop, H. Razi, I. Zizak, D. W. Hutmacher, P. Fratzl, G. N. Duda, W. Wagermaier, and A. Cipitria. Scaffold curvature-mediated novel biomineralization process originates a continuous soft tissue-to-bone interface. *Acta Biomater.*, 60:64–80, 2017.

[4] P. Kollmannsberger, C. M. Bidan, J. W. C. Dunlop, P. Fratzl, and V. Vogel. Tensile forces drive a reversible fibroblast-tomyofibroblast transition during tissue growth in engineered clefts. *Sci. Adv.*, 4:eaao4881, 2018.

[5] A. Graziano, R. D′Aquino, M.G.C.-D. Angelis, F. De Francesco, A. Giordano, G. Laino, A. Piattelli, T. Traini, A. De Rosa, and G. Papaccio. Scaffolds surface geometrysignificantly affects human stem cell bone tissue engineering. *J. Cell. Physiol.*, 214:166–172, 2008.

[6] M. M. Giraud-Guille. Plywood structures in nature. *Curr. Opin. Solid. St. M.*, 3:221–227, 1998.

[7] T. Yamamoto, T. Hasegawa, M. Sasaki, H. Hongo, C. Tabata, Z. Liu, M. Li, and N. Amizuka. Structure and formation of the twisted plywood pattern of collagen fibrils in rat lamellar bone. *J. Electron. Microsc.*, 61:113–121, 2012.

[8] S. M. Chen, H. L. Gao, Y. B. Zhu, H. B. Yao, L. B. Mao, Q. Y. Song, J. Xia, Z. Pan, Z. He, H. A. Wu, and S. H. Yu. Biomimetic twisted plywood structural materials. *Natl. Sci. Rev.*, 5:703–714, 2018.

[9] V. Sharma, M. Crne, J. O. Park, and M. Srinivasarao. Bouligand structures underlie circularly polarized iridescence of scarab beetles: A closer view. *Mater. Today: Proc.*, 1:161–171, 2014.

[10] F. Carrión, G. Martínez-Nicolás, P. Iglesias, J. Sanes, and M. Bermúdez. Liquid crystals in tribology. *Int. J. Mol. Sci.*, 10:4102–4115, 2009.

[11] A. D. Rey. Liquid crystal models of biological materials and processes. *Soft Matter*, 6:3402–3429, 2010.

[12] A. D. Rey. Liquid crystal models of biological materials and processes. *Soft Matter*, 6:3402–3429, 2015.

[13] H. M. Whitney, M. Kolle, P. Andrew, L. Chittka, U. Steiner, and B. J. Glover. Floral iridescence, produced by diffractive optics, acts as a cue for animal pollinators. *Science*, 323:130–133, 2009.

[14] J. Yin, X. Han, Y. Cao, and C. Lu. Surface wrinkling on polydimethylsiloxane microspheres via wet surface chemical oxidation. *Sci. Rep.*, 4:5710, 2014.

[15] X. Feng, A. Mourran, M. Mller, and C. Bahr. Afm study of gibbs films of semifluorinated alkanes at liquid crystal/air interfaces. *Chemphyschem*, 14:1801–1805, 2013.

[16] N. Hano, M. Takafuji, and H. Ihara. One-pot preparation of polymer microspheres having wrinkled hard surfaces through self-assembly of silica nanoparticles. *Chem. Commun.*, 53:9147–9150, 2017.

[17] B. Jerome. Surface effects and anchoring in liquid crystals. *Rep. Prog. Phys.*, 54:391–451, 1991.

[18] J. Shan, W. Shi, L. Y. Liu, Y. R. Shen, and L. Xu. Optical control of surface anchoring and reorientation of liquid crystals via a plasmon-enhanced local field. *Phys. Rev. Lett.*, 109:147801, 2012.

[19] P. Rofouie, Z. Wang, and A. D. Rey. Two-wavelength wrinkling patterns in helicoidal plywood surfaces: imprinting energy landscapes onto geometric landscapes. *Soft Matter*, 14:5180–5185, 2018.

[20] Z. Wang, P. Rofouie, and A. D. Rey. Surface anchoring effects on the formation of two-wavelength surface patterns in chiral liquid crystals. *Crystals*, 9:190, 2019.

[21] M. D. Thouless and H. M. Jensen. Elastic fracture mechanics of the peel- test geometry. *J. Adhesion*, 38:185–197, 1992.

CHAPTER 2
Surface Anchoring Effects on the Formation of Two-Wavelength Surface Patterns in Chiral Liquid Crystals

Ziheng Wang, Pardis Rofouie and Alejandro D. Rey

Crystals (Open Access), 2019, **9**, 190 DOI Link

Preface: In Chapter 1, we introduced the background of cholesteric liquid crystals, the anchoring phenomenon and why they are important in nano-wrinkling applications. In Chapter 2, we will build a basic model using a continuum mechanics approach and then we will evaluate some important parameters describing surface wrinkling patterns such as normal angle, surface relief and curvature. We also use the concept of capillary pressure to understand the mechanics behind surface anchoring. Furthermore, we show novel mechano-geometry relations by linking capillary pressure (mechanics) and surface patterns (geometry).

Abstract: We present a theoretical analysis and linear scaling of two-wavelength surface nanostructures formed at the free surface of cholesteric liquid crystals (CLC). An anchoring model based on the capillary shape equation with the high order interaction of anisotropic interfacial tension is derived to elucidate the formation of the surface wrinkling. We showed that the main pattern-formation mechanism is originated due to the interaction between lower and higher order anchoring modes. A general phase diagram of the surface morphologies is presented in a parametric space of anchoring coefficients, and a set of anchoring modes and critical lines are

defined to categorize the different types of surface patterns. To analyze the origin of surface reliefs, the correlation between surface energy and surface nano-wrinkles is investigated, and the symmetry and similarity between the energy and surface profile are identified. It is found that the surface wrinkling is driven by the director pressure and is annihilated by two induced capillary pressures. Linear approximation for the cases with sufficient small values of anchoring coefficients is used to realize the intrinsic properties and relations between the surface curvature and the capillary pressures. The contributions of capillary pressures on surface nano-wrinkling and the relations between the capillary vectors are also systematically investigated. These new findings establish a new approach for characterizing two-length scale surface wrinkling in CLCs, and can inspire the design of novel functional surface structures with the potential optical, friction, and thermal applications.

Keywords: cholesteric liquid crystal; two-length scale surface wrinkling; capillary shape equation; anisotropic surface energy

2.1 Introduction

A variety of periodic surface structures and wrinkled textures are widely found in the plant and animal kingdoms [1, 2, 3, 4, 5, 6]. Since these surface ultrastructures with micro/nano scale features provide unique optical responses and iridescent colors [7, 8, 9, 10, 11], understanding their formation mechanism is crucial in realizing structural color in nature and in biomimetic design of novel photonic systems. As similar nano/micro scale periodic wrinkles are formed at the free surface of both synthetic and biological cholesteric liquid crystals (CLCs) [12, 13], and CLC phases are widely found in nature and living soft materials both in vivo and vitro [13, 14],

nematic liquid crystal self-assembly has been proposed as the formation mechanism of helicoidal plywoods and the surface ultrastructures in many fibrous composites ranging from plant cell walls to arthropod cuticles [15, 16, 17, 18, 19]. Moreover, it has been shown that the characteristics of chiral phases control the unique colors and optical properties exhibited in the films and fibers made by cellulose-based CLCs [20, 21].

Inspired by surface ultrastructure in nature, engineered surface structures incorporating chiral nematic structures can be fabricated to mimic the unique optical properties. If the formation of the surface patterns can be efficiently captured by a rigorous model based on a CLC mesophase, we can elucidate the pattern formation mechanisms for the construction of biomimetic proof-of-concept prototypes. In our previous work [22, 23, 24], significant efforts have been made in formulating and validating theoretical models to explain the formation of surface wrinkles in a plant-based CLC as a model material system. We identified the chiral capillary pressure, known as director pressure, that reflects the anisotropic nature of CLC through the orientation contribution to the surface energy as the fundamental driving force in generating single-wavelength wrinkling. However, surface wrinkling in nature can include more complex patterns such as multiple-length-scale undulations [11, 25, 26, 27]. To elucidate this feature, we previously proposed a physical model [28, 29] that combines membrane bending elasticity and liquid crystal anchoring. A rich variety of multi-scale complex patterns, such as spatial period-doubling and period-tripling are presented for the cases in which the anchoring and bending effects are comparable [28]. In a recent communication [30], we briefly presented

a pure higher order anchoring model in the absence of bending elasticity, surprisingly capturing multiple length-scale surface wrinkles. In this previous work, a novel mechanism for the formation of two-scale nano-wrinkling was proposed, which was exclusively based on anchoring energy including quartic harmonics. Here, we present a complete and rigorous new analysis of the multiple-length-scale surface wrinkles based on the pure higher order anchoring model in full detail and approximate the response of the surface structure to chirality and anchoring coefficients based on a linear model. In addition, a fundamental characterization of the capillary vector and capillary pressures required to connect surface geometry and mechanical forces is presented.

The objective of this paper is to identify the key mechanisms that induce and resist the multiple-length-scale surface wrinkling in CLCs based on a pure higher order anchoring model. To develop the anchoring model, we used the generalized shape equation for anisotropic interfaces using the Cahn-Hoffman capillarity [31] and the Rapini-Papoular quartic anchoring energy [32]. The presented model depicts the formation mechanism of two-length scale surface patterns based on the interaction between lower and higher order anchoring modes. The linear approximations of surface curvatures are derived to provide the explicit relations between the anchoring coefficients, helix pitch, and surface profile of the two-length scale wrinkles. These new findings can establish a new strategy for characterizing two-length scale surface wrinkling in biological CLCs, and inspire the design of novel functional surface structures with the potential optical, friction, and thermal applications.

The organization of this paper is as follows. Section 2.2 presents the geometry and structure of the CLC system. Section 2.3 presents the governing nemato-capillary shape equation expressing the coupling mechanism between the surface geometry and anisotropic ordering for a CLC free interfaces with a quartic anchoring energy and a pure surface splay-bend deformation. Appendix 2.A presents the details of the derivation of the Cahn-Hoffman capillary vector thermo-dynamics for CLC interfaces. Appendix 2.B describes the capillary shape equation in terms of three capillary pressures. Appendix 2.C represents the shape equation based on the driving and resisting terms. Section 2.4 analyzes the effect of anchoring coefficients and helix pitch on the surface normal angle and the resultant surface profile. In this section, a general phase diagram of surface profiles in the parametric of anchoring coefficients is presented and the origin of the two scales is revealed through the linear theory. Then, the linear approximations of surface curvatures, assuming small values of anchoring coefficients, are derived to identify the leading mechanism controlling the surface wrinkling. Appendix 2.D proposes the analytical expression for the linear approximation of the surface relief. The surface energy associated with the CLC interface is also analyzed to establish an energy transfer mechanism from anchoring energy of a flat surface into a wrinkled surface. Furthermore, the surface wrinkles are evaluated through analyzing the three capillary pressures, and the pressurecurvature relations are introduced to explore the variation of curvature profile with respect to the capillary pressures. Appendix 2.E represents the derivation of the pressurecurvature relations. Finally, the capillary vectors are formulated to provide

a clear physical explanation for the formation of the surface wrinkles. Appendix 2.F formulates the capillary vectors. Section 2.5 presents the conclusions.

2.2 Geometry and Structure

Figure 2–1 depicts the schematics of the CLC structure when ellipsoids indicate fiber orientation on each parallel layer. We assume that the helix axis, **H** is parallel to the surface; other complex structures occurring when the helix axis **H** is distorted are beyond the scope of this paper. The fiber orientation at the interface is defined by the director **n**. The pitch length P_0 is defined as the distance through which the fibers undergo a 2π rotation. For a rectangular (x, y, z) coordinate system, the surface relief that is directed along the x axis can be described by a $y(x, z)$ deviation from the xz plane. The amplitude of the vertical undulation is $h(x)$. As the surface relief is constant in the z direction for a linear texture, the curvature in the z-direction is zero. The unit tangent, **t**, and the unit normal, **k**, to the surface can be expressed with the normal angle, ϕ : $\mathbf{t} = (\sin\phi(x), -\cos\phi(x), 0)$, $\mathbf{k} = (\cos\phi(x), \sin\phi(x), 0)$. L is the given system length in the x direction. The arc-length measure of the undulating surface is "s".

2.3 Governing Equations

In this paper, we assume that the multi-length scale surface wrinkles are formed through modulation in surface energy at the anisotropic-air interface of CLCs. The typical capillary shape equations, which are generalized forms of a Laplace equation including the liquid crystal order and gradient density have been comprehensively formulated and previously presented for liquid crystal fibers, membranes, films, and drops [33]. Here, the coupling mechanism between the surface geometry and CLC

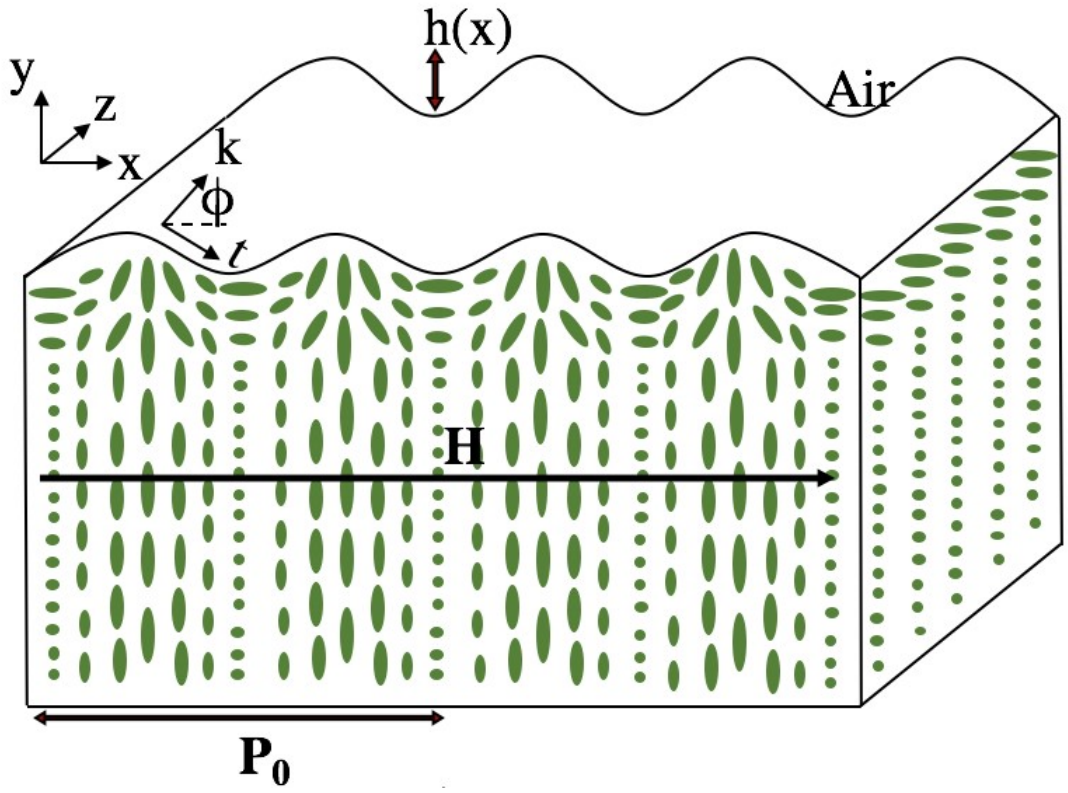

Figure 2–1: Schematic of a cholesteric liquid crystals (CLC) and surface structures. **H** is the helix unit vector, and P_0 is the pitch. The surface director has an ideal cholesteric twist in the bulk. The helix uncoiling near the surface creates a bend and splay planar (2D) orientation and surface undulations of nanoscale relief $h(x)$ with micron range wavelength $P_0/2$. Adapted from ref. [22].

order are demonstrated through the capillarity shape equation for CLC free interfaces with a pure surface splay-bend deformation.

The formation of surface nanostructures in CLC interfaces is a complex phenomenon involving interfacial tension, surface anchoring energy, and bulk Frank elasticity that requires integrated multi-scale modelling of bulk and surface. However, the analytic solution of the problem with the usual formalism is very complicated. Here, we assume a cholesteric director field in the bulk region, $\mathbf{n}_b(x) = (0, \cos\theta, \sin\theta)$, and a splay-bend director field at the interface $\mathbf{n}(x) = (\cos q, \sin q, 0)$ where $\theta = qx$, $q = 2\pi/P_0$, θ is the director angle, q is the wave vector, and P_0 is the helix pitch.

Based on the generalized Rapini-Papoular equation [24]. the interfacial surface energy, γ between a liquid crystal phase and another phase can be described by [32]

$$\gamma = \gamma_0 + \sum_{i=1}^{\infty} \mu_{2i} (\mathbf{n} \cdot \mathbf{k})^{2i} \tag{2.1}$$

where γ_0 is the isotropic contribution, $\mathbf{n}$ is the director field at the interface, $\mathbf{k}$ is the surface unit normal, and μ_{2i} are the temperature/concentration dependent anchoring coefficients. The preferred orientation that minimizes the anchoring energy (Equation (2.1)) is known as the easy axis. The actual stationary surface director orientation is the result of a balance between surface anchoring and bulk gradient Frank elasticity [34]. For the cases in which the gradient Frank elasticity is insignificant, the actual stationary and preferred director fields are identical. As shown in ref. [22], for the cholestericair interface with quite strong anchoring, the gradient Frank elasticity is negligible in comparison with anchoring in the formation of the surface undulations. It should be noted that here we neglect the Marangoni flow that is likely

to be formed due to the orientational-driven surface tension gradients [35, 36, 37]. Other effects and processes such as 3D orientation structures, strong nonlinearities, hydrodynamic [38, 39], and viscoelastic effects [40, 41, 42] discussed elsewhere are beyond the scope of this paper.

The generalized Cahn-Hoffman capillary vector $\boldsymbol{\Xi}$ [43, 44], is the fundamental quantity that reflects the anisotropic contribution of CLC in the capillary shape equation. It contains two orthogonal components: normal vector, $\boldsymbol{\Xi}_{\perp}$ representing the increase in surface energy through dilation (change in area) and tangent vector, $\boldsymbol{\Xi}_{\parallel}$ representing the change in surface energy through rotation of the unit normal. The derivation details of the Cahn-Hoffman capillary vector thermodynamics for anisotropic interfaces are given in Appendix 2.A [31].

$$\boldsymbol{\Xi} = \boldsymbol{\Xi}_{\perp}(\mathbf{n}, \mathbf{k}) + \boldsymbol{\Xi}_{\parallel}(\mathbf{n}, \mathbf{k}) \tag{2.2}$$

$$\boldsymbol{\Xi}_{\perp} = \gamma \mathbf{k}; \boldsymbol{\Xi}_{\parallel} = \mathbf{I}_s \cdot \frac{\partial \gamma}{\partial \mathbf{k}} \tag{2.3}$$

Here, $\mathbf{I}_s = \mathbf{I} - \mathbf{kk}$ is the 2×2 unit surface dyadic, and $\mathbf{I}$ is the identity tensor. The dyadic $(\mathbf{kk})^m$ is similar to $(\mathbf{tt})^m$ due to $(\mathbf{kk})^m = \mathbf{R} \cdot (\mathbf{tt})^m \cdot \mathbf{R}^{-1}$, where $\mathbf{t}$ is the unit tangent and $\mathbf{R}$ is the rotation matrix $\in$ SO(2) satisfying $\mathbf{k} = \mathbf{R} \cdot \mathbf{t}$ (see refs [45] and [46] for details):

$$\mathbf{R} = \begin{bmatrix} 0 & -1 \\ 1 & 0 \end{bmatrix} \tag{2.4}$$

The following identity holds:

$$\mathbf{nn} : \mathbf{kk} + \mathbf{nn} : \mathbf{tt} = 1 \tag{2.5}$$

The interfacial static force balance equation at the CLC/air interface is expressed by

$$-\mathbf{k}\cdot(\mathbf{T}^a-\mathbf{T}^b)=\nabla_s\cdot\mathbf{T}_s \tag{2.6}$$

where $\mathbf{T}^{a/b}$ represent the total stress tensor in the air and the bulk CLC phase, $\nabla_s=\mathbf{I}_s\cdot\nabla$ is the surface gradient operator, and $\mathbf{T}_s$ is the interface stress tensor. The air and the bulk CLC stress tensor, $\mathbf{T}^{a/b}$ are given by

$$\mathbf{T}^a=-p^a\mathbf{I}\text{ and }\mathbf{T}^b=-(p^b-f_g)\mathbf{I}+\mathbf{T}^E \tag{2.7}$$

where $p^{a/b}$ are the hydrostatic pressures, f_g is the bulk Frank energy density, and $\mathbf{T}^E$ is the Ericksen stress tensor. The bulk Frank energy density for a CLC reads

$$\begin{aligned}f_g=&\frac{K_1}{2}(\nabla\cdot\mathbf{n})^2+\frac{K_2}{2}(\mathbf{n}\cdot\nabla\times\mathbf{n}-q)^2+\frac{K_3}{2}(\mathbf{n}\times\nabla\times\mathbf{n})^2\\&+\frac{1}{2}(K_2+K_4)[\mathrm{tr}(\nabla\mathbf{n})^2-(\nabla\cdot\mathbf{n})^2]\end{aligned} \tag{2.8}$$

where $\{K_i\}(i=1,2,3)$ are splay, twist, and blend elastic constant, respectively. K_4 is saddle-splay elastic constant. The Ericksen stress tensor, $\mathbf{T}^E$ is given by

$$\mathbf{T}^E=-\frac{\partial f_g}{\partial\nabla\mathbf{n}}\cdot(\nabla\mathbf{n})^\intercal \tag{2.9}$$

The projection of Equation (2.6) along direction k yields the capillary shape equation:

$$\underbrace{(p^a-p^b)+f_g+\mathbf{kk}:\left[-\frac{\partial f_g}{\partial\nabla\mathbf{n}}\cdot(\nabla\mathbf{n})^\intercal\right]}_{\text{stress jump, SJ}}=\underbrace{(\nabla_s\cdot\mathbf{T}_s)\cdot\mathbf{k}}_{-p_c} \tag{2.10}$$

where stress jump, SJ, is the total normal stress jump, and p_c is the capillary pressure. Usually we take $p^a-p^b=0$, and consider te other terms as elastic correction. The

interfacial torque balance equation is given by

$$-\mathbf{h}+\mathbf{k}\cdot\frac{\partial f_g}{\partial\nabla\mathbf{n}}=\lambda^s\mathbf{n} \tag{2.11}$$

where λ^s is the Lagrange multiplier and h is the surface molecular field composed by two parts:

$$\mathbf{h}=-\underbrace{\frac{\partial\gamma_{an}}{\partial\mathbf{n}}}_{\mathbf{h}_{an}}\underbrace{-\frac{\partial\gamma_g}{\partial\mathbf{n}}+\nabla_s\cdot\left(\frac{\partial\gamma_g}{\partial\nabla_s\mathbf{n}}\right)}_{\mathbf{h}_g} \tag{2.12}$$

Here γ_g is the gradient interfacial free-energy density defined by introducing surface gradient energy density vector $\mathbf{g}$:

$$\mathbf{g}:=(\mathbf{n}\cdot\nabla)\mathbf{n}-\mathbf{n}(\nabla\cdot n)\text{ and }\gamma_g=\frac{1}{2}(K_2+K_4)\mathbf{k}\cdot\mathbf{g} \tag{2.13}$$

By multiplying $(\nabla\mathbf{n})^\intercal$ on both sides of Equation (2.11), the torque balance equation can be rewritten in a compact form:

$$-\mathbf{h}\cdot(\nabla\mathbf{n})^\intercal+\mathbf{k}\cdot\mathbf{T}^E=0 \tag{2.14}$$

Equation (2.14) gives an alternative path to compute $\mathbf{kk}:\mathbf{T}^E$. The expansion of the term $\mathbf{hk}:(\nabla\mathbf{n})^\intercal$ reads

$$\mathbf{hk}:(\nabla\mathbf{n})^\intercal=\left[-\frac{\partial\gamma_{an}}{\partial\mathbf{n}}-\frac{\partial\gamma_g}{\partial\mathbf{n}}+\nabla_s\cdot\left(\frac{\partial\gamma_g}{\partial\nabla_s\mathbf{n}}\right)\right]\cdot(\nabla\mathbf{n})^\intercal\cdot\mathbf{k} \tag{2.15}$$

which gives $\mathbf{hk}:(\nabla\mathbf{n})^\intercal$. Thus, only the bulk energy density, f_g, contributes to the elastic correction, which is negligible [22]. For typical cholesteric liquid crystals, the internal length K/γ_0 is in the range $1nm$ (an order of magnitude estimation of the elastic onstant K and the surface tension γ_0 gives $K\approx 10^{-11}\,\mathrm{J\,m^{-1}}$ and $\gamma_0\approx$

$10^{-2}\mathrm{J\,m^{-2}}$). As the ratio of W/γ_0 at the cholesteric-air interface with quite strong anchoring lies in the range ($B = W/\gamma_0 = 0.01$), the extrapolation length scale K/W is about $\frac{K}{W} = \frac{K/\gamma_0}{W/\gamma_0} \sim \frac{1[\mathrm{nm}]}{0.01} \sim 100[\mathrm{nm}]$. With these values, for a typical CLC with a pitch $P_0 \sim 1.2\,\mu\mathrm{m}$, the ration of extrapolation length scale to pitch is in the order of $\frac{K/W}{P_0} = \frac{100[\mathrm{nm}]}{1200[\mathrm{nm}]} = 0.08$. So, the elastic correction contributes 8% to the shape equation, and can be neglected to describe nano-scale surface undulations. As the result, the final shape equation becomes (see Appendix 2.B)

$$p_c = -(\nabla_s \cdot \mathbf{T}_s) \cdot \mathbf{k} = \nabla_s \cdot \boldsymbol{\Xi} = \underbrace{\frac{\partial \boldsymbol{\Xi}_\perp}{\partial \mathbf{k}} : (\nabla_s \mathbf{k})}_{\text{dilation pressure}} + \underbrace{\frac{\partial \boldsymbol{\Xi}_\parallel}{\partial \mathbf{k}} : (\nabla_s \mathbf{k})}_{\text{rotation pressure}} + \underbrace{\frac{\partial \boldsymbol{\Xi}_\parallel}{\partial \mathbf{n}} : (\nabla_s \mathbf{n})}_{\text{dilation pressure}} \quad (2.16)$$

The first two terms contain $\nabla_s \mathbf{k} = -\kappa \mathbf{t}\mathbf{t}$, providing information about the surface curvature $\kappa = \frac{d\phi}{ds}$, where ϕ is the normal angle and s is the arc-length. The first term on the right-hand side of Equation (2.16), which is the usual Laplace pressure, corresponds to the contribution from the normal component of the Cahn-Homman capillary vector. The second term which is the anisotropic pressure due to preferred orientation (known as Herring's pressure) corresponds to the contribution from the tangential component of the Cahn-Hoffman capillary vector $\boldsymbol{\Xi}_\parallel$. The last term in Equation (2.16) represents the additional contribution to the capillary pressure which corresponds to the director curvature due to orientation gradients (see Appendix 2.C). Considering a rectangular coordinate system (x, y, z), where x is the wrinkling direction, and y is the vertical axis, and considering the typical quartic anchoring model [24], $\gamma = \gamma_0 + \gamma_a$; $\gamma_a = \mu_2(\mathbf{n} \cdot \mathbf{k})^2 + \mu_4(\mathbf{n} \cdot \mathbf{k})^4$, yields the nonlinear

ordinary differential equation (ODE) in terms of normal angle, ϕ:

$$\frac{d\phi}{dx} = \frac{F_{\mathrm{Dr}}}{F_{\mathrm{Rs}}} = \frac{\partial_s \mathbf{n}}{\sin\phi} \cdot \frac{2[\mu_{2*} + 2\mu_{4*}(\mathbf{n}\cdot\mathbf{k})^2](\mathbf{n}\cdot\mathbf{k})\mathbf{t} + 2[\mu_{2*} + 6\mu_{4*}(\mathbf{n}\cdot\mathbf{k})^2](\mathbf{n}\cdot\mathbf{t})\mathbf{k}}{1 + \mu_{2*}[2(\mathbf{n}\cdot\mathbf{t})^2 - (\mathbf{n}\cdot\mathbf{k})^2] + 3\mu_{4*}(\mathbf{n}\cdot\mathbf{k})^2[4(\mathbf{n}\cdot\mathbf{t})^2 - (\mathbf{n}\cdot\mathbf{k})^2]} \tag{2.17}$$

Here F_{Dr} denotes as the driving force and F_{Rs} the resistant term. The boundary condition at $x = 0$, is $\phi|_{x=0} = \frac{\pi}{2}$. μ_{2*} and μ_{4*} are the scaled anchoring coefficients divided by isotropic surface tension γ_0, $\mu_{2*} = \mu_2/\gamma_0$ and $\mu_{4*} = \mu_4/\gamma_0$, and $\tilde{\phi}(x)$ is the approximation of $\phi(x)$. The generic features of the normal angle and its periodicity are the important outputs of the shape equation. There are three significant system parameters that have influence on the $\phi(x)$: the scaled anchoring coefficients (μ_{2*}, μ_{4*}), and the sign and magnitude of the helix pitch P_0. Thus, the surface profile $h(x)$ is a function of two material properties (μ_{2*}, μ_{4*}) and one structural order parameter (P_0). In the following context, we always assume that helix pitch is constant at $P_0 = 1.2\,\mu\mathrm{m}$. Figure 2–2a depicts the regions with different surface wrinkling in the parametric space of the scaled anchoring coefficients: O_4^+, O_4^-, H_2^+, H_2^-, P_2^+, H_4^+, H_4^-. Here O, H, and P refer to oblique, homeotropic, and planar director anchoring modes, respectively. The reader is directed to reference [30] for a full discussion of these fundamental states. The subscript numbers in O, H, and P indicate the wave number of morphologies in in one period, and the superscript sign differentiates the anchoring modes. The transition lines L_1 and L_2 are defined as $L_1 : \mu_{4*} = \mu_{2*}$ and $L_2 : \mu_{4*} = \mu_{2*}/2$, and the thermodynamic stability line ($\gamma = 0$) is $S : \mu_{4*} = -1 - \mu_{2*}$. Points A, B, C, and D are chosen as the representative points in P_2^+, O_4^+, H_2^+ and H_4^- regions with $\{\mu_{2*}, \mu_{4*}\}$: $A(0.002, 0.001)$, $B(-0.002, 0.0015)$, $C(-0.002, -0.001)$, and $D(0.002, -0.0015)$. Points A and C, and B and D are related by π rotation

symmetry. It should be noted that for the cases in which the quartic anchoring is zero, only single-wavelength sinusoidal profile can be obtained ($\mu_4 = 0$) in the linear regime ($|\mu_{2*}| << 1$).

2.4 Results and Discussion

2.4.1 Surface Profile

The surface normal angle, $\phi(x)$ can be directly obtained through solving the governing shape equation, Equation (2.17). The generic features of the normal angle $\phi(x)$, its magnitude, and its periodicity are the three key outputs of the model. The two significant parameters influencing $\phi(x)$ are the helix pitch P_0, and the scaled anchoring coefficients μ_{2*} and μ_{4*}, which affect the periodicity and the magnitude of $\phi(x)$, correspondingly. Theoretically, μ_{2*} and μ_{4*} give two degrees of freedom to the governing equation. But, for small anchoring coefficients and constant helix pitch, the shape of $\phi(x)$ is only a function of the anchoring ratio, $r = \mu_2/2\mu_4$. The plot of normal angle $\phi(x)$ as a function of the distance x, corresponding to the points A, B, C, and D, is shown in Figure 2–3a. As expected, the periodicity equals the half pitch, $P_0/2$, and the amplitude shows a slight deviation, $\phi(x) = \pi/2 + \epsilon(x)$. Figure 2–3b shows the effect of helix pitch on the normal angle $\phi(x)$ for the particular point B at three different values of helix pitch P_0, $P_0/2$, and $-P_0/2$. The helix pitch does not influence the amplitudes span of normal angle, but it changes the periodicity of the normal angle. By reducing the helix pitch to half, a more squeezed normal angle profile can be observed. The sign of P_0 reflects the normal angle profile with respect to $\pi/2$. It should be noted that we can estimate the behavior of curvature κ by checking the slope of $\phi(x)$ as $\kappa(x) = \partial_s[\phi(x)] = \phi'(x)sin\phi(x) \approx \phi'(x)$. The surface

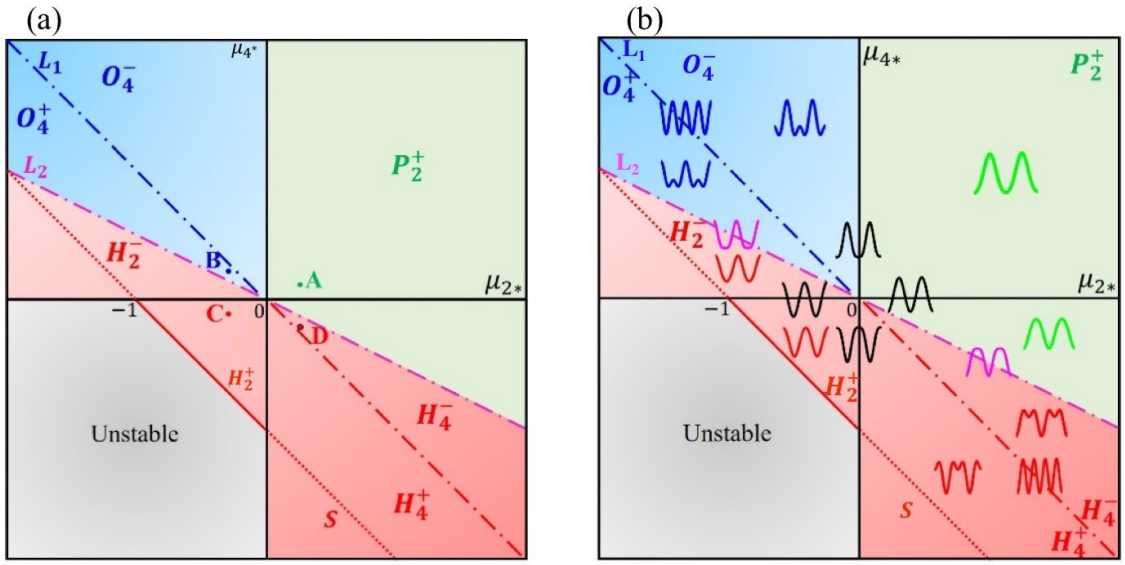

Figure 2–2: (a) Parametric space in terms of the anchoring coefficients obtained using Equation (2.17). Two characteristic lines $L_1 : \mu_{4*} = \mu_{2*}$ (blue dash-dot) and $L_2 : \mu_{4*} = \mu_{2*}/2$ (purple dash-dot) indicate wrinkling mode transitions, O_4^+, O_4^-, H_2^+, H_2^-, P_2^+, H_4^+, H_4^-. The subscript numbers indicate how many waves there are within one period. P, O, H represent planar, oblique, homeotropic anchoring, respectively. The thermodynamic line, S, passing point $\mu_{2*} = -1$ illustrates the points where it ends on μ_{2*} and μ_{4*} axes. A$(+0.002, +0.001)$, B$(0.002, +0.0015)$, C$(0.002, 0.001)$, and D$(+0.002, 0.0015)$ are four representative points in region P_2^+, O_4^+, H_2^+, and H_4^-, respectively. The region below the dotted S line implies an unstable state because the surface tension is negative. (b) Surface relief profile in the parametric (μ_{2*}, μ_{4*}) space obtained using Equation (2.17). The anchoring coefficients correspond to all computed curves are less than 0.01.

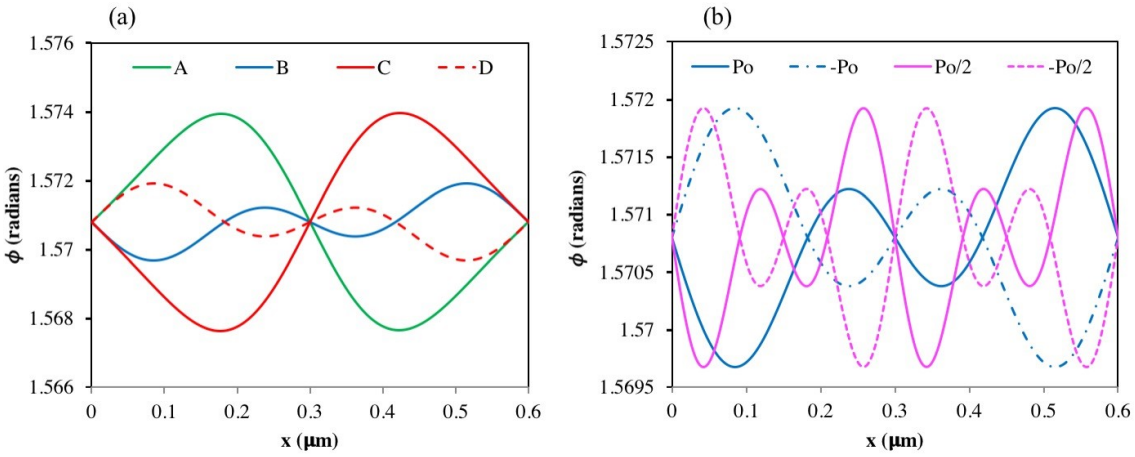

Figure 2–3: Normal angle profile. (a) The normal angle profiles corresponding to the points A, B, C, and D as illustrated in Figure 2–2a: A (green; mode P_2^+), B (blue, mode O_4^+), C (red, full line, mode H_2^+), and D (red, dash line, mode H_4^-). (b) The normal angle profile for the point B at different helix pitch values of P_0, $-P_0$, $P_0/2$, and $-P_0/2$, where $P_0 = 1.2\,\mu\text{m}$.

profile is then obtained from

$$h(s) = -\int_0^s \cot\phi(x)dx \tag{2.18}$$

Figure 2–4a shows typical surface profiles $h(x)$ and corresponding energy profile for the point B and point D. As shown in Figure 2–4a, increasing P_0 results in both higher periodicity and magnitude. We can clearly see that the surface relief profiles of points B and D exhibit the mirror symmetry, while changing the sign of P_0 result in the same mirror symmetry. These surface undulations can be validated with the two-length-scale surface modulations observed in a sheared CLC cellulosic films [25]. The two different scale periodical gratings include a primary set of bands perpendicular to the shear direction, and a smoother texture characterized by a secondary periodic structure containing small bands. It has been shown that the development and periodicities of the small bands are mainly ruled by the CLC characteristics. The chirality of CLC can therefore be mainly responsible for the formation of the secondary bands. The model can be also validated with the two-scale surface pattern of the Queen of the Night tulip [11], where fore this specimen the ratio of amplitudes are $h_2/h_0 = 0.01$, and corresponding wavelength is $\lambda = 1.2\,\mu\text{m}$.

Figure 2–4b shows the scaled energy profile, $\frac{(\gamma_*-1)}{q}$, in comparison with the surface profile for point B. The scaled energy profile gives the similar plot as the surface relief.

If we denote the parametric vector as $\boldsymbol{\mu}_* = (\mu_{2*}, \mu_{4*})$, then $h(x)$ becomes a function depending on two variables, the vector $\boldsymbol{\mu}_*$ and the helix pitch P_0. Within a

linear regime ($|\mu_{2*}| << 1, |\mu_{4*}| << 1$), the following identities holds true:

$$\text{Geometric Symmetries: } h(\boldsymbol{\mu}_*, P_0) = -h(-\boldsymbol{\mu}_*, P_0) = -h(\boldsymbol{\mu}_*, -P_0) = h(-\boldsymbol{\mu}_*, -P_0) \tag{2.19a}$$

$$\text{Surface Geometry-Energy Relation: } qh(\boldsymbol{\mu}_*, P_0) = \gamma_*(\boldsymbol{\mu}_*, P_0) - 1 \tag{2.19b}$$

This identity formulates the symmetric property of surface relief, and its relation to surface energy. Figure 2–4b is a clear demonstration of symmetry and scaling laws formulated in Equations (2.19a, 2.19b): if we compare B and D we have mirror symmetry and if we plot the anchoring energy of B we would see the same plot as the surface relief: $\underbrace{-h(D, P_0) = h(B, P_0)}_{\text{symmetry}}$, $\underbrace{h(B, P_0) = \dfrac{\gamma_*(B, P_0) - 1}{q}}_{\text{geometry-energy}}$.

Another important parameter that categorizes the shape of surface relief is the ratio between its two wavelengths. The origin of the two scales can be revealed through the linear theory, which gives the signed amplitudes of h_0 and h_2 (the nomenclature is defined in Figure 2–4b) as a function of anchoring ratio, $r = \mu_2/2\mu_4$:

$$\frac{\tilde{h}_0}{\tilde{h}_2} = \frac{r^2}{(1+r)^2} \tag{2.20}$$

L_1 and L_2 are defined as the two mode transition lines. Line L_1, which gives a four-wave profile within one period corresponds to the condition $\mu_{4*} = -\mu_{2*}(r = -1/2, \tilde{h}_0 = \tilde{h}_2)$. Line L_2, which gives a two-wave profile within one period corresponds to the condition $\mu_{4*} = \mu_{2*}/2(r = -1, \tilde{h}_2 \to 0)$. In addition, if $\mu_{4*} \to 0$, then $r \to \infty$ such that $\tilde{h}_0 \to \tilde{h}_2$, also gives a two-wave profile.

Figure 2–2b shows the general phase diagram of $h-$profiles in the parametric (μ_{2*}, μ_{4*}) plane. As shown in the figure, the transition lines L_1 and L_2 are the critical

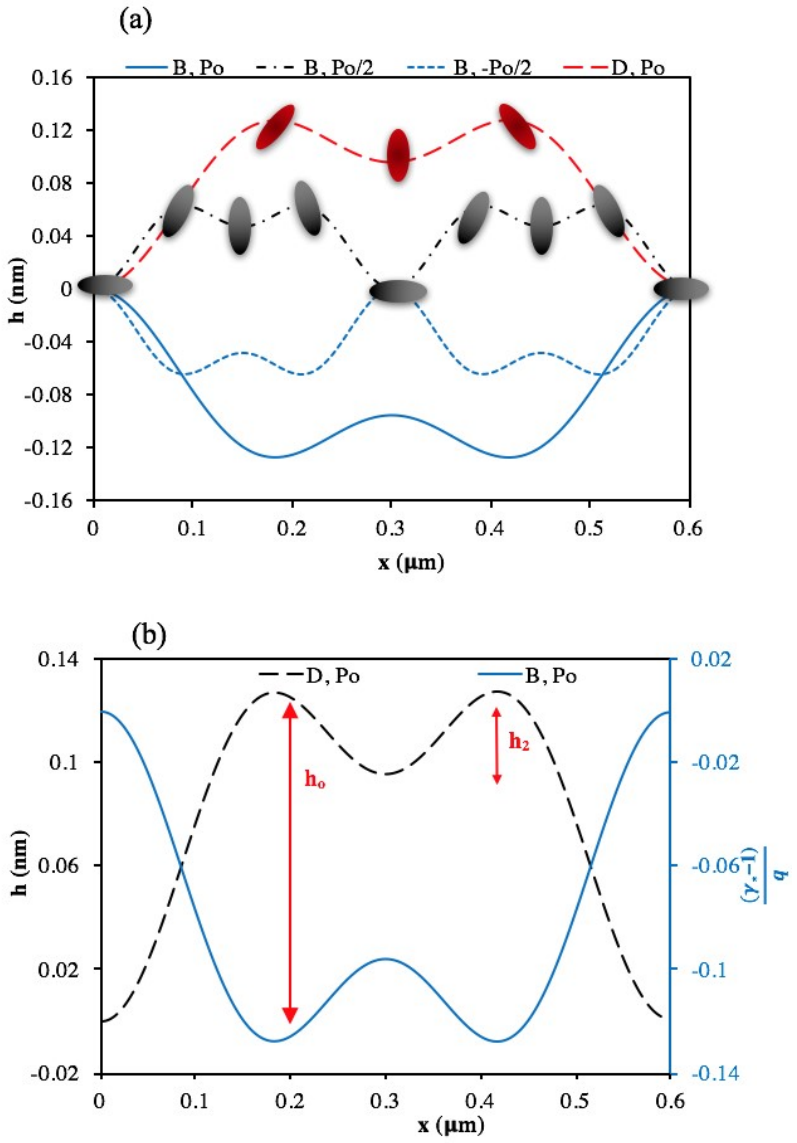

Figure 2–4: Mirror symmetries observed in surface relief profiles. (a) The surface relief profiles at point B with different helix pitches are given by the two blue curves and the black curve. The red curve gives the surface relief profile at point D. The red and black ellipsoids depict the director orientation for point B with $P_0/2$ and point D with P_0, respectively. These ellipsoids show where the surface extrema occur for planar, homeotropic, and oblique anchoring. (b) The surface profile at point D and scaled energy profile at point B. This figure indicates that there is similarity between surface relief profile and energy profile. The helix pitch is $P_0 = 1.2\,\mu\text{m}$.

lines across which surface relief changes its shape. We identify line L_1 as a resonant line with the maximum interaction between quadratic and quartic anchoring effects.

The computations show that h-profile is centrally symmetrical with respect to original point, which can be observed in Figure 2–2b. As summarized as in Table 2–1, there are mainly three types of surface wrinkling patterns. It should be noted that there is no difference between O_4^+ and O_4^- as the patterns shown in one region are just a phase shift of the other; the same applies to H_4^+ and H_4^-. However, there is a difference between regions L_2, $\mu_{2*} = 0$ and H_2^+, H_2^-, P_2^+, $\mu_{4*} = 0$ due to the existence of a small plateau shown in the pattern computed along the two lines: L_2 and $\mu_{2*} = 0$. This small plateau corresponds to the discontinuity of two capillary vectors diagram which will be discussed later.

Table 2–1: Surface wrinkling patterns in different regions of the parametric space $\boldsymbol{\mu}_* = (\mu_{2*}, \mu_{4*})$

Region	Total Wave Number	h_2/h_0
$O_4^+, O_4^-, H_4^+, H_4^-$	4	$\neq 1$
L_1	4	$= 1$
$H_2^+, H_2^-, P_2^+, \mu_{4*} = 0$	2	0
$L_2, \mu_{2*} = 0$	2	0

Results above are considered within one period. Nomenclature: O(oblique), P(planar), and H(homeotropic) refer to the type of anchoring. The L_i's refer to transition lines; see text.

Table 2–1 summarizes the main four types of surface relief profiles. Region O_4^+, O_4^-, H_4^+, H_4^- and L_1 both give four waves within one period. The difference is that four waves are identical on line L_1. Region H_2^+, H_2^-, P_2^+, $\mu_{4*} = 0$ and L_2, $\mu_{2*} = 0$ both give two waves within one period, so h_2/h_0 is equal to 0. The difference

between these two modes is that region H_2^+, H_2^-, P_2^+, $\mu_{4*} = 0$ gives very smooth surface geometry while region L_2, $\mu_{2*} = 0$ gives sharp peaks on the surface profile.

2.4.2 Surface Curvature

In this subsection we present, discuss, and characterize the surface curvature obtained from direct numerical simulations of the governing equations, and from a new and highly accurate linear model.

The surface behavior is not only affected by the magnitude of the surface relief, but also by the surface curvature. The curvature can be computed directly by two equivalent forms:

$$\kappa = \frac{d\phi}{ds} \text{ or } \kappa = \left[1 + \left(\frac{dh}{dx}\right)^2\right]^{-\frac{3}{2}} \frac{d^2h}{dx^2} \tag{2.21}$$

The first computing method in Equation (2.21) is exactly based on the governing Equation (2.17). Considering that for small values of anchoring coefficients, the resistant term is mainly controlled by isotropic energy γ_0, we obtain the resistant term denoted in Equation (2.17), $F_{\text{Rs}} = 1$. So, the linear approximation of curvature reads

$$\tilde{\kappa}_{\tilde{\phi}} = 2q[\mu_{2*} \cos 2qx + 2\mu_{4*}(3 \sin^2 qx \cos^2 qx - \sin^4 qx)] \tag{2.22}$$

where $\tilde{\kappa}_{\tilde{\phi}}$ denotes the linear approximation of curvature assuming that $\phi = \pi/2$. The analytical expression for the linear approximation of the surface relief is proposed in Appendix 2.D. By assuming $\tilde{\kappa}_{\tilde{h}} = h_{xx}$, we can also obtain another approximation for the surface curvature. It can be easily found that $\tilde{\kappa}_{\tilde{h}} = \tilde{\kappa}_{\tilde{\phi}}$ as we made similar assumptions to approximate the surface curvature based on Equation (2.21).

A more sophisticated approximation of curvature $\tilde{\kappa}_G$ can be derived without linearing the governing equation:

$$\tilde{\kappa}_G = q \cdot \frac{2(\mu_{2*} + 6\mu_{4*}\sin^2 qx)\cos^2 qx - 2(\mu_{2*} + 2\mu_{4*}\sin^2 qx)\sin^2 qx}{1 + \mu_{2*}(2\cos^2 qx - \sin^2 qx) + 3\mu_{4*}\sin^2 qx(4\cos^2 qx - \sin^2 qx)} \tag{2.23}$$

As illustrated in Figure 2–5, the linear approximation of curvature $\tilde{\kappa}_{\tilde{\phi}}$ obtained by Equation (2.22) and $\tilde{\kappa}_G$ from Equation (2.23) provides a very good approximation of curvature. As the curvature $\tilde{\kappa}_{\tilde{\phi}}$ includes the explicit and simple expression, it allows us to mathematically derive more feasible relations to characterize the formation of the surface relief.

2.4.3 Surface Energy

Understanding surface energy behavior is another perspective in realizing the surface profile which helps us to establish an energy transfer mechanism from the anchoring energy of a flat surface into a wrinkled surface. For sufficient small values of the anchoring coefficients, as the normal angle profile $\phi(x)$ is fluctuating around $\pi/2$ with a very small amplitude, an explicit relation between the linearized surface profile and the total surface energy can be estimated based on the linear approximation:

$$\tilde{\gamma}_* - 1 = q\tilde{h} \tag{2.24}$$

where $(\tilde{\gamma}_* - 1)$ is the scaled anisotropic anchoring energy, and $q\tilde{h}$ is the scaled surface relief. This correlation is detected in Figure 2–4b where h and $\frac{(\gamma_* - 1)}{q}$ are essentially identical for the small anchoring coefficients. This simple expression implies an essential physical phenomenon. The expression, Equation (2.24) verifies that zero anisotropic surface energy results in a flat surface ($h = 0$). As the result, based on

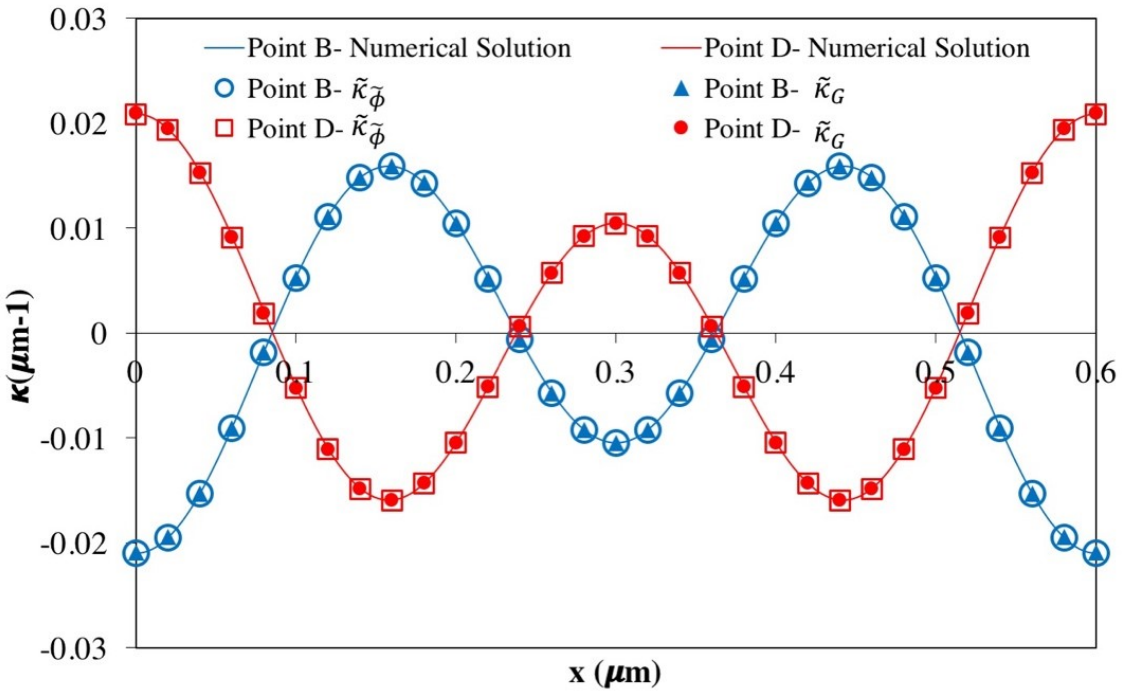

Figure 2–5: Surface curvature profiles computed numerically and with the two approximation methods: $\tilde{\kappa}_{\tilde{\phi}}$ and $\tilde{\kappa}_G$. Blue and red solid lines are the numerical solutions solved from governing equation for point B and D, respectively. Blue hollow circles and blue filled triangles represent the data points of computed $\tilde{\kappa}_{\tilde{\phi}}$ and $\tilde{\kappa}_G$ at point B, respectively. Red hollow squares and red filled circles represent the data points of computed $\tilde{\kappa}_{\tilde{\phi}}$ and $\tilde{\kappa}_G$ at point D, respectively. As the both approximations $\tilde{\kappa}_{\tilde{\phi}}$ and $\tilde{\kappa}_G$ are identical, the filled circles and triangles are superimposed on hollow squares and circles. The helix pitch is $P_0 = 1.2\,\mu\text{m}$.

the expression, the anchoring energy is the driving force contributing to the surface relief, which is in accordance with the previous findings [22]. Moreover, the expression confirms the expected insight that the uppermost surface area contain the highest surface energy.

2.4.4 Capillary Pressures

As mentioned above, the three main contributions in the capillary pressure are (1) P_{dil}: dilation pressure (Laplace pressure), P_{rot}: rotation pressure (Herrings pressure), P_{dir}: director curvature which is the anisotropic pressure due to the preferred orientation (see Equation (2.16)). P_{dir} is the driving forces to wrinkle the interface. The explicit expansion of Equation (2.16) in terms of $(\mathbf{n}\cdot\mathbf{k})$ yields:

$$
\begin{aligned}
p_c &= P_{\text{dil}} + P_{\text{rot}} + P_{\text{dir}} \\
P_{\text{dil}} &= -\kappa[1 + \mu_{2*}(\mathbf{nn}:\mathbf{kk}) + \mu_{4*}(\mathbf{nn}:\mathbf{kk})^2] \\
P_{\text{rot}} &= -\kappa[2\mu_{2*}(\mathbf{nn}:\mathbf{tt} - \mathbf{nn}:\mathbf{kk}) + 4\mu_{4*}(\mathbf{nn}:\mathbf{kk})(3\mathbf{nn}:\mathbf{tt} - \mathbf{nn}:\mathbf{kk})] \\
P_{\text{dir}} &= 2[\mu_{2*} + 2\mu_{4*}(\mathbf{nn}:\mathbf{kk})](\mathbf{n}\cdot\mathbf{k})\mathbf{t}\cdot\partial_s\mathbf{n} + 2[\mu_{2*} + 6\mu_{4*}(\mathbf{nn}:\mathbf{kk})](\mathbf{n}\cdot\mathbf{t})\mathbf{k}\cdot\partial_s\mathbf{n}
\end{aligned}
\tag{2.25}
$$

As all the pressures are scaled by isotropic tension γ_0, they have the same unit as curvature. It should be noted that based on theory $\dim[P] = \dim[\gamma]\cdot\dim[\partial_s]$. Figure 2–6a shows the wrinkling mechanism through the capillary pressures changes along x. The three scaled pressure contributions are plotted as function of x for the particular point B. As shown in the figure, the capillary pressures cancel each other out maintaining the summation at zero. The important observation from these pressure profiles is that P_{dil} and P_{dir} are always out-of-phase, while P_{rot} is

always negative. These outcomes, $P_{\text{dir}} \cdot P_{\text{dil}} \leq 0$ and $\text{sgn}(P_{\text{rot}}) = -\text{sgn}(P_0)$ can be also interpreted from the linear model. Figure 2–6a also denotes that P_{rot} is two orders of magnitude smaller than P_{dil} and P_{dir}. This phenomenon confirms that P_{dir} is the formation source of wrinkling, annihilated by inducing area change and area rotation. Another observation from the linear model is that P_{rot} has the similar expression of curvature, $\tilde{\kappa}$. This similarity encourages us that capillary pressures can be also analyzed in the $\kappa - P$ frame. Figure 2–6b shows the variation of curvature profile with respect to the capillary pressures. We can realize from the figure that in the linear region and for the constant P_0, each capillary pressure only lay on intrinsic curves independent of the anchoring coefficients. The linear approximation gives the intrinsic curves (see Appendix 2.E for the details):

$$\tilde{P}_{\text{dil}} = -\tilde{\kappa}, \tilde{P}_{\text{rot}} = -\frac{\tilde{\kappa}^2}{q} \text{ and } \tilde{P}_{\text{dir}} = \tilde{\kappa} + \frac{\tilde{\kappa}^2}{q} \tag{2.26}$$

The $\kappa - P$ relations approve that helix pitch P_0 is the only parameter affecting the intrinsic curves. Equation (2.26) implies that the intrinsic curves obtained for $-P_0$ show the central symmetry. Variations in anchoring coefficients do not impose any influence on the intrinsic curves, they only change the arc-length of the intrinsic curves (denoted by $\tilde{l}$). The analytical expression of the arc-length for the intrinsic

curves can be obtained by

$$\tilde{l}_{\text{dil}} = \sqrt{2}(\tilde{\kappa}_{\max} - \tilde{\kappa}_{\min}) \tag{2.27}$$

$$\tilde{l}_{\text{rot}} = \left[\kappa\sqrt{\left(\frac{1}{2}\right)^2 + \left(\frac{\kappa}{q}\right)^2} + \frac{q}{4}\ln\left|\frac{\kappa}{q} + \sqrt{\left(\frac{1}{2}\right)^2 + \left(\frac{\kappa}{q}\right)^2}\right|\right]\Bigg|_{\tilde{\kappa}_{\max}-\tilde{\kappa}_{\min}} \tag{2.28}$$

$$\tilde{l}_{\text{dir}} = \frac{q}{4}\left[\left(1+\frac{2\kappa}{q}\right)\sqrt{1+\left(1+\frac{2\kappa}{q}\right)^2} + \ln\left|\left(1+\frac{2\kappa}{q}\right) + \sqrt{1+\left(1+\frac{2\kappa}{q}\right)^2}\right|\right]\Bigg|_{\tilde{\kappa}_{\max}-\tilde{\kappa}_{\min}} \tag{2.29}$$

where $\tilde{\kappa} \in [\tilde{\kappa}_{\min}, \tilde{\kappa}_{\max}]$. If we denote $\min_a = -\mu_{4*} - |\mu_{2*} + \mu_{4*}|$, $\max_a = -\mu_{4*} + |\mu_{2*} + \mu_{4*}|$, and $\text{local} = -(\mu_{2*} + 2\mu_{4*}) + (\mu_{2*} + 5\mu_{4*})^2/8\mu_{4*}$, then we denote $\min_b = \min\{\min_a, \max_a, \text{local}\}$ and $\max_b = \max\{\min_a, \max_a, \text{local}\}$, considering the approximation curvature, $\tilde{\kappa}_{\tilde{\phi}}$ (Equation (2.22)), the interval of $\tilde{\kappa}$ can be found by

$$\tilde{\kappa} \in [2q \cdot \min_a, 2q \cdot \max_a] \text{ if } r \notin [-5/3, 3/2] \tag{2.30}$$

$$\tilde{\kappa} \in [2q \cdot \min_b, 2q \cdot \max_b] \text{ if } r \in [-5/3, 3/2] \tag{2.31}$$

These findings denote that the span of curvature is associated with the anchoring coefficients, and ideally exhibits a linear correlation with $1/P_0$. So, we expect that if the helix pitch is increased to $2P_0$ under the same anchoring condition, the span of curvature would reduce to half. Figure 2–6b illustrates the numerical solutions for director, dilation, and rotation pressures obtained by Equation (2.25) in comparison with the intrinsic lines defined by Equation (2.26). We can observe that there are no considerable deviations between the director pressures and the intrinsic lines approximated by the linear model. As shown in Figure 2–6b, the span of actual

curvature is in accordance with the minimum and maximum values of curvature computed by Equations (2.30) and (2.31), which confirms that the linear approximation is validated within the linear region (small anchoring coefficients).

In partial summary, in this subsection we have shown (i) the key balancing pressures are the Laplace and director pressures (Figure 2–6); (ii) quadratic curvature contributions are proportional to the pitch, the curvature-pressure relations follow intrinsic curves (Equation (2.26)) whose lengths are affected by anchoring, such that lower anchoring (higher anchoring) decreases (increases) their lengths (Equation (2.27)-(2.31)).

2.4.5 Capillary Vectors

The behavior of the capillary vectors can give another perspective to analyze the surface wrinkling. If we assume that $\mu_{4*} = 0$, then the magnitude of two capillary vectors $\xi_\perp$ and $\xi_\parallel$ naturally satisfy

$$\frac{[\xi_\perp - (\gamma_0 + \frac{1}{2}\mu_2)]^2}{(\frac{1}{2}\mu_2)^2} + \frac{\xi_\parallel^2}{\mu_2^2} = 1 \tag{2.32}$$

ξ denotes the magnitude of the capillary vector, $\boldsymbol{\Xi}$. From this equation, we can read an ellipse with eccentricity $\mathrm{e_{cc}} = \sqrt{3}/2$ which is independent of anchoring coefficient μ_2. The two capillary vectors change proportionally; $\xi_\perp$ oscillates around $\gamma_0 + \frac{1}{2}\mu_2$ with an amplitude of $\frac{1}{2}|\mu_2|$, while $\xi_\parallel$ oscillates around zero with amplitude of $|\mu_2|$. This ellipse with invariant shape can provide a clear physical explanation to understand how capillary vectors are formed. Figure 2–7a illustrates the plots of the ellipse equation for the anchoring coefficient $|\mu_{2*}| = 0.002$. Considering that the CLC surface is differentiable, we can introduce two foci (F_1 and F_2, defined

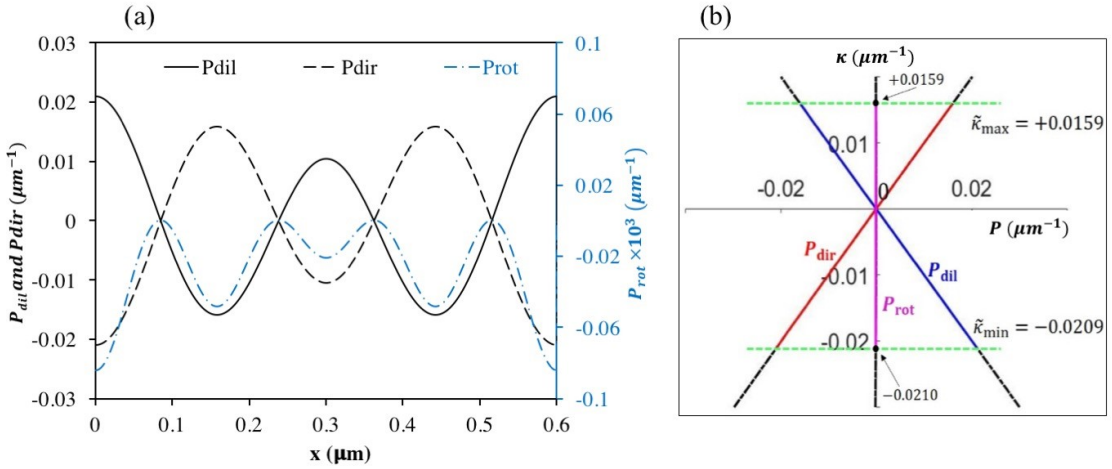

Figure 2–6: Capillary pressure profile. (a) Three components of capillary pressures with respect to x axis for the point B. Black real line, black dash line, and blue dot line represent dilation pressure, director pressure, and rotation pressure, respectively. (b) Curvature-Pressure plot at point B. Red, blue, and purple lines represent the numerical solutions to director pressure, dilation pressure, and rotation pressure, respectively. Black dash lines are the intrinsic lines defined by Equation (2.26). Green dash lines are the span of curvature computed by Equations (2.30) and (2.31). Two black points are where the span of numerical solution for curvature ends. The helix pitch is $P_0 = 1.2\,\mu\text{m}$.

by μ_{2*} in Figure 2–7b) such that every point P in the vector diagram is restrained by $|PF_1| + |PF_2| = 2|\mu_{2*}|$. When $\mu_2 \to 0$, two foci are very close to each other, giving that $|PF_1| \approx |PF_2| = |\mu_{2*}|$. Ellipse becomes a circle with a radius of $|\mu_{2*}|$, which can be considered as a point. From Figure 2–7a we can also observe that $\xi_\perp$ only reaches its extrema when $\xi_\parallel$ vanishes. This phenomenon corresponds to $\xi_\parallel = \|\mathbf{I}_s \cdot \partial_{\mathbf{k}}\gamma\| = \mathbf{t} \cdot \partial_{\mathbf{k}}\xi_\perp$. However, when $\xi_\parallel$ reaches its extrema, $\xi_\perp$ does not vanish as isotropic surface tension prevents $\xi_\perp$ to be reduced to zero.

The solution to ellipse equation yields

$$\xi_\parallel = \pm\sqrt{\mu_2^2 - 4[\xi_\perp - (\gamma_0 + \frac{1}{2}\mu_2)]^2} \text{ and } \xi_\perp = \left(\gamma_0 + \frac{1}{2}\mu_2\right) \pm \frac{1}{2}\sqrt{\mu_2^2 - \xi_\parallel^2} \tag{2.33}$$

These are explicit algebraic relations between $\xi_\perp$ and $\xi_\parallel$. Recall that the capillary vectors and the normal angle are related by

$$\phi(x) = \frac{\pi}{2} + \int_0^x \frac{1}{\xi_\perp}\partial_x\xi_\parallel dx \tag{2.34}$$

Replacing $\xi_\perp$ with $\xi_\parallel$ from Equation (2.33), the normal angle can be expressed only in term of $\xi_\parallel$ (see Appendix 2.F):

$$\begin{gathered}
\phi = \frac{\pi}{2} + \phi_\parallel(\xi_\parallel) \text{ where} \\
\phi(\xi_\parallel) = 2\arcsin\frac{\xi_\parallel}{\mu_2} - \frac{2(2+\mu_{2*})}{\sqrt{1+\mu_{2*}}}\arctan\left[\sqrt{\frac{1}{1+\mu_{2*}}}\tan\left(\frac{1}{2}\arcsin\frac{\xi_\parallel}{\mu_2}\right)\right] \text{ or} \\
\phi(\xi_\parallel) = -2\arcsin\frac{\xi_\parallel}{\mu_2} - \frac{2(2+\mu_{2*})}{\sqrt{1+\mu_{2*}}}\arctan\left[\sqrt{\frac{1}{1+\mu_{2*}}}\cot\left(\frac{1}{2}\arcsin\frac{\xi_\parallel}{\mu_2}\right)\right]
\end{gathered} \tag{2.35}$$

Equation (2.35) clarifies the source of fluctuation; the perturbation $\phi_{\|}(\xi_{\|})$, is imposed onto the normal angle profile due to the presence of $\xi_{\|}$, which is fixed by the ellipse equation.

If we assume that $\mu_{2*} = 0$, the magnitude of two capillary vectors $\xi_{\perp}$ and $\xi_{\|}$ satisfy

$$\frac{\xi_{\|}^2}{\mu_4^2} - 2\left[\frac{4(\xi_{\perp} - \gamma_0)}{\mu_4}\right]^{\frac{3}{2}} + \frac{16(\xi_{\perp} - \gamma_0)^2}{\mu_4^2} = 0 \tag{2.36}$$

This equation reads a teardrop curve. Figure 2–7b illustrates the plots of the teardrop equation for the anchoring coefficient $|\mu_{4*}| = 0.002$. The main parameters defining this teardrop curve are given in Figure 2–7b. Similar to the ellipse curves shown in Figure 2–7a, the magnitude of μ_{4*} does not change the shape of teardrops, while it controls the size of the teardrop curves. It should be noted that the teardrop curves are not continuous at the original point (Point O shown in Figure 2–7b). Both the ellipse and teardrop curves show a symmetry by changing the sign of the anchoring coefficients, and shrink to zero as the anchoring coefficients go to zero.

2.5 Conclusions

This paper presents a rigorous model based on nonlinear nemato-capillarity shape equation and its linear approximation to describe the main formation mechanism of two-length scale surface wrinkling formed at the CLC/air interface. The role of three capillary pressure contributions (dilation, rotation, and director curvature) on the formation of surface curvature have been elucidated and the effect of the helix pitch and the anchoring coefficients has been characterized. The linear approximation provides a simple model to describe wrinkling behavior with high accuracy and

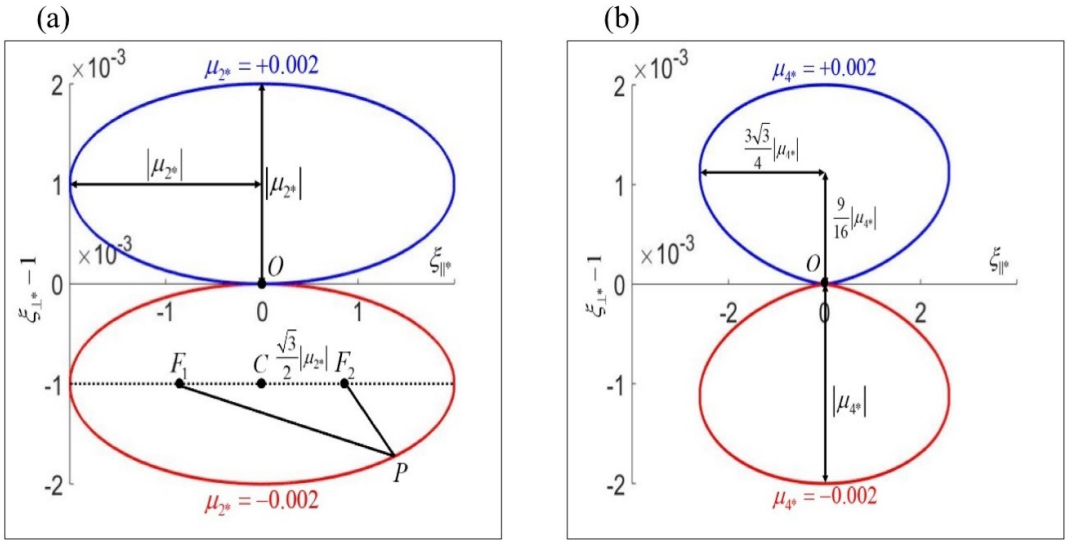

Figure 2–7: Plots of capillary vector components under two limiting anchoring coefficient values. (a) $\mu_{4*} = 0$ results in an ellipse. (b) $\mu_{2*} = 0$. This results in a teardrop curve. The sign of anchoring coefficient imposes a mirror symmetry. The axes of the loops are determined by the anchoring coefficients.

less computation when the two anchoring coefficients are very small. The linear approximation can also serve as the main criteria to classify the type of surface relief. The key mechanism driving surface wrinkling is identified and discussed through the two perspectives: capillary pressures and capillary vectors. Moreover, the surface normal is expressed by the capillary pressures, whose summation must maintain at zero, serving as the constraint to the system. The proposed new model and its linear approximation augment previous models dedicated to understand and mimic complex surface patterns observed at the free surface of synthetic and biological chiral nematic liquid crystals, chiral polymer solutions, surfactant-liquid crystal surfaces and membranes, and in frozen biological plywoods. The present results can inspire

design and fabrication of complex surface patterns with the possible potentials in optical, high friction, and thermal applications.

REFERENCES

[1] S. Vignolini, E. Moyroud, B.J. Glover, and U. Steiner. Analysing photonic structures in plants. *J. R. Soc. Interface*, 10, 2013.

[2] P.J. Willcox, S.P. Gido, W. Muller, and D.L. Kaplan. Evidence of a cholesteric liquid crystalline phase in natural silk spinning processes. *Macromolecules*, 29:5106–5110, 1996.

[3] V. Sharma, M. Crne, J.O. Park, and M. Srinivasarao. Structural origin of circularly polarized iridescence in jeweled beetles. *Science*, 325:449–451, 2009.

[4] T.L. Tan, D. Wong, and P. Lee. Iridescence of a shell of mollusk haliotis glabra. *Opt. Express*, 12:4847–4854, 2004.

[5] A.R. Parker. Discovery of functional iridescence and its coevolution with eyes in the phylogeny of ostracoda (crustacea). *Proc. R. Soc. B Biol. Sci.*, 262:349–355, 1995.

[6] A.R. Parker and N. Martini. Diffraction gratings in caligoid (crustacea: Copepoda) ecto-parasites of large fishes. *Mater. Today: Proc.*, 1:138–144, 2014.

[7] V. Sharma, M. Crne, J.O. Park, and M. Srinivasarao. Bouligand structures underlie circularly polarized iridescence of scarab beetles: A closer view. *Mater. Today: Proc.*, 1:161–171, 2014.

[8] P. Vukusic, J.R. Sambles, and C.R. Lawrence. Structural colourcolour mixing in wing scales of a butterfly. *Nature*, 404:457, 2000.

[9] D.W. Gould, K.S.and Lee. Physical and ultrastructural basis of blue leaf iridescence in four malaysian understory plants. *Am. J. Bot.*, 83:45–50, 1996.

[10] R.M. Graham, D.W. Lee, and K. Norstog. Physical and ultrastructural basis of blue leaf iridescence in 2 neotropical ferns. *Am. J. Bot.*, 80:198–203, 1993.

[11] H.M. Whitney, M. Kolle, P. Andrew, L. Chittka, U. Steiner, and B.J. Glover. Floral iridescence, produced by diffractive optics, acts as a cue for animal pollinators. *Science*, 323:130–133, 2009.

[12] M. Urbanski, C.G. Reyes, J. Noh, A. Sharma, Y. Geng, V.S.R. Jampani, and J.P.F. Lagerwall. Liquid crystals in micron-scale droplets, shells and fibers. *J. Phys. Condens. Matter*, 29:133003, 2017.

[13] M. Mitov. Cholesteric liquid crystals in living matter. *Soft Matter*, 13:4176–4209, 2017.

[14] A.D. Rey. Liquid crystal models of biological materials and processes. *Soft Matter*, 6:3402–3429, 2010.

[15] Y. Bouligan. Twisted fibrous arrangements in biological-materials and cholesteric mesophases. *Tissue Cell*, 4:189–217, 1972.

[16] A.C. Neville. *Biology of Fibrous Composites: Development Beyond the Cell Membrane*. Cambridge University Press, New York, NY, USA, 1993.

[17] A.D. Rey, E.E. Herrera-Valencia, and Y.K. Murugesan. Structure and dynamics of biological liquid crystals. *Liq. Cryst.*, 41:430–451, 2014.

[18] A.D. Rey and E.E. Herrera-Valencia. Liquid crystal models of biological materials and silk spinning. *Biopolymers*, 97:375–396, 2012.

[19] Y.K. Murugesan, D. Pasini, and A.D. Rey. Self-assembly mechanisms in plant cell wall components. *J. Renew. Mater.*, 3:56–72, 2015.

[20] J.P. Canejo, N. Monge, C. Echeverria, S.N. Fernandes, and M.H. Godinho. Cellulosic liquid crystals for films and fibers. *Liq. Cryst. Rev.*, 5:86–110, 2017.

[21] P. Rofouie, M. Alizadehgiashi, H. Mundoor, I.I. Smalyukh, and E. Kumacheva. Self-assembly of cellulose nanocrystals into semi-spherical photonic cholesteric films. *Adv. Funct. Mater.*, 28, 2018.

[22] P. Rofouie, D. Pasini, and A.D. Rey. Nano-scale surface wrinkling in chiral liquid crystals and plant-based plywoods. *Soft Matter*, 11:1127–1139, 2015.

[23] P. Rofouie, D. Pasini, and A.D. Rey. Nanostructured free surfaces in plant-based plywoods driven by chiral capillarity. *Colloids Interface Sci. Commun.*, 1:23–26, 2014.

[24] P. Rofouie, D. Pasini, and A.D. Rey. Tunable nano-wrinkling of chiral surfaces: Structure and diffraction optics. *J. Chem. Phys.*, 143:114701, 2015.

[25] S.N. Fernandes, Y. Geng, S. Vignolini, B.J. Glover, A.C. Trindade, J.P. Canejo, P.L. Almeida, P. Brogueira, and M.H. Godinho. Structural color and iridescence in transparent sheared cellulosic films. *Macromol. Chem. Phys.*, 214:25–32, 2013.

[26] E. Sharon, B. Roman, M. Marder, G.S. Shin, and H.L. Swinney. Mechanics: Buckling cascades in free sheetswavy leaves may not depend only on their genes to make their edges crinkle. *Nature*, 419:579, 2002.

[27] H. Aharoni, Y. Abraham, R. Elbaum, E. Sharon, and R. Kupferman. Emergence of spontaneous twist and curvature in non-euclidean rods: Application to erodium plant cells. *Phys. Rev. Lett.*, 108:238106, 2012.

[28] P. Rofouie, D. Pasini, and A.D. Rey. Multiple-wavelength surface patterns in models of biological chiral liquid crystal membranes. *Soft Matter*, 13:541–545, 2017.

[29] P. Rofouie, D. Pasini, and A.D. Rey. Morphology of elastic nematic liquid crystal membranes. *Soft Matter*, 13:5366–5380, 2017.

[30] P. Rofouie, Z. Wang, and A.D. Rey. Two-wavelength wrinkling patterns in helicoidal plywood surfaces: Imprinting energy landscapes onto geometric landscapes. *Soft Matter*, 14:5180–5185, 2018.

[31] A.G. Cheong and A.D. Rey. Cahn-hoffman capillarity vector thermodynamics for curved liquid crystal interfaces with applications to fiber instabilities. *J. Chem. Phys.*, 117:5062–5071, 2002.

[32] A. Rapini and M. Papoular. Distorsion dune lamelle nmatique sous champ magntique conditions dancrage aux parois. *J. Phys. Colloq.*, 30:C4–54–C4–56, 1969.

[33] A.D. Rey. Capillary models for liquid crystal fibers, membranes, films, and drops. *Soft Matter*, 3:1349–1368, 3.

[34] V.A. Belyakov, D.V. Shmeliova, and S.V. Semenov. Towards the restoration of the liquid crystal surface anchoring potential using grandgean-cano wedge. *Mol. Cryst. Liq. Cryst.*, 657:34–45, 2017.

[35] A.D. Rey. Nemato-capillarity theory and the orientation-induced marangoni flow. *Liq. Cryst.*, 26:913–917, 1999.

[36] A.D. Rey. Marangoni flow in liquid crystal interfaces. *J. Chem. Phys.*, 110:9769–9770, 1999.

[37] R. Eelkema, M.M. Pollard, N. Katsonis, J. Vicario, D.J. Broer, and B.L. Feringa. Rotational reorganization of doped cholesteric liquid crystalline films. *J. Am. Chem. Soc.*, 128:14397–14407, 2006.

[38] X.G. Yang, J. Li, and Q. Forest, M.G. andWang. Hydrodynamic theories for flows of active liquid crystals and the generalized onsager principle. *Entropy*, 18:202, 2016.

[39] Q. Forest, M.G. andWang and R.H. Zhou. Kinetic theory and simulations of active polar liquid crystalline polymers. *Soft Matter*, 9:5207–5222, 2013.

[40] H.R. Brand, H. Pleiner, and D. Svensek. Dissipative versus reversible contributions to macroscopic dynamics: The role of time-reversal symmetry and entropy production. *Rheol. Acta*, 57:773–791, 2018.

[41] A.D. Rey. Theory of linear viscoelasticity of chiral liquid crystals. *Rheol. Acta*, 35:400–409, 1996.

[42] A.D. Rey. Theory of linear viscoelasticity of cholesteric liquid crystals. *J. Rheol.*, 44:855–869, 2000.

[43] D.W. Hoffman and J.W. Cahn. Vector thermodynamics for anisotropic surfaces 1. fundamentals and application to plane surface junctions. *Surf. Sci.*, 31:368–388, 1972.

[44] A.D. Rey. Mechanical model for anisotropic curved interfaces with applications to surfactant-laden liquid-liquid crystal interfaces. *Langmuir*, 22:219–228, 2006.

[45] F.I. Fedorov. Covariant description of the properties of light beam. *J. Appl. Spectrosc.*, 2:344–351, 1965.

[46] A.H. Sihvola. *Electromagnetic Mixing Formulas and Applications*. The Institution of Engineering and Technology, London, UK, 1999.

CHAPTER 3
Mechano-Geometry of Nano-wrinkling in Cholesteric Liquid Crystal Surface

Article under review

Preface: In Chapter 2, we captured the essential mechanisms of surface wrinkling patterns, the capillary pressure profile as well as the relationship between them. In Chapter 3, we derive two alternative but complementary methods to the model proposed in Chapter 2. In addition, we propose a novel approach involving the topology of capillary vectors and the surface topology to investigate novel mechano-geometry relationships. We find that the winding number of the topology of the capillary vectors implies the periodicity of surface wrinkling patterns, thus serving as an invariant between the mechanical frame and the geometric frame.

Abstract: Biological plywoods are multifunctional fibrous composites materials, ubiquitous in nature. The chiral fibrous organization is found in chitin (insects), cellulosics (plants) and collagen I (cornea and bone of mammals) and is a solid analogue of that of cholesteric liquid crystals. The surface and interfaces of plywoods are distinguished by hierarchical topographies and nanowrinkling. In this paper, we present a theory to model the emergence of these surfaces and interfaces using novel liquid crystal-based shape equations that directly connect material properties with geometric wrinkling. The model applies to liquid crystal precursors of the plywood solid analogues. We focus on wrinkling geometry, wrinkling mechanics, and

the mechano-geometry relationships that underlie multifunctionality ubiquitous in biological surfaces. Scaling wrinkling laws that connect mechanical pressures and stresses to folding and bending are formulated and quantified. A synthesis of the connections between mechanics and geometry is achieved using the topology of stress curves and curvature of the wrinkles. Taken together the results show that anchoring is a versatile surface morphing mechanism with a rich surface bending stress field, two ingredients behind many potential multifunctionalities.

Keywords: cholesteric liquid crystal; wrinkling geometry; surface mechanics; mechano-geometry relationship

3.1 Introduction

Cholesteric liquid crystalline phase can be widely found throughout nature [1, 2, 3, 4]. A distinguishing difference between cholesteric liquid crystals (CLCs) and other liquid crystal [5] is that CLCs are macroscopically (µm-range) chiral with a spatially periodic structure, which ensures the existence of some unique properties such as optical [6] and tribilogical [7] response. The cholesteric material is characterized by the orientation of the helix vector, the handedness (+/−) and the pitch (periodicity) length P_0 [3]. The pitch P_0 dependence on chemical and electromagnetic fields is the source of a rich sensor/actuator capabilities. In this work we focus on the interaction of the orientation structure of cholesteric helix with the geometry of a free surface and seek to elucidate the coupling mechanisms between elastic pressures generated from surface orientation gradients and surface wrinkling geometry. Since cholesterics have periodic structures one finds periodic wrinkling, but as we show in this work the observed geometric periodicity depends on the anisotropy of the surface tension,

generally known as anchoring [8, 9, 10]. In particular in this paper we explore how symmetry breaking from higher order harmonics in the anisotropic surface tension creates more complex wrinkling than a single sinusoidal profile.

To describe wrinkling in anisotropic soft matter surfaces we use the capillary vector methodology. The capillary vector method is widely used in crystalline and hard matter, which, after modification, can also be applied to soft matter materials and processes such as the analysis of Rayleigh fiber instabilities in liquid crystals [13], triple lines [14], wetting, and more [10]. In this paper, we extend this method to predict wrinkling patterns found in CLC free surfaces, given a certain unit vector director field $\mathbf{n}$, which characterizes the main average molecular orientation. The Cahn-Hoffman capillary vector [15, 16] $\boldsymbol{\Xi} := \nabla(r\gamma)$, is defined by the gradient of the product between the magnitude of position vector $\mathbf{r}$ and surface energy γ, and is the core element of this paper. The Cahn-Hoffman capillary vector method yields analogies and direct correspondences in many fields and processes. For example, the Maxwell-Lamé equation [17] in optical-elasticity research has the same form as Eq. (3.28) in this paper, which is related to the principal surface stresses. On large spatial scales, we find that geological pattern formation is described by ad hoc geometric relations [18], that emerge naturally in the Cahn-Hoffman capillary vector method formulated here.

Fig. 3–1 is a schematic explaining the wrinkling geometry and mechanical quantities associated with folding. Given a periodic director field $\mathbf{n}(x)$, we can observe an undulating surface profile $h(x)$, whose intrinsic geometry can be described by its curvature κ. The disclination defects [19] (red λ^+ points) separate the CLC into

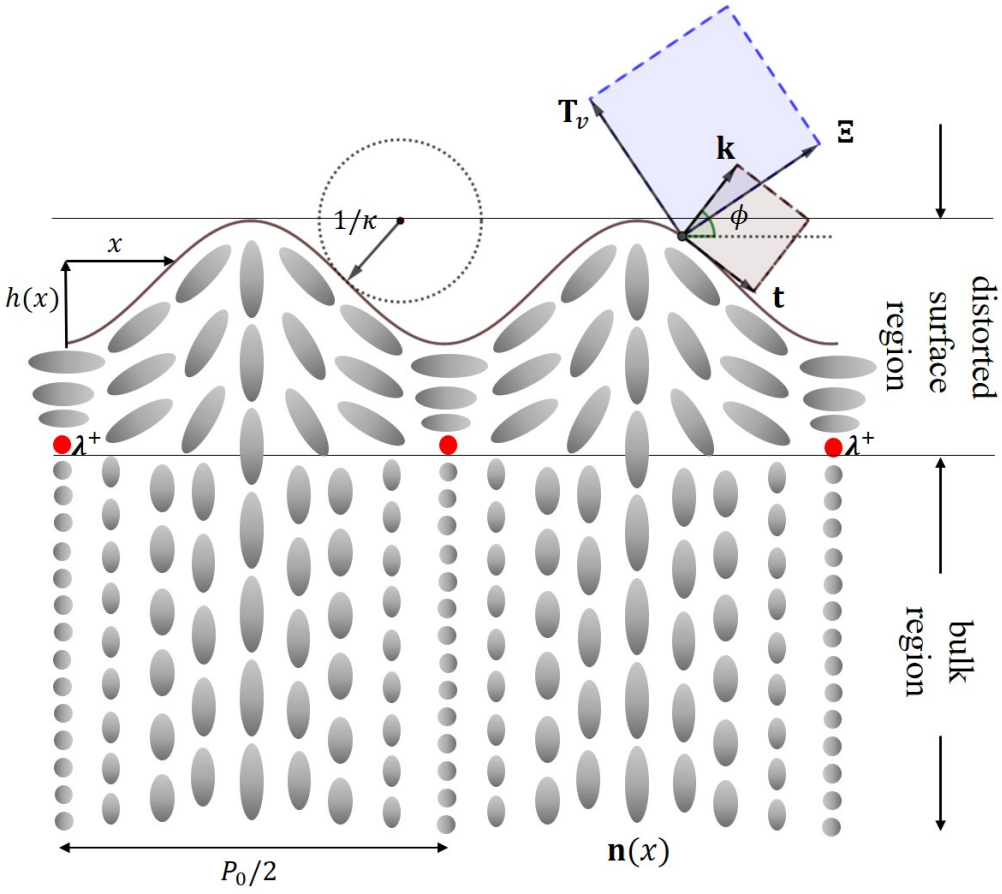

Figure 3–1: Schematic of surface wrinkling of a cholesteric liquid crystal; surface relief ($h(x)$), geometric frame ($\mathbf{t}, \mathbf{k}$), surface curvature (κ), surface mechanical fields ($\boldsymbol{\Xi}, \mathbf{T}_v$); $\mathbf{t}$ is the unit surface tangent vector, $\mathbf{k}$ is the outward unit normal, $\boldsymbol{\mu}$ is the capillary vector, and $\mathbf{T}_v$ is the surface stress vector. Far from the interface the cholesteric helix unit vector $\mathbf{H} = \hat{\boldsymbol{\delta}}_x$ is horizontal and the director field is a pure twist : $\mathbf{n}(x) = (0, n_y, n_z)$; $\mathbf{n} \cdot \mathbf{H} = 0$. In the interfacial region the helical director field uncoils $\mathbf{n}(x) = (n_x, n_y, 0)$ into a planar splay-bend director field and $\mathbf{n} \cdot \hat{\boldsymbol{\delta}}_z = 0$. The surface and bulk region are separated by an array of low energy non-singular λ^+ disclination lines [11, 12]. The chirality of the bulk director is transferred to the surface director in terms of spatial gradient information. The surface curvature is periodic and the period is equal to half the cholesteric pitch $P_0/2$. Capillary vector $\boldsymbol{\Xi}$, generalizes the surface tension under anisotropy. A counterclockwise rotation of $\boldsymbol{\Xi}$ gives the stress vector $\mathbf{T}_v$. The orthonormal geometrical frame ($\mathbf{t}, \mathbf{k}$) is related to the orthogonal mechanical frame ($\boldsymbol{\Xi}, \mathbf{T}_v$) by a dilation-rotation transformation, as shown in this paper.

two regions: distorted surface region above which surface wrinkling occurs, and bulk region where $\mathbf{n}(x)$ is the director field corresponding to a cholesteric liquid crystal with pitch P_0. Since the surface tension is anisotropic, the Cahn-Hoffman capillary vector $\boldsymbol{\Xi}$ describing the capillarity and surface is a 2-D planar (no torsion is considered) surface vector acting on a surface with outward unit normal $\mathbf{k}$ and unit tangent vector $\mathbf{t}$. The surface stress vector normal to $\boldsymbol{\Xi}$ is $\mathbf{T}_v$. The geometric frame $(\mathbf{t}, \mathbf{k})$ defines a unit square area (gray) and the mechanical frame $(\boldsymbol{\Xi}, \mathbf{T}_v)$ defines another square area (blue) and the connection between geometry and mechanics, which is a central topic in this paper, is the rotation-dilation Jacobian matrix that transforms $(\mathbf{t}, \mathbf{k})$ into $(\boldsymbol{\Xi}, \mathbf{T}_v)$.

In our previous work [11, 12] we first explored wrinkling in CLC surfaces with a simple quadratic anisotropic surface tension known as the Rapini-Papoular model [20]. The key mechanism for wrinkling is based on the fact that energy is minimized with a specific relative angle between the director field $\mathbf{n}$ and the unit surface normal $\mathbf{k}$, or equivalently $(\mathbf{n} \cdot \mathbf{k})$. If the surface director orientation changes $\mathbf{n}(x)$ since CLC are spatially periodic, the surface energy is then minimized by geometric distortions $\mathbf{k}(x)$, that seek to keep the optimal (lowest energy) relative angle between $\mathbf{t}$ and $\mathbf{n}$. Subsequently, inspired by actual surface material properties of liquid crystals, we found that a more complex surface pattern can be described including a higher order quartic term $(\mathbf{n} \cdot \mathbf{k})^4$ in the Rapini-Papoular equation [11, 12]. This previous work [11, 12] showed that to describe experimentally observed two-scale wrinkling, anchoring mechanisms are sufficient and that membrane-anchoring models [21] that also predict two-scale wrinkling are not always necessary. The latter class

of membrane-LC models have two intrinsic length scales (membrane scale and helix pitch) whose ratio defines a folding number; increasing the folding number increases the number of wrinkling length scales, leading to predictions in agreement with the structure of the queen of the night tulip. These membrane-liquid crystal models rely on compressive stress loading to create wrinkling, while the purely anchoring models considered in this paper fold the surface to reduce surface tension.

The formal calculation of wrinkling geometry is based on the solution of the shape equation that essentially balances the capillary pressures with the bulk stress jump [10]. When the latter is zero, the curvature is the ratio of the driving capillary pressure divided by a resistance coefficient. The driving pressure for wrinkling is the director pressure which is unique to liquid crystal surfaces since it originates in surface director gradients $\nabla_s \mathbf{n}$. The origin and underlying nature of this unique but less recognized pressure can be elucidated by using mechanical conservation principles such as least action methods, as done in this paper. The wrinkling formation process is characterized by the surface geometry and the surface stress field. The surface geometry includes the surface relief $h(x)$ and more importantly its first four moments, including skewness and kurtosis [22]. Of special interest to this present paper is predict and compare higher order surface relief moments generated from soft matter elastic instabilities with those of hard materials obtained from abrasion, laser treatments and more [23, 24, 25]. Geometric analysis on its own does not shed light on mechanical driving forces and interfacial stresses. Of particular importance to this present paper is to know and assess the principal stresses that drive wrinkling and construct an atlas of complex Lamé curves [26] that synthesize the action of

the stresses involved. For isotropic surfaces one expects a stress circle, for low order anisotropic surfaces one would expect elliptical Lamé stress curves, but for higher order anisotropy, stress curve intersections are inevitable and reveal the nature of the underlying forces. Lastly, integrating geometry and mechanics, as done in other systems under the name of geometro-mechanics, provides the direct link between surface curvature and principal stresses and encapsulates in one diagram why and how wrinkling emerges.

Based on the above observations and facts, the main objectives of this paper are: (1). Derive complementary Maxwell-Lamé and least action method that lead to the shape equation, highlighting the essential nature of the driving director capillary pressure and its dependence on quadratic and quartic anchoring energies; (2). Characterize the full statistical geometry of wrinkling, including skewness and kurtosis as a function of anchoring, emphasizing connections with hard material surfaces; (3). Present an atlas of Lamé principal stress curves as a function of anchoring, to highlight the mechanical forces behind wrinkling; (4). Present an integrated geometro-mechanics characterization in terms of curvature and surface stress ratio, that augments the understanding obtained from just solving the shape equation.

In this paper, we use the following assumptions: (1). The CLC surface is an infinite 1-D manifold where the Gaussian curvature vanishes (parabolic surfaces). This means we study a periodic planar 2-D space curve instead of a 2-D surface; (2). The model is time-independent and focuses on equilibrium patterns and not on transients that may include convective, Marangoni [27, 28] or back flows (energy minimization

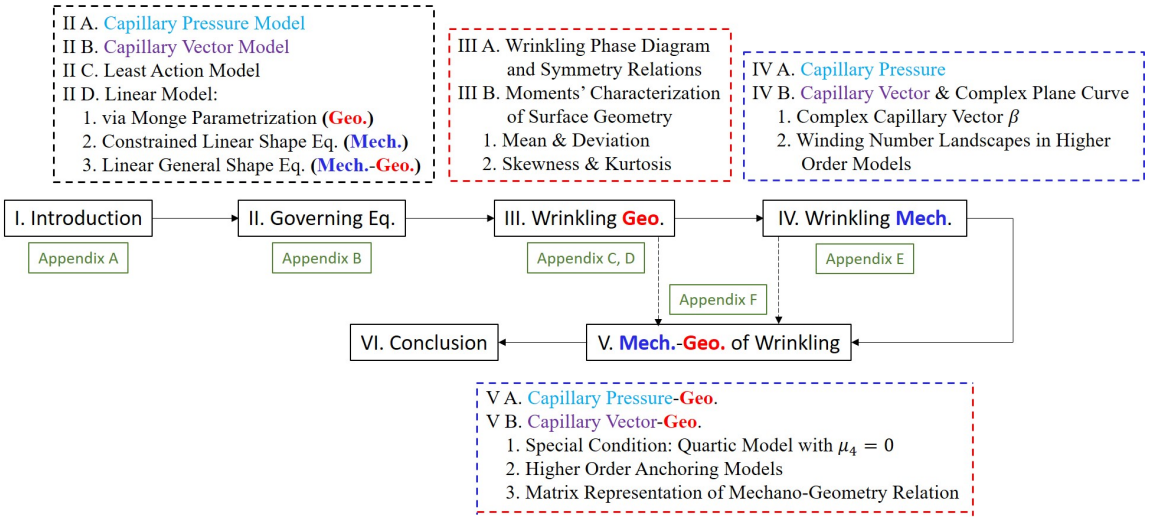

Figure 3–2: Organization and flow of information in this paper. Geo.(red) denotes geometry and Mech.(blue) mechanics.

analysis is included); an energy minimization is included; (3). The surface director field $\mathbf{n}(x)$ is known a priory and based on our previous work and experimental data [29]; (4). Bulk elasticity, known as the elastic correction is negligible as shown previously and corresponds to the easy shape conditions that emerges under zero net capillary pressures. Phenomena and materials inconsistent with these assumptions are not described in this work and are beyond the scope of this paper. The main focus of this paper is on anchoring energies up to quartic order, but few generalizations to six order anchoring are presented when they shed important insights.

This paper is organized as follow and explained by Fig. 3–2. Blue texts represent mechanics (where light blue highlights capillary pressure method and purple highlights capillary vector method), while red texts represent geometry. In Secion 3.2, we derive the governing equation that control the shape of the surface. Then the shape equation will be discussed in terms of three different but complementary models: (1)

The capillary pressure model, (2) the Maxwell-Lamé capillary vector model and (3) the least action model. Each of them provides complementary insights, specially on the driving force (director pressure) and principal stresses; we note that these three models are consistent and equivalent and their solutions predict the same wrinkling. At the end of Sec. 3.2, a linear model is formulated and solved to approximate wrinkling patterns with less numerical computation but with high accuracy, revealing parametric dependence and scaling laws. In Sec. 3.3, we evaluate the statistical geometry of the patterns, including skewness and kurtosis as a function of anchoring [12]. Sec. 3.4 presents a mechanical characterization in terms of principal stress components and Lamé curves. Sec. 3.5 presents the geometro-mechanics in terms of curvature and principal stress ratio which is an efficient method to explain and quantify wrinkling geometry. A mechano-geometry transformation matrix containing the information of both geometry and mechanics is also analyzed in the end of this section. Sec. 3.5 also serves as a bridge between Sec. 3.3 and Sec. 3.4. Sec. 3.6 presents the conclusions. Complete mathematical derivations and proofs, and supporting information are included in the Appendices (green text in Fig. 3–2). We emphasize that under the conditions of this study, wrinkling emerges if and only if the geometric distortions reduce energy as compared with a pure flat geometry with the same director field. In Appendix 3.A, we prove that the total surface energy density does decrease by forming wrinkling patterns.

3.2 Governing Equations

The generalized Rapini-Papoular equation [30, 31] describes the interfacial energy γ as an even expansion

$$\gamma = \gamma_0 + \sum_{j=1}^{\infty} \mu_{2j} (\mathbf{n} \cdot \mathbf{k})^{2i} \tag{3.1}$$

where γ_0 is the isotropic surface energy and μ_{2i} $(i = 1, 2, ..., j)$ are the anchoring coefficients influenced by factors such as temperature, surfactants and more. As mentioned above, $\mathbf{n}$ is the director vector, $\mathbf{k}$ is the surface outward unit normal and P_0 is the helix pitch. The parameters of the model are integrated into a vector $\mathbf{V} = [\boldsymbol{\mu}\ P_0]$ such that $\boldsymbol{\mu} = [\mu_2\ \mu_4\ ...\ \mu_{2n}] \in \Lambda_{2n}$ and $P_0 \in \mathcal{P}$. Hence the parametric space is $\Lambda_{2n} \oplus \mathcal{P} \cong \mathbb{R}^{n+1}$. The order of the wrinkling model is defined by the maximum $2n$, with $n = 1$ denoted quadratic and $n = 2$ the quartic model. As mentioned above, higher order models with lower symmetry have the potential to create more complex wrinkling, but no extensive data appears to be available for higher order coefficients. In this paper we mainly focus on the quartic $(n = 2)$ model where the anchoring coefficient vector is $\boldsymbol{\mu} = [\mu_2\ \mu_4]$, but generalized results are provided when available or when revealing novel results. The symmetry properties of surface wrinkles in terms of the signs of P_0 and $\boldsymbol{\mu} = [\mu_2\ \mu_4]$ was discussed previously.

For completeness we first very briefly presents the bulk elasticity, which becomes non-negligible in surface wrinkling under very short pitches, as in blue phases not considered here. The Ossen-Frank bulk elastic energy density $f_g(\mathbf{n}, \nabla\mathbf{n})$ for a CLC

surface reads [32]

$$\begin{aligned} 2f_g =& K_1(\nabla \cdot \mathbf{n})^2 + K_2(\mathbf{n} \cdot \nabla \times \mathbf{n} - q)^2 + K_3(\mathbf{n} \times \nabla \times \mathbf{n})^2 \\ &+ (K_2 + K_4)[\mathrm{tr}(\nabla \mathbf{n})^2 - (\nabla \cdot \mathbf{n})^2] \end{aligned} \tag{3.2}$$

where $K_i (i = 1, 2, 3)$ are the splay, twist, and bend elastic constants, while K_4 is the saddle-splay elastic constant. Usually we use one-constant approximation such that $K_1 = K_2 = K_3 = K$ while $K_4 = 0$. If $q = 0$, then f_g can be written simply by

$$2f_g = K[(\nabla \cdot \mathbf{n})^2 + \underbrace{(\mathbf{n} \cdot \nabla \times \mathbf{n})^2 + (\mathbf{n} \times \nabla \times \mathbf{n})^2}_{(\nabla \times \mathbf{n})^2} + \underbrace{\mathrm{tr}(\nabla \mathbf{n})^2 - (\nabla \cdot \mathbf{n})^2}_{\nabla \cdot [(\mathbf{n} \cdot \nabla)\mathbf{n} - \mathbf{n}(\nabla \cdot \mathbf{n})]}] = K \left\| \nabla \mathbf{n} \right\|^2 \tag{3.3}$$

The gradient interfacial free energy density γ_{g} is computed by using geometric tensor $\mathbf{g} := (\mathbf{n} \cdot \nabla)\mathbf{n} - \mathbf{n}(\nabla \cdot \mathbf{n})$ as

$$\gamma_g = \frac{1}{2}(K_2 + K_4)\mathbf{k} \cdot \mathbf{g} \tag{3.4}$$

As mentioned above, the Cahn-Hoffman capillary vector [15, 16] is defined by $\boldsymbol{\Xi} := \nabla(r\gamma)$, where r is the magnitude of position vector $\mathbf{r}$. $\boldsymbol{\Xi}$ describes the thermodynamics of an interface, which can be decomposed along vector $\mathbf{k}$ and $\mathbf{t}$ such that normal capillary vector $\boldsymbol{\Xi}_\perp = \Xi_\perp \mathbf{k}$ and tangent capillary vector $\boldsymbol{\Xi}_\parallel = \Xi_\parallel \mathbf{t}$. Notice that $d(r\gamma) = \nabla(\mathbf{r}\gamma) \cdot d\mathbf{r}$ so we have

$$r d\gamma + \gamma dr = \boldsymbol{\Xi} \cdot d(r\mathbf{k}) = r\boldsymbol{\Xi} \cdot d\mathbf{k} + \boldsymbol{\Xi} \cdot \mathbf{k} dr \tag{3.5}$$

Eq. (3.5) yields, for the quartic model, two components

$$\boldsymbol{\Xi}_{\perp} = \gamma \mathbf{k} = \gamma_0 \mathbf{k} + [\mu_2 + \mu_4(\mathbf{nn} : \mathbf{kk})](\mathbf{nn} : \mathbf{kk})\mathbf{k} \tag{3.6}$$

$$\boldsymbol{\Xi}_{\parallel} = \mathbf{I}_s \cdot \frac{\partial \gamma}{\partial \mathbf{k}} = [2\mu_2 + 4\mu_4(\mathbf{nn} : \mathbf{kk})](\mathbf{nn} : \mathbf{kt})\mathbf{t} \tag{3.7}$$

where $\mathbf{I}_s = \mathbf{I} - \mathbf{kk}$ is the surface dyadic and $\mathbf{I}$ the unit dyadic. We note that if μ_2 appears in the normal vector in Eq. (3.6) then $2\mu_2$ appears in the tangential vector in Eq. (3.7) and the same for μ_4. This multiplicative effect affects wrinkling. Also the quartic anchoring in Eq. (3.6, 3.7) is modulated by $(\mathbf{nn} : \mathbf{kk})$, introducing nonlinearity into the quartic coefficient.

The interfacial static force balance requires that the following equation holds on CLC/air interface [33, 34, 27]

$$-\mathbf{k} \cdot (\mathbf{T}^a - \mathbf{T}^b) = \nabla_s \cdot \mathbf{T}_s \tag{3.8}$$

where $\mathbf{T}^{a/b}$ represent the total stress tensor in the air (a) and in the bulk (b) of CLC phase. $\nabla_s = \mathbf{I}_s \cdot \nabla$ is the surface gradient operator and $\mathbf{T}_s$ is the interface stress tensor. $\mathbf{T}^{a/b}$ are given by

$$\mathbf{T}^a = -p^a \mathbf{I} \tag{3.9}$$

$$\mathbf{T}^b = -(p^b - f_g)\mathbf{I} + \mathbf{T}^E \tag{3.10}$$

where $p^{a/b}$ are the hydrostatic pressures. The Ericksen stress tensor $\mathbf{T}^E$ is given by

$$\mathbf{T}^E = -\frac{\partial f_g}{\partial \nabla \mathbf{n}} \cdot (\nabla \mathbf{n})^{\intercal} \tag{3.11}$$

The projection of Eq. (3.8) along $\mathbf{k}$ yields the well-known shape equation

$$\underbrace{(p^a - p^b) + f_g + \mathbf{kk} : \left[-\frac{\partial f_g}{\partial \nabla \mathbf{n}} \cdot (\nabla \mathbf{n})^\intercal \right]}_{\text{Stress Jump, SJ}} = \underbrace{\nabla_s \cdot \mathbf{T}_s \cdot \mathbf{k}}_{-p_c} \tag{3.12}$$

where stress jump, SJ is the total normal stress jump, and p_c is the capillary pressure. Assume $p^a - p^b = 0$ and denote the rest of the term on the left hand side as the elastic correction. We next show that for the case at hand we can safely neglect SJ. Recall the interfacial torque balance equation [35, 36]

$$-\mathbf{h} + \mathbf{k} \cdot \frac{\partial f_g}{\partial \nabla \mathbf{n}} = \lambda^s \mathbf{n} \tag{3.13}$$

where λ^s is the Lagrangian multiplier and $\mathbf{h}$ is the surface molecular field composed by two parts

$$\mathbf{h} = \underbrace{-\frac{\partial \gamma_{\text{an}}}{\partial \mathbf{n}}}_{\mathbf{h}_{\text{an}}} \underbrace{-\frac{\partial \gamma_g}{\partial \mathbf{n}} + \nabla_s \cdot \left(\frac{\partial f_g}{\partial \nabla_s \mathbf{n}} \right)}_{\mathbf{h}_g} \tag{3.14}$$

where $\mathbf{h}_{\text{an}}$ is the anisotropic component and $\mathbf{h}_g$ is related to the gradient. Multiply by $(\nabla \mathbf{n})^\intercal$ on both sides of Eq. (3.13). The torque balance equation can be rewritten as

$$-\mathbf{h} \cdot (\nabla \mathbf{n})^\intercal + \mathbf{k} \cdot \mathbf{T}^E = \mathbf{0} \tag{3.15}$$

which implies that surface director torque is balanced by the bulk stress force. Thus, we can compute $\mathbf{kk} : \mathbf{T}^E$ by $\mathbf{hk} : (\nabla \mathbf{n})^\intercal$

$$\mathbf{hk} : (\nabla \mathbf{n})^\intercal = \left[-\frac{\partial \gamma_{\text{an}}}{\partial \mathbf{n}} - \frac{\partial \gamma_g}{\partial \mathbf{n}} + \nabla_s \cdot \left(\frac{\partial \gamma_g}{\partial \nabla_s \mathbf{n}} \right) \right] \cdot (\nabla \mathbf{n})^\intercal \cdot \mathbf{k} \tag{3.16}$$

which in our case vanishes. Only bulk energy density f_g contributes to the stress jump SJ, which is negligible if helix pitch P_0 is greater than $1\,\mu\text{m}$ [20]. Thus the shape Eq. (3.12) reduces to vanishing total capillary pressure $p_c = 0$.

We parametrize the relevant vector fields as follows: $\mathbf{n} = [\cos qx \;\; \sin qx]$, $\mathbf{t} = [\sin\phi \;\; -\cos\phi]$ and $\mathbf{k} = [\cos\phi \;\; \sin\phi]$, where the rectangular coordinate frame (x, y) is fixed. The adopted planar surface director field $\mathbf{n}(x)$ is discussed in our previous work and suggested by actual experiments. Here $q = 2\pi/P_0$ is the wave-vector and the actual director angle qx is linear in x. Nonlinear director fields lead to tangentially graded wrinkling, explored previously for the quadratic model [37].

3.2.1 Capillary Pressure Model

Here we briefly present the standard shape Eq. (3.12) in terms of the capillary pressures using the capillary vector Eq. (3.6, 3.7) and its special relation with the surface stress tensor $\mathbf{T}_s$ (see Appendix 3.B) [38]. For our cylindrical surface ($\mathbf{I}_s = \mathbf{tt}$) the relation between stress tensor $\mathbf{T}_s$ and Cahn-Hoffman capillary vector $\boldsymbol{\Xi}$ is

$$\mathbf{T}_s = \boldsymbol{\Xi} \cdot (\mathbf{ktt} - \mathbf{ttk}) = \underbrace{\Xi_\perp \mathbf{tt}}_{\mathbf{T}_N} \underbrace{-\Xi_\parallel \mathbf{tk}}_{\mathbf{T}_B} \tag{3.17}$$

where $\mathbf{T}_N$ is the normal stress component and $\mathbf{T}_B$ is the bending stress component. Bending stresses are characteristic of LC surfaces and interfaces due to anchoring and reflect the fact that the surface energy can be changed through area rotations [10]. The sign of $\mathbf{T}_B$ is opposite to that of $\boldsymbol{\Xi}_\perp$ because bending stress is positive when creating negative curvature while $\boldsymbol{\Xi}_\perp$ is along the outward unit normal $\mathbf{k}$. The stress

vector $\mathbf{T}_v$ acting on the surface edge is

$$\mathbf{T}_v = \mathbf{t} \cdot \mathbf{T}_s = \Xi_\perp \mathbf{t} - \Xi_\parallel \mathbf{k} = \boldsymbol{\Xi} \cdot \mathbf{R} \tag{3.18}$$

where $\mathbf{R}$ is the rotation matrix corresponding to an counterclockwise $\pi/2$ rotation along the $\mathbf{b} = \mathbf{t} \times \mathbf{k}$ direction such that $\mathbf{R} = \mathbf{tk} - \mathbf{kt}$. If we replace Eq. (3.12) with Eq. (3.17), shape equation in the language of capillary pressures reads [35]

$$p_c = \nabla_s \cdot \boldsymbol{\Xi} = \underbrace{\frac{\partial \boldsymbol{\Xi}_\perp}{\partial \mathbf{k}} : \nabla_s \mathbf{k}}_{\text{dilation}} + \underbrace{\frac{\partial \boldsymbol{\Xi}_\parallel}{\partial \mathbf{k}} : \nabla_s \mathbf{k}}_{\text{rotation}} + \underbrace{\frac{\partial \boldsymbol{\Xi}_\parallel}{\partial \mathbf{n}} : \nabla_s \mathbf{n}}_{\text{director}} \tag{3.19}$$

where $(\partial_{\mathbf{n}} \boldsymbol{\Xi}_\perp : \nabla_s \mathbf{k})$ vanishes since γ is a function of $(\mathbf{n} \cdot \mathbf{k})$. Eq. (3.19) shows that there are three distinct capillary pressures. The first term on the right hand side characterizes the capillary pressure due to area change denoted by dilation pressure P_{dil}, which is the standard Laplace pressure. The second term is the rotation pressure P_{rot} due to area rotation relative to a given director field. In crystal surfaces this pressure is denoted by Herrings pressure. The last term is the director capillary pressure P_{dir}, which is the driving force that causes wrinkling patterns and is generated by surface director gradients and is unique to liquid crystals [10].

Expanding Eq. (3.19) we obtain a non-linear first order ODE for the surface normal angle ϕ

$$\frac{\kappa}{\sin\phi} = \frac{d\phi}{dx} = \frac{1}{\sin\phi} \frac{F_{\text{Dr}}}{F_{\text{Rs}}} \tag{3.20}$$

where κ is the surface curvature defined by $d\phi/ds$ and s is the arc-length. In Eq. (3.20) the driving force F_{Dr} and resistance F_{Rs} are expressed in the quartic

model by

$$F_{\mathrm{Dr}} = 2[\mu_2 + 2\mu_4(\mathbf{nn} : \mathbf{kk})] \left(\mathbf{n} \otimes \frac{\partial \mathbf{n}}{\partial s} : \mathbf{tk} \right) + 2[\mu_2 + 6\mu_4(\mathbf{nn} : \mathbf{kk})] \left(\mathbf{n} \otimes \frac{\partial \mathbf{n}}{\partial s} : \mathbf{kt} \right) \tag{3.21}$$

$$F_{\mathrm{Rs}} = \gamma_0 + \mu_2[2(\mathbf{nn} : \mathbf{tt}) - (\mathbf{nn} : \mathbf{kk})] + 3\mu_4(\mathbf{nn} : \mathbf{kk})[4(\mathbf{nn} : \mathbf{tt}) - (\mathbf{nn} : \mathbf{kk})] \tag{3.22}$$

The boundary condition for the first order ODE Eq. (3.20) is $\phi|_{x=0} = \pi/2$. Also notice that $\mathbf{nn} : \mathbf{tt} + \mathbf{nn} : \mathbf{kk} = 1$ so $\mathbf{n} \cdot \mathbf{t}$ and $\mathbf{n} \cdot \mathbf{k}$ are not independent in the case of the planar splay-bend surface director field studied here. Eq. (3.20) implies that surface curvature κ is measured by the quotient between F_{Dr} and F_{Rs}. It can be verified that

$$\int_0^{P_0} \frac{F_{\mathrm{Dr}}}{F_{\mathrm{Rs}}} \, ds = 0 \tag{3.23}$$

guaranteed by Gauss-Bonett theorem. Finally surface relief h can be computed by

$$h(s) = -\int_0^s \cot \phi(x) \, dx \tag{3.24}$$

We note that to convert $h(s)$ to $h(x)$ or any other function $x(s)$ we just use $dx = ds \sin \phi$.

3.2.2 Capillary Vector Model

Defining $\mathbf{b} = \mathbf{t} \times \mathbf{k}$, a Frenet-Serret frame can be constructed

$$\frac{d}{ds} \begin{bmatrix} \mathbf{t} \\ \mathbf{k} \\ \mathbf{b} \end{bmatrix} = \begin{bmatrix} 0 & \kappa & 0 \\ -\kappa & 0 & \tau \\ 0 & -\tau & 0 \end{bmatrix} \begin{bmatrix} \mathbf{t} \\ \mathbf{k} \\ \mathbf{b} \end{bmatrix} \tag{3.25}$$

where τ represents torsion which is 0 in this paper as we only consider planar curves. Next we apply Frenet-Serret frame and rewrite Eq. (3.19) as follows

$$\nabla_s \cdot \boldsymbol{\Xi} = \left[\left(\frac{\partial \Xi_{\parallel}}{\partial s} - \kappa \Xi_{\perp} \right) \mathbf{t} + \left(\frac{\partial \Xi_{\perp}}{\partial s} + \kappa \Xi_{\parallel} \right) \mathbf{k} \right] \cdot \mathbf{t} \tag{3.26}$$

Using the relative angle $\theta = \phi - qx$, there is an alternating structure

$$\frac{\partial \Xi_{\perp}}{\partial \theta} + \Xi_{\parallel} = 0 \tag{3.27}$$

which relates the principal stress components $(\Xi_{\parallel}, \Xi_{\perp})$. Since the magnitude of $\Xi_{\perp}$ is γ, we are able to link surface energy with surface curvature by a single expression

$$\Upsilon \circ \gamma = \kappa, \text{where } \Upsilon(\gamma) = -\frac{1}{\gamma} \frac{\partial}{\partial s} \left(\frac{\partial \gamma}{\partial \theta} \right) \tag{3.28}$$

Eq. (3.28) is the general shape equation. It is a general form not only because γ is not explicitly expressed, but also shares common structure with Maxwell-Lamé equation in the study of optical-elasticity [17]. If we denote $\Sigma = ds/d\theta$, where Σ is just a coordinate transformation and Eq. (3.28) is a second order ordinary differential equation. In Sturm-Liouville form it reads:

$$\frac{d}{ds} \left(\frac{d\gamma}{ds} \right) + \kappa \Sigma^{-1} \gamma = 0 \tag{3.29}$$

Comparing the two versions of the shape Eq. (3.19) and Eq. (3.28) we can see that the capillary pressure model highlights the role of director pressure P_{dir} (Eq. (3.19)) and the Maxwell-Lamé model (Eq. (3.26, 3.27)) highlights the principal stresses. Finally Eq. (3.29) shows the Laplacian ∇^2 in arc-length space of the surface energy

γ is proportional to the capillary dilation pressure $\kappa\gamma$ and hence periodicity in γ is connected to periodicity in κ.

3.2.3 Least Action Model

Lastly we recast the shape equation into a least action model by identifying the wrinkling Hamiltonian. Consider the following functional S_L reaching extremum

$$S_L = \int \mathcal{L}\, ds = \int \left[\frac{1}{2} \left(\frac{d\gamma}{ds} \right)^2 - \frac{1}{2} \kappa \Sigma^{-1} \gamma^2 + \pounds(s) \right] ds \tag{3.30}$$

The Legendre transformation of $\mathcal{L}$ is

$$\mathcal{H} = \frac{d\gamma}{ds} \frac{\partial \mathcal{L}}{\partial (\frac{d\gamma}{ds})} - \mathcal{L} \left(\gamma, \frac{d\gamma}{ds}, s \right) = \frac{1}{2} \left(\frac{d\gamma}{ds} \right)^2 + \frac{1}{2} \kappa \Sigma^{-1} \gamma^2 - \pounds(s) \tag{3.31}$$

Eq. (3.31) can be considered as the energy of this system. Comparing Eq. (3.31) with the standard equation of a driven pendulum, we found that $d\gamma/ds$ is the wrinkling velocity of the surface, and $\kappa\Sigma^{-1}$ represents its modulus. We then consider $\mathcal{H}$ as the wrinkling Hamiltonian of a CLC surface. It can be verified that its corresponding wrinkling Lagrangian $\mathcal{L}$ satisfies the Euler-Lagrange equation. Then shape equation Eq. (3.29) is simply generated by a variation $\delta S_L = 0$. Each component of $\mathcal{H}$ represents important aspects of wrinkling. The velocity $d\gamma/ds$ tells us how fast the energy changes along s, and κ reflects how curved the surface is, while Σ is just a coordinate transformation so that the first two terms of $\mathcal{H}$ have the same dimension. $\kappa\Sigma^{-1}\gamma^2$ corresponds to a potential energy stored by the surface. In addition, $\pounds(s)$ corresponds to the driving force. It can be verified numerically that $\pounds(s)$ is just the scaled director pressure P_{dir} (see Eq. (3.19)). The least action model

of cholesteric wrinkling shows that anisotropic capillary phenomena can be projected into a pendulum-like equation, as done in isotropic systems.

3.2.4 Linear Model

Linearization leads to solvable shape equations that yield explicit formulae for geometry, mechanics, and mechano-geometry relationships. It turns out that the capillary vector (Eq. (3.6, 3.7)), the capillary pressure model (Sec. 3.2.1), the capillary vector model (Sec. 3.2.2) can be independently linearized giving complementary computational tools and insights. We use an upper tilde to denote linearized quantity and a star subscript for a quantity which is scaled by γ_0. Here we focus on the quartic model $\gamma = \gamma_0 + \mu_2(\mathbf{n}\cdot\mathbf{k})^2 + \mu_4(\mathbf{n}\cdot\mathbf{k})^4$ for concreteness.

Linear Model via Monge Parametrization

Consider an almost-flat surface, naturally there is a trivial solution where $\boldsymbol{\Xi}$ is a constant solution to equation $\nabla_s \cdot \boldsymbol{\Xi} = 0$. Without loss of generality we can choose $\boldsymbol{\Xi} = \gamma_0 \hat{\boldsymbol{\delta}}_y$ which indicates that at $x = s = 0$ the capillary vector (Eq. (3.6, 3.7)) is along the $y-$axis. Using a Monge parametrization of the surface $\mathbf{r} = (x, h(x))$, the tangent unit vector $\mathbf{t}$ in the linear regime is

$$\mathbf{t} \approx \begin{bmatrix} 1 & \nabla_\parallel h \end{bmatrix} \tag{3.32}$$

Multiply $\mathbf{t}$ on both sides of $\boldsymbol{\Xi} = \gamma_0 \hat{\boldsymbol{\delta}}_y$

$$\begin{aligned} \boldsymbol{\Xi}_\parallel \cdot \mathbf{t} + \boldsymbol{\Xi}_\perp \cdot \mathbf{t} &= \gamma_0 \hat{\boldsymbol{\delta}}_y \cdot \mathbf{t} \\ (2\mu_2 + 4\mu_4 \mathbf{nn} : \mathbf{kk})(\mathbf{nn} : \mathbf{kt}) &= \gamma_0 \nabla_\parallel h \end{aligned} \tag{3.33}$$

Integrating on both sides with respect to x, gives a balance between anchoring (see Eq. (3.7)) and capillarity

$$(\mu_2 + \mu_4 \mathbf{nn} : \mathbf{kk})(\mathbf{nn} : \mathbf{kk}) = q\gamma_0 h \tag{3.34}$$

Replacing $\phi = \pi/2$ in Eq. (3.34) we find the explicit equation for the surface relief $\tilde{h}$

$$\tilde{h} = \frac{1}{q}(\mu_{2*} \sin^2 qx + \mu_{4*} \sin^4 qx) \tag{3.35}$$

Eq. (3.35) shows the remarkable result that capillary energy $\gamma_0 qh$ is equivalent to the anchoring energy of the initial flat profile $\mu_2(\mathbf{n} \cdot \hat{\boldsymbol{\delta}}_y)^2 + \mu_4(\mathbf{n} \cdot \hat{\boldsymbol{\delta}}_y)^4$ (see Eq. (3.1)), that is

$$\tilde{\gamma}_* - 1 = q\tilde{h} \tag{3.36}$$

This equation allows direct calculation of all geometric and mechanical quantities of interest and shows that the energy landscape (left hand side) is imprinted onto the surface relief landscape (right hand side). Also we note from Eq. (3.36) that since anchoring coefficients are usually at most 10% of the isotropic tension, the wrinkling generated by a micron-range pitch P_0 is in the nanoscale [11, 12].

Constrained Linear Shape Equation Model

We can also linearize Eq. (3.20) by assuming that the surface unit normal angle is fixed at $\phi = \pi/2$, yielding:

$$\frac{\tilde{\kappa}}{2q} = \frac{1}{2q}\frac{\tilde{F}_{\mathrm{Dr}}}{\tilde{F}_{\mathrm{Rs}}} \approx \frac{1}{2q}\frac{\tilde{F}_{\mathrm{Dr}}}{\gamma_0} = \mu_{2*} \cos 2qx + 2\mu_{4*}(3 \sin^2 qx \cos^2 qx - \sin^4 qx) \tag{3.37}$$

Integrating the equation twice with respect to x we find:

$$\int \left(\int \tilde{\kappa}\, dx \right) dx = \tilde{h} + \text{constant} \tag{3.38}$$

It can be easily verified that the surface relief we obtained from the equation above is exactly the same as that derived from Monge parametrization (Eq. (3.36)). The value of this direct linearization is that reveals the exact relation between curvature κ and the director pressure F_{Dr} (see Eq. (3.20)) and emphasize the point that wrinkling is driven by this unique capillary pressure.

Linear General Shape Equation Model

Examination of the general shape Eq. (3.28) shows that Eq. (3.36) is inevitable.

If we assume that $\phi = \pi/2$ then $d\theta = -qds$ and $dx = ds$. Replace them into Eq. (3.28) and let $\gamma = \gamma_0$ om the left hand side we have

$$-\frac{d^2}{ds^2}\left(\frac{\tilde{\gamma}}{q}\right) = -\frac{d^2}{ds^2}(\tilde{h}\gamma_0) \tag{3.39}$$

which implies that $\tilde{\gamma}/q = \tilde{h}\gamma_0 + C_1 s + C_2$ where C_1 and C_2 are constants. Implementing boundary condition then we verify Eq. (3.36), which is found to be the universal property valid for any anchoring model.

All three methods above yield the same result while they are derived from different approaches: (1) Monge parametrization emerges purely from geometry; (2) Linear shape equation model is derived only by linearizing a shape ODE, an equation reflecting mechanics; and (3) The general shape equation model is an equation links mechanics and geometry. Hence we have established that the mechanics and geometry of wrinkling in cholesteric surfaces are naturally linked.

3.3 Wrinkling Geometry

3.3.1 Wrinkling Phase Diagram and Symmetry Relations

An important aspect of wrinkling geometry is how it reflect the symmetry properties of the linearized shape equations Eq. (3.36, 3.38, 3.39). This will help answer the questions of how the surface relief $h(x)$ profile changes when changing the handedness of the CLC or sign of P_0 and when changing the signs of the anchoring coefficients, since they are not fixed by thermodynamics. We recall that the parameters are $\mathbf{V} = [\boldsymbol{\mu}\ P_0]$. We have previously shown that the wrinkling geometry shows central symmetry in space Λ_{2n} with respect to its origin point [12]. The key idea is that for a parametric vector $\mathbf{V} \in \Lambda_{2n} \oplus \mathcal{P}$ within the linear region, surface relief can be seen as a map taking the value of vector $\boldsymbol{\mu} = [\mu_2\ \mu_4\ \mu_6...]$ and P_0 onto an output pattern. It can be verified that $\tilde{h}$ is multi-linear to $\boldsymbol{\mu}$. However, the j^{th} term in $\tilde{h}$ is $(\mu_{2j} \sin^{2j} qx)/q$, where the wave vector q affects both magnitude as well as periodicity. Hence, the magnitude of $\tilde{h}$ as well as its statistical properties scaled by P_0 such as mean value or standard deviation are linear to all the inputs.

A direct application of this result is the surface profile symmetry relations:

$$\begin{array}{ccccc} \tilde{\gamma}/q & \xrightarrow{-1/q} & \tilde{h}(\boldsymbol{\mu}, P_0) & \xrightarrow{-\Lambda_{2n}} & -\tilde{h}(-\boldsymbol{\mu}, P_0) \\ & & \downarrow{\scriptstyle -\mathcal{P}} & & \downarrow{\scriptstyle -\mathcal{P}} \\ & & -\tilde{h}(\boldsymbol{\mu}, -P_0) & \xrightarrow{-\Lambda_{2n}} & \tilde{h}(-\boldsymbol{\mu}, -P_0) \end{array}$$

For example, changing the signs of all anchoring coefficients and pitch will leave the surface profile intact. On the other hand a pitch inversion will reverse the profile. This could be important in applications when controlling the flatness or peak sharpness present in $h(x)$ is important. Next we evaluate the surface roughness behavior as a function of anchoring coefficients; whenever tractable we present general results

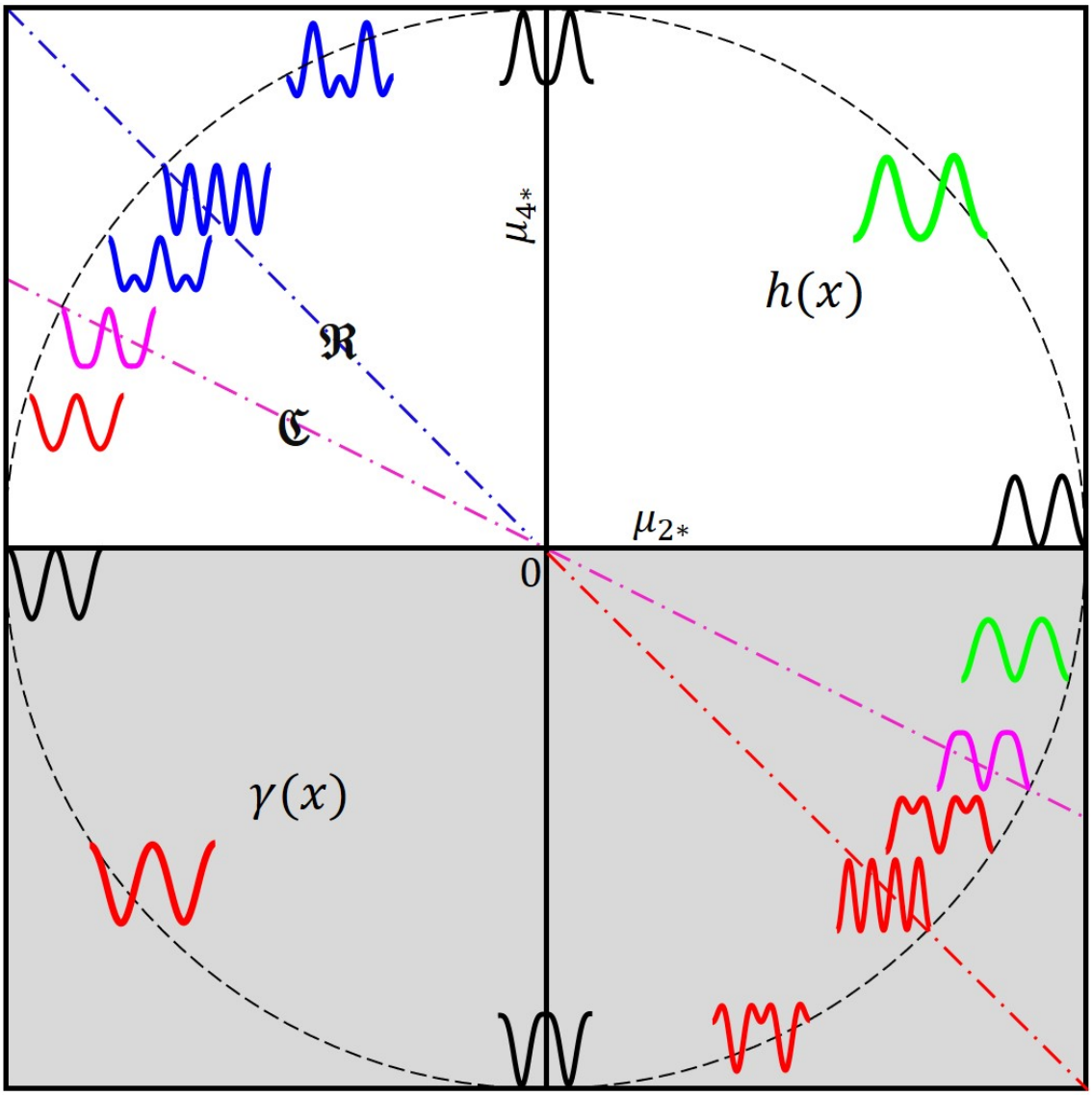

Figure 3–3: Wrinkling phase diagram as a function of anchoring coefficients. The top semicircle shows the surface profile $h(x)$ and the bottom semicircle shows the surface tension profiles $\gamma(x)$. The resonance line $\mathfrak{R}$ is $\mu_{2*} + \mu_{4*} = 0$ and the critical line $\mathfrak{C}$ is $\mu_{2*} + 2\mu_{4*} = 0$ (see text). At the resonance line $\mathfrak{R}$ the quartic and quadratic harmonics is a maximum. The sectors within the $\mathfrak{C}$ and μ_{4*} lines display two waves, and the rest of the sectors only one wave. According to Eq. (3.36) the surface tension γ is proportional to the surface relief $h(x)$ and hence essentially the same; thus we show $h(x)$ on the top semicircle and γ on the bottom semi-circle. The symmetry of the $h(x)$ profiles (or the γ profiles) follow the graphical equations in Sec. 3.3.1.

for $\boldsymbol{\mu} = [\mu_2 \ \mu_4 \ \mu_6 ...]$ but for specificity we concentrate on the quartic anchoring model $\boldsymbol{\mu} = [\mu_2 \ \mu_4]$. Fig. 3–3 shows the wrinkling phase diagram for the quartic model in terms of the two anchoring coefficients. The figure shows the patterns of surface relief profile (upper plane) and energy profile (lower plane with gray shading area) when fixing P_0 as a constant. The circle is $\mu_{2*}^2 + \mu_{4*}^4 = C^2$ where $C \in \mathbb{R}^+$. The resonance line $\mathfrak{R}$ is $\mu_{2*} + \mu_{4*} = 0$ and the critical line C is $\mathfrak{C}$ is $\mu_{2*} + 2\mu_{4*} = 0$. Fig. 3–3 verifies the correspondence between $h(x)$ and $\gamma(x)$ (see Eq.(3.36)), as well as the central symmetry shown in the Λ_4 space. The colors in Fig. 3–3 serve to categorize different regions in Λ_4 where we adapted from previous discussion [12]. The anchoring space is divided into 6 sectors according to the emergence of double wrinkling or single wrinkling, by the vertical $\mu_2 = 0$ line , the oblique resonance line $\mathfrak{R}$, and the oblique critical line $\mathfrak{C}$. Double wrinkling occurs in (a) the first sector of the second quadrant (i.e. between the vertical $\mu_2 = 0$ line and the oblique critical line $\mathfrak{C}$; blue profiles), and in (b) the first sector of the fourth quadrant (i.e. between the vertical $\mu_2 = 0$ line and the oblique $\mathfrak{C}$ critical line; red profiles). In terms of signs $(+-)$ of the anchoring coefficients, double wrinkling only occurs in the $(-+)$ and $(+-)$ sectors of the phase diagram Fig. 3–3. Hence richer double wrinkling is relatively abundant in the anchoring space. Also note that the resonance line $\mathfrak{R}$ denotes maximal interaction between the harmonics and results in single wrinkling. Fig. 3–3 also indicates than in the $(-+)$ mode peaks are up and valley are down , while in the $(+-)$ mode the reverse is true. This important effect is captured by the third moment of the surface height distribution (skewness) discussed below. Finally we see that that signed ratio of the anchoring coefficients is the main variable

controlling wrinkling while Eq.(3.35) indicates that $\boldsymbol{\mu}$ controls the amplitude only. An important close similarity is the shape and curvedness of surfaces [39] with the former given by a curvature ratio, and the latter by the sum of curvature squares.

3.3.2 Moments Characterization of Surface Geometry

A detailed characterization of surface geometry requires specification of the moments of the surface relief $M[n, m]$ with respect to the mean m. We note that the common base line of the surface relief is fixed and defined by the given director filed at $s = 0(\mathbf{n} = \hat{\delta}_x)$ and is equal to $h(s = 0) = 0$ for all cases. We start with the quantities that appear in calculating the moments that characterize wrinkling. The Mclaurin series of $(1 - x)^{-1/2}$ is

$$\frac{1}{\sqrt{1-x}} = \sum_{n=0}^{\infty} \frac{(2n-1)!!}{2^n n!} x^n = \sum_{n=0}^{\infty} \frac{1}{\sqrt{\pi}} \frac{\Gamma(n+\frac{1}{2})}{\Gamma(n+1)} x^n \tag{3.40}$$

where Γ is the gamma function. Let the n^{th} coefficient of x^n be $\mathfrak{b}_n$, and denote dimensionless series $\{\mathfrak{b}_n\}$. Most common values are $\mathfrak{b}_1 = 1/2$, $\mathfrak{b}_2 = 3/8$, $\mathfrak{b}_3 = 5/16$ and $\mathfrak{b}_4 = 35/128$. Next we establish the important relation of the $\mathfrak{b}_n$ to sine integrals that appear when integrating h and its powers (i.e., computing the moments). In the following computations, we always assume $P_0 = 1\,\mu\text{m}$ unless otherwise stated. We find that the n^{th} (n is even) moment of $\sin qx$ satisfies the following identity (consult Appendix 3.C)

$$\int_0^{P_0} \sin^n(qx)\, dx = P_0 \mathfrak{b}_{n/2} \tag{3.41}$$

The statistical parameters to describe surface profile are summarized to Tab. 3–1, where we use standard notation [22]. In Tab. 3–1, we define $M[n, m]$ as the n^{th}

moment of $h(x) - m$ in Λ_4 computed by (see Appendix 3.C)

$$M[n,m] := \frac{1}{P_0}\int_0^{P_0}[h(x)-m]^n\,dx \tilde{=} \sum_{i=0}^{n}\binom{n}{i}(-\tilde{m})^{n-i}\sum_{j=0}^{i}\binom{i}{j}\mu_{2*}^{j}\mu_{4*}^{i-j}\mathfrak{b}_{2i-j} \quad (3.42)$$

This formula reveals the central role $\mathfrak{b}_n$, and also the signs of the anchoring coefficients for odd moments that control up-to-down $h-$profile features.

Table 3–1: Statistics of surface geometry

Parameter	Symbols	Definition	Description
Mean	m	$M[1,0]$	Average value of $h(x)$
Arithmetical Mean	Ra	$M[1,m]$ [1]	Average deviation with absolute value accumulated
Variance	σ^2	$M[2,m]$	Deviation of $h(x)$ with respect to m
Skewness	Rsk	$M[3,m]/\sigma^3$	Measure of the asymmetry
Kurtosis	Rku	$M[4,m]/\sigma^4$	Measure of the tailedness

Mean and Deviation

The mean m represents average line and σ^2 captures the deviation of surface from the mean value. Both σ and Ra describe the deviation from average line. Using linear theory, in quartic model $\tilde{m}$ becomes

$$\tilde{m} = \frac{1}{q}(\mathfrak{b}_1\mu_{2*} + \mathfrak{b}_2\mu_{4*}) \quad (3.43)$$

while $\tilde{\sigma}$ reduces to

$$\tilde{\sigma}^2 = \frac{1}{q^2}[(\mathfrak{b}_2 - \mathfrak{b}_1^2)\mu_{2*}^2 + 2(\mathfrak{b}_3 - \mathfrak{b}_1\mathfrak{b}_2)\mu_{2*}\mu_{4*} + (\mathfrak{b}_4 - \mathfrak{b}_2^2)\mu_{4*}^2] \quad (3.44)$$

[1] Defined as $\frac{1}{P_0}\int_0^{P_0}|h(x)-m|\,dx$, where the square bracket in Eq. (3.42) is replaced with an absolute value

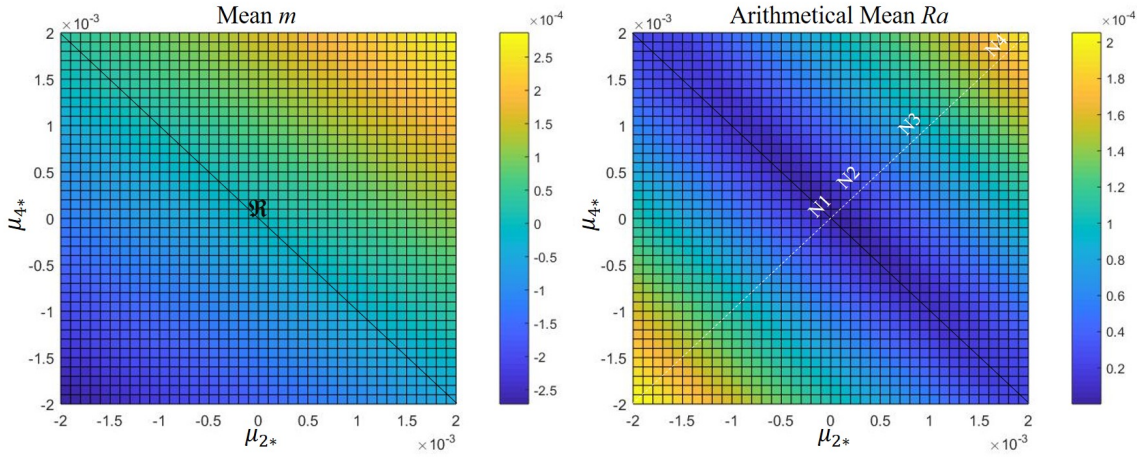

Figure 3–4: Mean value m (left) and arithmetic mean Ra (right) as a function of two dimensionless anchoring coefficients. See Tab. 3–1 and Appendix 3.C for definitions and details. The mean vanishes close to the resonance line and the maximum is along a line normal to this line. The arithmetic mean is a minimum along the resonance line and increases normal to this line. The lables $N1 - N4$ denote characteristic roughness values used to characterize rough surfaces, with $N1$ having low and $N4$ high roughness. The location of $N1 - N4$ in the anchoring diagram shows the practical applicability of anchoring.

Fig. 3–4 shows the numerical solutions (colors correspond to numerical values given in the side bar) of the mean m and arithmetical mean Ra in the parametric plane, obtained from Eq. (3.20, 3.24, 3.42). We can observe that the mean value almost vanishes along the resonance line $\mathfrak{R}$. In addition, due to the symmetry of Λ_4, any two points symmetric with respect to the origin should have the same magnitude but opposite sign of m. For the arithmetical mean Ra, the minimum value occurs along $\mathfrak{R}$, and closer to the origin of Λ_4, a darker color appears in the Ra plot, which corresponds to the fact that weak anchoring gives weak deviation. An important technical application of Ra is to categorize roughness with a grade number N since a high Ra implies a very rough surface. Grade number $N1$ correspond to a 0.025 µm roughness and $N4$ to 0.2 µm [22, 40]. Roughness grade numbers $N1$ to $N4$, in our soft matter material, are shown in Fig. 3–4 (left figure) by assuming the scale of the magnitude of $P_0\mu_{2*}$ is 1 mm. We can see that surface roughness grade number is distributed perpendicular to $\mathfrak{R}$; since $N1$ corresponds to 0.025 µm and $N4$ to 0.2 µm we see that anchoring is compatible with industrial roughness values for reasonable pitch P_0 scales.

We can shed more light into the specific trends shown in Fig. 3–4 by analyzing Eq. (3.42) in conjunction with the wrinkling geometry of the anchoring phase diagram (Fig. 3–3). According to Eq. (3.43) The mean value m can be set to zero by forcing $\mathfrak{b}_1\mu_{2*} = -\mathfrak{b}_2\mu_{4*}$, while according to Eq. (3.44) the standard deviation σ can be arbitrarily close to zero, which corresponds to a flat surface. Hence we choose two parameters along a closed circle (see Fig. 3–5): $\mu_{2*}^2 + \mu_{4*}^2 = C^2$. We seek to find the extreme values of mean and deviation along this characteristic circle. Fig. 3–5 shows

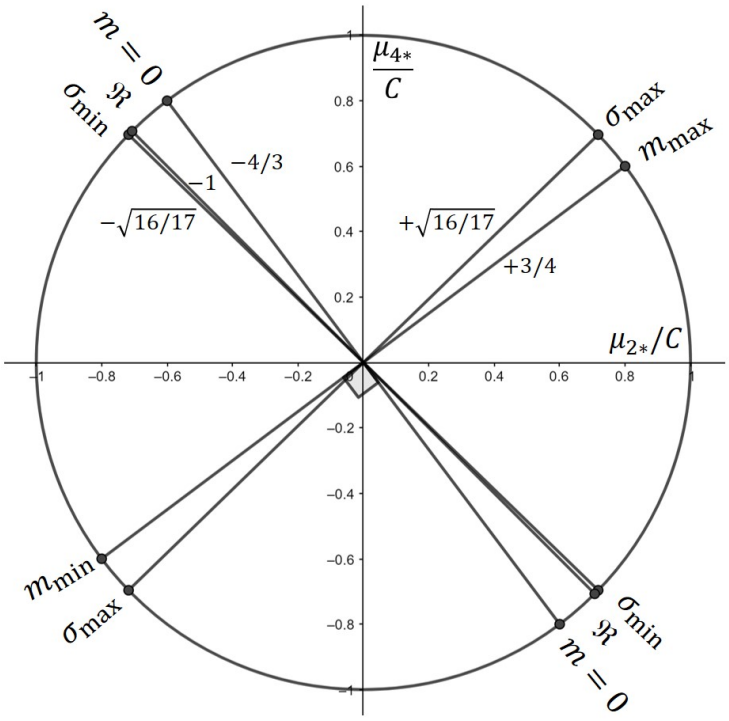

Figure 3–5: Extremum values distribution for m and σ restricted by $\mu_{2*}^2 + \mu_{4*}^2 = C^2$ within Λ_4 space, with number next to each line representing its slope. The mini-max lines crisscrossing the anchoring phase diagram show the versatility of anchoring as a wrinkling force. The radial lines also show that essential wrinkling qualities depend on the ratio of the anchoring coefficients (azimuthal angle in this diagram) and not on C (sum of anchoring amplitudes square or radial direction in this diagram).

that the line along which m vanishes is perpendicular to the line where m reaches extremum. Also the line along which σ reaches maximum is a mirror symmetry of the line where σ reaches a minimum with respect to μ_{4*}/C line.

Since $\mathfrak{b}_j = \mathfrak{b}_{j-1}(1 - \frac{1}{2j})$, so $\mathfrak{b}_j$ contributes less and less as j increases. The monotonic decrease of series $\{\mathfrak{b}_n\}$ is the reason why $m = 0$ requires $|\mu_4| > |\mu_2|$. The numerical solution given by Fig. 3–4 (see color intensity grading and Ni labels) matches our discussion that m essentially vanishes along $\mathfrak{R}$. This important results establishes that the maxima in m corresponds to a $(++)$ mode and the maxima in σ to a $(++)$ and $(--)$ modes.

As expected, we can generalize the extrema characterization to higher order Λ_{2n} anchoring models. Consider a special but realistic condition when each anchoring coefficient μ_{2i} is proportional to $\mathfrak{b}_i$ such that $\mu_{2i*} = \alpha\mathfrak{b}_i$ (α is a non-zero constant); as noted below Eq. (3.44) the coefficients decrease with "i" and hence we are assuming that the anchoring coefficients also decrease with "i". Then $\tilde{m} = \alpha S/q$, where $S = \sum_{i=1}^{n} \mathfrak{b}_i^2$ and anchoring coefficients are restricted on an $n-$sphere $\sum_{i=1}^{n} \mu_{2i*}^2 = C^2$ where C is a positive constant. It can be verified that this special condition is exactly the solution giving the extremum $\tilde{m}$. And the constant can be computed by $\alpha = -C/\sqrt{S}$ (proof is given by Appendix 3.D). The Borsuk-Ulam [41] theorem requires that a vanishing m must exist, corresponding to a $n-1$ dimensional hyperplane $\sum_{i=1}^{n} \mathfrak{b}_i\mu_{2i} = 0$, which is perpendicular to the line represented by this special condition. This important result indicates vanishing m for any anchoring order model. We note that since the director field is fixed at $\mathbf{n}(x = 0) = \hat{\boldsymbol{\delta}}_x$, the zero mean can not be shifted away.

Skewness and Kurtosis

The third order moment, normalized skewness Rsk quantifies the asymmetry of the surface profile, while the fourth order moment, normalized kurtosis Rku intuitively describes the thickness of the tail of the surface profile distribution. Fig. 3–6 shows the numerical computations using Eq. (3.20, 3.24, 3.42) with $P_0 = 1\,\mu\text{m}$. The geometric meaning of Rsk is given by the bottom left $h-$profiles in Fig. 3–6. the positive or negative sign of Rsk represent two asymmetric patterns shown in the figure, where positive skewness indicates a surface with tall peaks and negative skewness indicates a surface with deep valleys. The magnitude of Rsk measures the magnitude of this asymmetry. Fig. 3–6 (left) shows that Rsk vanishes along $\mathfrak{R}$, and almost vanishes in the first quadrant and third quadrant. We can observe that $Rsk > 0$ in the second quadrant and $Rsk < 0$ in the fourth quadrant of Λ_4.

Fig. 3–6 shows the kurtosis surface with intersecting double folds, converging along $\mathfrak{R}$. We can also observe that $Rku \neq 0$ except at $\boldsymbol{\mu} = \mathbf{0}$, where the surface is flat. In the bottom middle profiles of Fig. 3–6, we can see that the geometric meaning of Rku is how much the small tails contribute to the total wave pattern. Rku reaches its minimum along $\mathfrak{R}$, also in the first and third quadrant.

This can be explained since wrinkling waves are identical along $\mathfrak{R}$ and show no difference in the first and third quadrant. Rku displays rotational symmetry in the second and fourth quadrant, hence we only need to analyze the second quadrant. Small tails contribute the most when the surface relief occur in the vicinity of $\mathfrak{R}$ but not exactly along $\mathfrak{R}$. The essential features of the intersecting double folds are as follows. Therefore, if we track Rku along a $1/4$ circle parametrized by $\mu_{2*}^2 + \mu_{4*}^2 = C^2$

where C is a positive constant from $\mu_{2*} = -C$ to $\mu_{2*} = 0$, we should expect Rku to increase initially due to the emergence of small tails, then decreases until the circle reaches $\mu_{2*} = -\sqrt{2}C/2$ since waves are identical along $\mathfrak{R}$, exhibiting a local minimum in kurtosis. If we then continue to move along the 1/4 circle until reaching $\mu_{2*} = 0$ from $\mathfrak{R}$, the process is reversed and we find an increasing and then decreasing Rku. Considering now the Rsk plot (Fig. 3–6 left), we find that the magnitude of Rsk shows the same trends as that of Rku. These insights reveal that the vicinity of the resonance line exhibit higher magnitudes in kurtosis and skewness which affect functionalities such as friction.

Kurtosis Rku as a function of skewness Rsk is shown inte bottom right right panel of Fig. 3–6. The symmetric petal pattern corresponds to a bifolium [42], another classical planar curve associated with biological forms. The importance of this plot is that it reveals the versatility of anchoring-driven wrinkling. Using hard materials and respective processes only specific areas of the kurtosis-skewness plane are achievable [43].

Kurtosis is always below 3 (so called Gaussian profile), indicating a gradually changing surface curvature. The petal pattern is an intrinsic plot, and it does not depend on $\boldsymbol{\mu}$ or P_0. Given a certain $\boldsymbol{\mu}$ and P_0, we can locate a point in $Rsk - Rku$ plot. Points are denser around the bottom point shown in Fig. 3–6, implying that most of the points in Λ_4 are surrounding the minimum Rsk (or Rku), corresponding to the fact that most regions in Λ_4 yield 1-wavelength pattern (2 waves within one period). As for the applications, the $Rsk-Rku$ plot plays an important role in surface science and industry. For example, it is possible to lower static friction coefficients

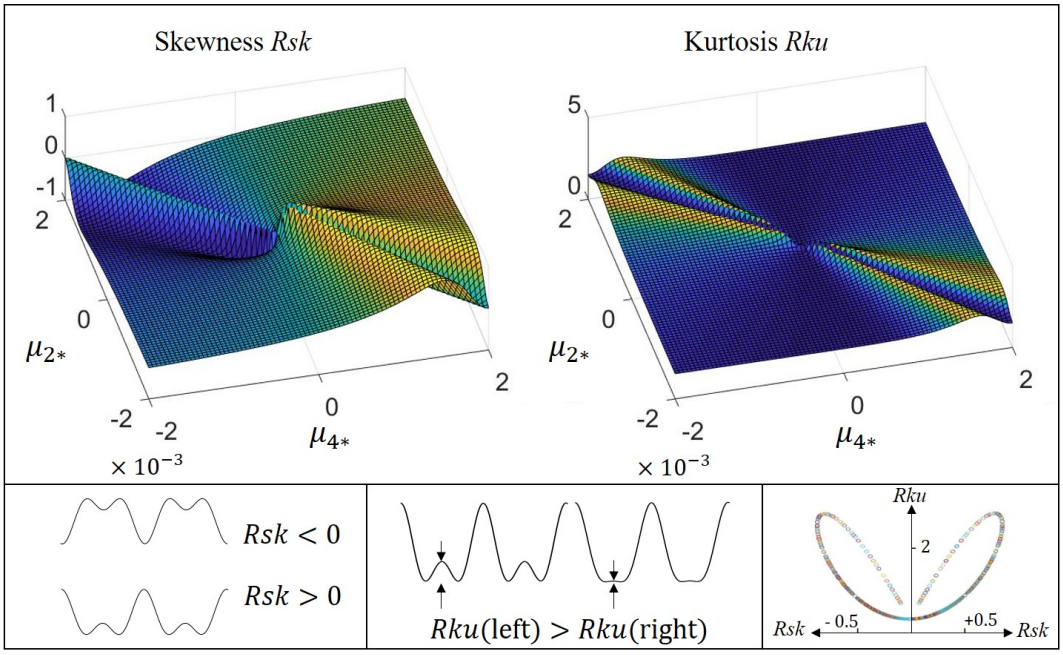

Figure 3–6: Computed skewness Rsk and kurtosis Rku surfaces as a function of the two anchoring coefficients (top two plots). Representative surface profiles with different skewness (bottom left) and kurtosis (middle bottom). Skewness as a function of kurtosis, as the anchoring coefficients change, showing mirror symmetry.

by increasing high Rku while remaining positive Rsk [44]. $Rsk - Rku$ plot is also used to measure the roughness of biological surface topography [45].

3.4 Wrinkling Mechanics

In this section, we characterize wrinkling mechanics using the capillary pressure and the capillary vector $\boldsymbol{\Xi}$. It will be shown that the mechanical information content in the capillary pressures can be expressed in polar coordinates and that the stress state can be quantized by winding numbers W_p of generalized Lamé stress curves.

3.4.1 Capillary Pressure

The mechanics behind surface wrinkling is the cancellation between dilation pressure, rotation pressure and director pressure, as shown in Eq. (3.19). These pressures play different roles in surface wrinkling and are expressed by

$$
\begin{aligned}
P_{\text{dil}} =& -\kappa[1+\mu_{2*}(\mathbf{nn}:\mathbf{kk})+\mu_{4*}(\mathbf{nn}:\mathbf{kk})^2] \\
P_{\text{rot}} =& -\kappa[2\mu_{2*}(\mathbf{nn}:\mathbf{tt}-\mathbf{nn}:\mathbf{kk})+4\mu_{4*}(\mathbf{nn}:\mathbf{kk})(3\mathbf{nn}:\mathbf{tt}-\mathbf{nn}:\mathbf{kk})] \\
P_{\text{dir}} =& 2[\mu_{2*}+2\mu_{4*}(\mathbf{nn}:\mathbf{kk})]\left(\mathbf{n}\otimes\frac{\partial\mathbf{n}}{\partial s}:\mathbf{tk}\right)+2[\mu_{2*}+6\mu_{4*}(\mathbf{nn}:\mathbf{kk})]\left(\mathbf{n}\otimes\frac{\partial\mathbf{n}}{\partial s}:\mathbf{kt}\right)
\end{aligned}
\tag{3.45}
$$

The dilation pressure P_{dil} represents the area dilation effect, which is related to the expansion or shrinkage of surface area (Laplace pressure). The rotation pressure P_{rot} represents a small rotation of surface area, whose contribution to the surface wrinkling is brought by tangential component $\boldsymbol{\Xi}_{\parallel}$ (also known as Herring's pressure). They are two pressures related to the surface hence they both have an explicit κ term in their equations. The director pressure P_{dir} is introduced by director surface gradients, so it does not contain direct geometric curvature information. As above-mentioned the director pressure is the driving force that causes wrinkling patterns in this model.

Fig. 3–7 shows polar plots P_{dil}, P_{dir} and P_{rot} as a function of the relative angle between the unit normal and the director $\theta = \phi - qx$. P_{dil} and P_{dir} dominate the magnitude, and P_{rot} is the small difference between them. The reason is that dilation effect is to the first order proportional to the curvature κ times γ_0; while the rotation effect under small wrinkling conditions is proportional to κ times γ_{an}

and since $\gamma_0 >> \gamma_{an}$, $P_{dil} >> P_{rot}$. Hence, $P_{dil} \approx -P_{dir}$ if we neglect rotation pressure, which implies that dilation pressure and director pressure are always out-of-phase. Another important identity is that the direction of rotation pressure is only dependent to the direction of helix pitch, i.e., $\text{sgn}(P_{rot}) = -\text{sgn}(P_0)$. This relation can be found by Eq. (3.53).

3.4.2 Capillary Vector and Complex Plane Curve

Complex Capillary Vector β

Fig. 3–1 and Eq. (3.18) show that stresses and the capillary vector are related by a simple $\pi/2$ rotation, suggesting the usefulness of using complex analysis , as done here. According to Eq. (3.17) (consult Appendix 3.B) the eigenvalues of the surface stress tensor are $\Xi_\perp$ and $-\Xi_\parallel$. The three tensor invariants are

$$\begin{aligned} I_1 &= \text{tr}\mathbf{T}_s = \Xi_\perp - \Xi_\parallel \\ I_2 &= \tfrac{1}{2}[(\text{tr}\mathbf{T}_s)^2 - (\text{tr}\mathbf{T}_s^2)] = -\Xi_\perp \Xi_\parallel \\ I_3 &= \det\mathbf{T}_s = I_2 \end{aligned} \tag{3.46}$$

Eq. (3.46) implies that any scalar function depending on capillary vectors is independent from rotations of the coordinate system. Define a dimensionless complex capillary number β as

$$\beta = \Xi_{\parallel *} + \Xi_{\perp *} i \tag{3.47}$$

As we show below, β is the core concept whose topology serves as the bridge between geometry and mechanics. If we are moving towards the positive x direction along the arc-length s, $\boldsymbol{\Xi}_\parallel$ stays in the tangent space. This is the reason why we assign $\boldsymbol{\Xi}_\parallel$

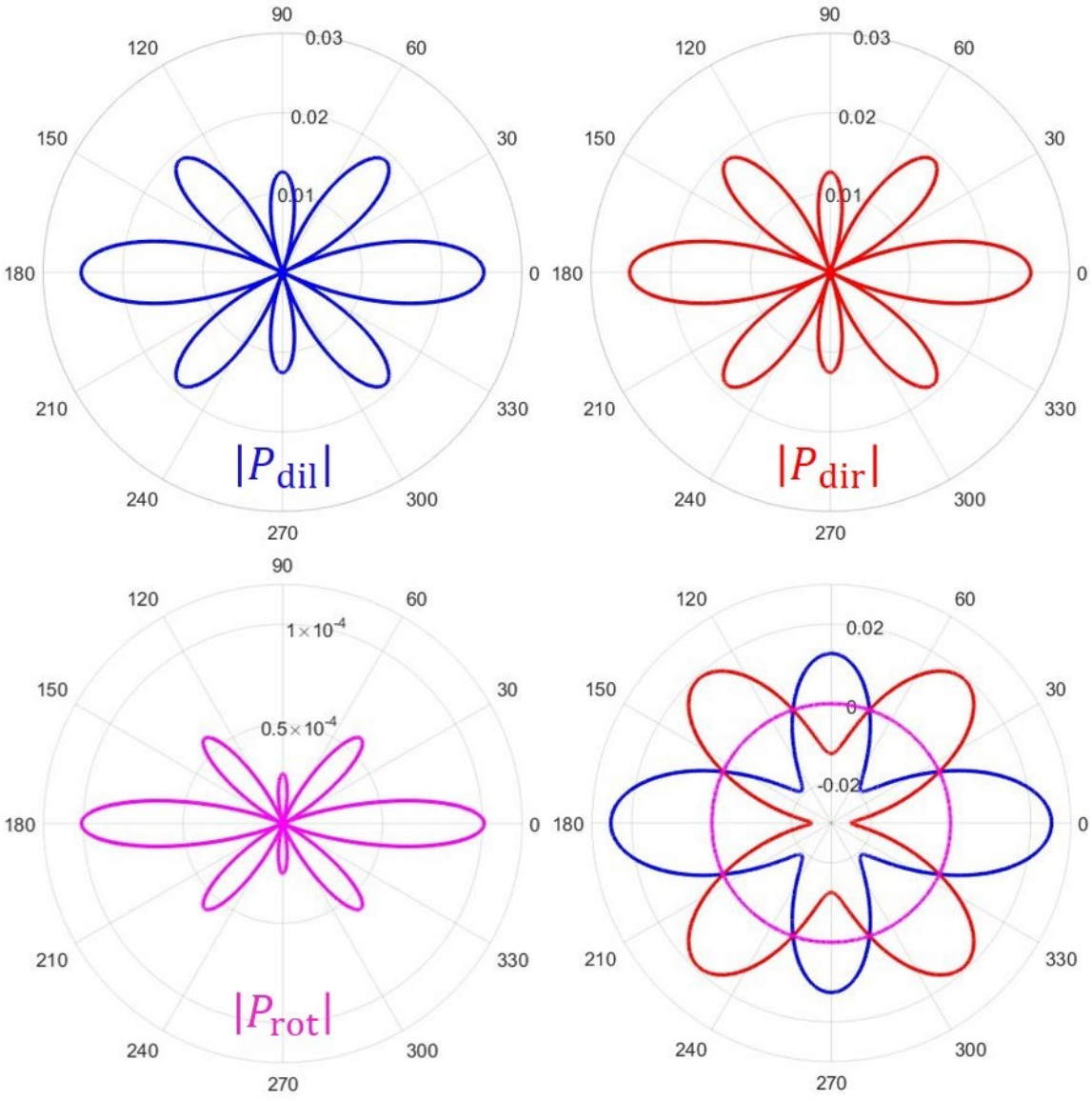

Figure 3–7: Capillary pressures visualized in polar plot where rotation angle $\theta = \phi - qx$. Blue, red and magenta paths represent dilation, director and rotation pressures, respectively. ($\mu_{2*} = -0.002$ and $\mu_{4*} = +0.0015$). The bottom right plot shows how the total capillary pressure vanishes (Eq. (3.19)).

to the real part of β. The complex capillary number also has a matrix form $\mathbf{B}$

$$\mathbf{B} = \Xi_{\parallel *}\mathbf{I} + \Xi_{\perp *}\mathbf{R} \tag{3.48}$$

where $\mathbf{I}$ is the identity matrix and $\mathbf{R}$ is the rotation matrix that appears in Eq. (3.18). The diagonalization of $\mathbf{B}$ contains its complex conjugate

$$\text{Diag}\mathbf{B} = \begin{bmatrix} \bar{\beta} & 0 \\ 0 & \beta \end{bmatrix} \tag{3.49}$$

We can easily link β, $\mathbf{B}$, Ξ and $\mathbf{T}_s$ by

$$\mathbf{B}\mathbf{B}^{\dagger} = \beta\bar{\beta}\mathbf{I} = \Xi^2\mathbf{I} = (\text{tr}\mathbf{T}_s^2)\mathbf{I} \tag{3.50}$$

Hence $\mathbf{B}/\Xi$ is a special unitary matrix$\in$ SU(2), while in Eq. (3.48), both $\mathbf{I}$ and $\mathbf{R}$ are special orthogonal matrices $\in$ SO(2). Latter we will show that $\mathbf{B}$ provides the same information as the mechano-geometry transformation matrix $\mathbf{Y}$ introduced in Sec. 3.5.2, that transforms the geometric frame $(\mathbf{t}, \mathbf{k})$ into the mechanical frame $(\boldsymbol{\Xi}, \mathbf{T}_v)$, shown in Fig. 3–1.

According to classical mechanics of 2-D surfaces with 2-D stress components, the typical Lamé stress curve is an elliptical closed curve [26]. In our model with 2-D stresses we will show that the elliptical Lamé stress curves of classical mechanics may become Limaçon curves [42] according to the degree of surface wrinkling. For example, for a quartic anchoring model, plotting for an anchoring condition along the resonance curve gives an ellipse , but plotting these quantities for a condition of double wrinkling produces a closes curve with an intersection (see middle row of Fig. 3–11). Here we wish to establish a classification scheme based on winding

number W_p for these generalized Lamé stress curves that provides a direct connection with geometry.

To first show the genesis of Limaçon stress curves , we consider a special simple case of a quartic model with $\mu_2 = 0$, and the Lamé stress curve we find is:

$$\left[\frac{\Xi_{\parallel}^2}{\mu_{4*}^2} + \frac{16(\Xi_{\perp} - \gamma_0)^2}{\mu_{4*}^2}\right]^2 = 4\left[\frac{4(\Xi_{\perp} - \gamma_0)}{\mu_{4*}}\right]^3 \tag{3.51}$$

which an equation consistent with a Limaçon curve [42], and that we can compute numerically by using Eqs. (3.6, 3.7, 3.20) for arbitrary anchoring constants.

Since β represents a Limaçon stress curve in the complex plane it has a winding number W_p. The winding number W_p of a stress loop C with respect to a point p in the complex plane $\mathbb{C}^1$ is defined as

$$W_p = \frac{1}{2\pi i}\oint_C \frac{1}{z-p}dz \tag{3.52}$$

whose geometric meaning is the number of net loops around a point. This number can help us to identify the total waves of $h(x)$ within one period. W_p varies according to the position of p. We use W_p to refer to the possible maximum W_p a loop can have due to the variation of W_p.

In general β describes s a closed loop pattern with a certain winding number in parametric space Λ_{2n}. The more non-vanishing anchoring coefficients there are, the more complicated pattern β exhibits. Particularly, β degenerates to a simple Lamés stress ellipse in Λ_2 space.

The Limaçon curve defines the stress states as the surface wrinkles. Importantly, when the surface profile changes slope $(+-)$ or $(-+)$ the bending stress (Eq. (3.17))

Table 3–2: Three points where $\Xi_{\|} = 0$ (or bending stress)

No.	Reβ	Imβ
1	0	1
2	0	$1 + \mu_{2*} + \mu_{4*}$
3	0	$1 - r\mu_{2*} + r^2{\mu_{4*}}^2$

or real component of β vanishes. The Limaçon curve β shows that in Λ_4 has 3 critical points where $\frac{d\text{Re}\beta}{d\text{Im}\beta} = 0$, and they are summarized by Tab. 3–2. The Tab. 3–2 shows that zero bending stress corresponds to different normal (extensional) stresses, creating complex stress conditions along the surface.

Fig. 3–8 shows the maximum winding number as a function of the anchoring model order. The maximum winding number W_p is linearly related to the highest anchoring term in Eq. (3.1). β is expected to have a maximum winding number of n, and minimum winding number of 1 in Λ_{2n} space (neglect flat surface condition). For example, for $n = 2$, $W_p = 1$ has a simple stress ellipse with two bending stress extrema, while for $W_p = 2$, the extrema are shown in Tab. 3–2. In partial summary, in contrast to plotting pressure and stress spatial profiles, we condensed all mechanical information in polar pressure plots (Fig. 3–7) and in quantized winding numbers of stress curves as functions of only the anchoring order model (Fig. 3–8).

Winding Number Landscapes in Higher Order Models

Here we generalize winding number results for $n = 3$. From Fig. 3–8, it is possible to have $W_p = 2$ in Λ_4 and $W_p = 3$ in Λ_6. If we write $\boldsymbol{\mu} = [\mu_2\ \mu_4\ \mu_6]$, the

[2] r is the anchoring ratio defined by $\frac{\mu_2}{2\mu_4}$

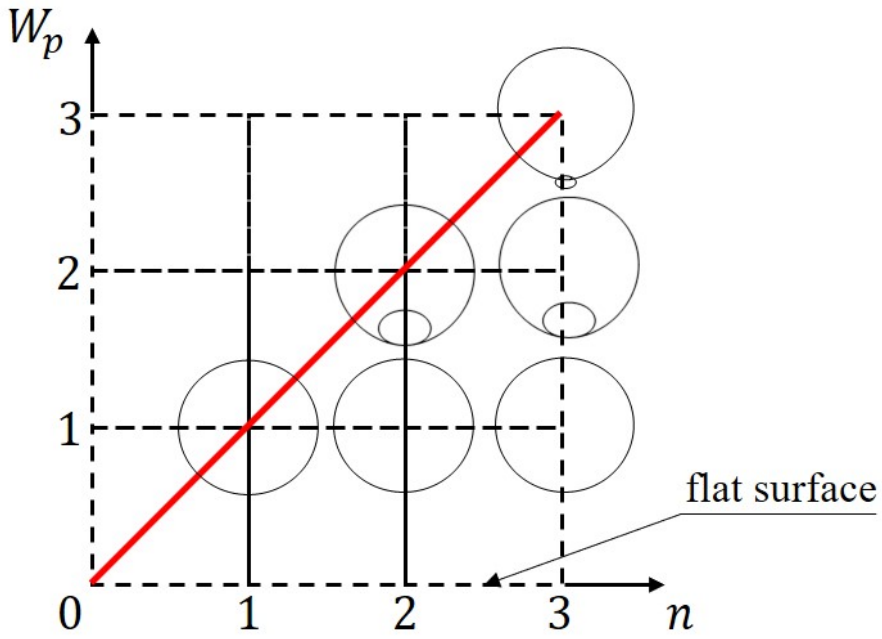

Figure 3–8: Maximum winding number W_p as a function of the highest anchoring model order n and Limaçon curves. All the possible patterns are limited between a flat surface and red line. For example, for the quartic model, the possible winding numbers of the stress loops are 1 and 2, which corresponds to single and double wrinkling in Fig. 3–3.

components of $\boldsymbol{\mu}$ span a 3-D space, which is the parametric space Λ_6. For simplicity, we use an ordered triplet $(\pm\pm\pm)$ to represent the sign of each anchoring coefficient. We found that only $(+-+)$ and $(-+-)$ quadrants allow us to have $W_p = 3$. Λ_6 also shows central symmetry, so we only need to evaluate the $(+-+)$ quadrant, shown in Fig. 3–9, together with the relevant planes quoted below.

The following surfaces serve as characteristic surfaces such that they are the boundaries to categorize different wrinkling regions of Λ_6.

$$\mathfrak{X} : \mu_4^2 = 3\mu_2\mu_6$$

$$\mathfrak{I} : -3\mu_6 = \mu_4$$

$$\mathfrak{S} : -3\mu_6 = \mu_2 + 2\mu_4$$

In Fig. 3–9, only the region between $\mathfrak{S}$ and $\mathfrak{X}$ allows $W_p = 3$. We can observe from Fig. 3–9 that in the region where $W_p = 3$, there exists one loop that is way more bigger than the other two. That loop is so big such that it is impossible to adjust μ to force three loops overlap. This phenomenon actually implies that we can never get 6 identical waves within one period in Λ_6. The details of this derivation are in Appendix 3.E. This important result on generalized models shows that higher harmonics can at most create only hierarchical effects, such as small ripples on larger scales wrinkling.

3.5 Mechano-Geometry of Wrinkling

In this section we synthesize the relationships between mechanics (capillary pressures, capillary vectors, winding numbers) and geometry (surface relief, curvature)

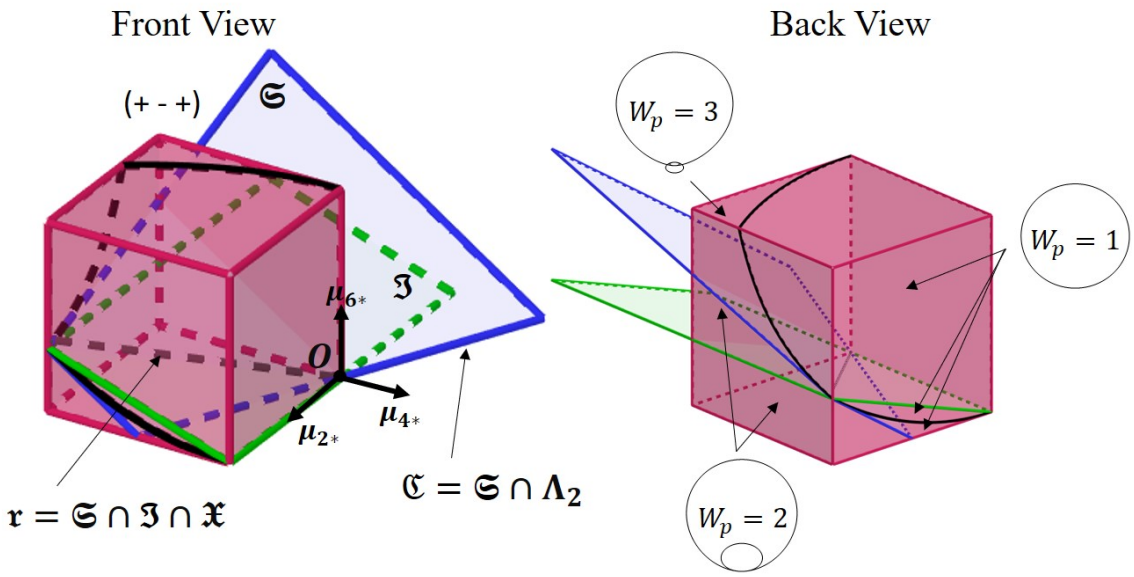

Figure 3–9: High winding number stress loops in the anchoring space for the sextic anchoring model ($n = 3$). Front view and back view of a subspace $(+-+)$ within Λ_6 where $W_p = 3$ is possible; the signs corresponds to the three anchoring coefficients of the $n = 3$ model. $W_p = 3$ can only be found in the region sandwiched in the middle of $\mathfrak{S}$ and $\mathfrak{X}$. The Limaçon stress curves for $W_p = 1, 2, 3$ are shown on the right back view figure. The figure was computed using the intersections of $\mathfrak{S}$, $\mathfrak{I}$, and $\mathfrak{X}$ (see text and Appendix 3.E).

using methods that lead to scaling relations and invariant that indicates surface property.

3.5.1 Capillary Pressures - Geometry Relation

We find that linearized capillary pressures (see Eq. (3.45)) are dependent on curvature according to this relations:

$$\tilde{P}_{\text{dil}} = -\tilde{\kappa},\ \tilde{P}_{\text{rot}} = -\frac{\tilde{\kappa}^2}{q} \text{ and } \tilde{P}_{\text{dir}} = \tilde{\kappa} + \frac{\tilde{\kappa}^2}{q} \tag{3.53}$$

If we plot the three capillary pressures as a function of curvature, Eq. (3.53) indicates that there exist three parameter-free universal curves. In each plot, μ_2 and μ_4 only affect the arc-length of these curves (starting and end points). Only the arc-length of $P_{\text{dil}} - \kappa$ curve is linear while the others are not. Generally, the span of curvature is dependent to anchoring coefficients, and ideally linear to $1/P_0$. This finding has an intuitive explanation. Consider the situation where P_0 is doubled while maintaining the same anchoring condition, the span of curvature should reduce to half. A numerical validation and details of discussion of Eq. (3.53) are given by previous work [12]. Eq. (3.53) encapsulates the symmetry relations shown in Sec. 3.3.1. If we change the sign of the chirality (q) the only way to accommodate this change is through a mirror symmetry along the $x-$axis. As mentioned above, chiral dopants control surface relief features such as skewness.

From Fig. 3–7, we can observe that winding number W_p and the absolute value of dilation pressure $|P_{\text{dil}}|$ are linked by: number of petal lobes $= 4 \times W_p$. This relation can be easily found through $P_{\text{dil}} = \kappa\gamma$.

3.5.2 Capillary Vectors - Geometry Relation

The wrinkling geometry and wrinkling mechanics are strongly connected. To reveal that link, we will first give a detailed explanation of how mechanics and geometry are linked for a special non-trivial condition where we only have one non-vanishing anchoring coefficient μ_2. Then we generalize the conclusion to n non-vanishing anchoring coefficients model. In the end of this sub-section, a mechano-geometry transformation matrix will serve as a summary to the mechano-geometry relation.

Special Condition: Quartic Model with $\mu_4 = 0$

If $\mu_4 = 0$ in the quartic model we obtain the quadratic model and the surface pattern is a single wavelength sinusoidal profile (see Fig. 3–3). The director pressure expression (Eq. (3.45)) is a contraction of symmetric tensors:

$$P_{\text{dir}} = \mu_{2*}\left(\mathbf{n}\otimes\frac{\partial\mathbf{n}}{\partial s}+\frac{\partial\mathbf{n}}{\partial s}\otimes\mathbf{n}\right):(\mathbf{tk}+\mathbf{kt}) \tag{3.54}$$

Eq. (3.54) indicates that the driving force is symmetric, hence a symmetric structure with vanishing skewness, $Rsk = 0$ should be generated. Under this condition, β degenerates to a Lamé ellipse and satisfy

$$\left(\frac{\text{Im}\beta-\mathcal{C}_0}{\frac{1}{2}\mu_{2*}}\right)^2+\left(\frac{\text{Re}\beta}{\mu_{2*}}\right)^2=1 \tag{3.55}$$

where $\mathcal{C}_0 = 1+\frac{1}{2}\mu_{2*}$. There is an analogy to a linear force field with center $\mathcal{C}_0 i$, which is the dynamically stable point. A linear force field acting on β obeys dynamic equation (parametrized by t)

$$\frac{d^2\beta}{dt^2}=-(\beta-\mathcal{C}_0 i) \tag{3.56}$$

whose solution $\beta = \frac{3}{4}\mu_{2*}e^{it} + \frac{1}{4}\mu_{2*}e^{-it} + \mathcal{C}_0 i$ is equivalent to Eq. (3.55). This analogy implies that $\mathcal{C}_0$ can be seen as an attracting point in the system. This important linear force field analogy encourages us to consider β in the general case as a linear combination of different components, based on the principle of superposition.

Another identity under the condition of $\mu_4 = 0$ that has been found is that surface normal angle ϕ can be written analytically as a function of $\Xi_{\|}$ only by (see Appendix 3.F for derivation)

$$\begin{aligned} \phi^{+} =& \frac{\pi}{2} + 2\arcsin\frac{\Xi_{\|}}{\mu_2} - \frac{2(2+\mu_{2*})}{\sqrt{1+\mu_{2*}}}\arctan\left[\frac{1}{\sqrt{1+\mu_{2*}}}\tan\left(\frac{1}{2}\arcsin\frac{\Xi_{\|}}{\mu_2}\right)\right] \\ \text{or } \phi^{-} =& \frac{\pi}{2} - 2\arcsin\frac{\Xi_{\|}}{\mu_2} - \frac{2(2+\mu_{2*})}{\sqrt{1+\mu_{2*}}}\arctan\left[\frac{1}{\sqrt{1+\mu_{2*}}}\cot\left(\frac{1}{2}\arcsin\frac{\Xi_{\|}}{\mu_2}\right)\right] \end{aligned} \tag{3.57}$$

where ϕ^{+} applies when $\gamma > \gamma_0$ and ϕ^{-} applies when $\gamma < \gamma_0$. Eq. (3.57) clearly demonstrates that as the normal angle oscillates back and forth around $\pi/2$, the bending stress oscillates around zero. The normal stress is not the source of oscillation.

Higher Order Anchoring Models

Similar analysis applies when $\mu_4 \neq 0$ (two loops in the β curve) in quartic model too. μ_2 and μ_4 serve as two dynamic attracting points in the system such that the surface wrinkles, β rotates (in specific sense) around them and form a Limaçon curve. The physical demonstration of the superposition principle is the two-wavelength surface profile. The net effect, represented by their mean value $\hat{\mu}_* = \frac{1}{2}(\mu_{2*} + \mu_{4*})$, always attracts β to generate exactly $W_p = 1$ loop such that

$$\frac{1}{2\pi i}\oint_{\Xi}\frac{1}{\beta - \hat{\mu}_*}\,d\beta = 1 \tag{3.58}$$

Generally, if the surface energy satisfies Eq. (3.1), then β is a summation of n sub-β such that $\beta = \sum_{j=1}^{n} \beta_{2j}$ where each β_{2j} is a closed path described by

$$(\mathrm{Re}\beta_{2j})^2 = (2j\mu_{2j*})^2 \left(\frac{\mathrm{Im}\beta_{2j}}{\mu_{2j*}}\right)^{2-\frac{1}{j}} \left[1 - \left(\frac{\mathrm{Im}\beta_{2j}}{\mu_{2j*}}\right)^{\frac{1}{j}}\right] \tag{3.59}$$

where $\mathrm{Im}\beta_{2j}$ takes the value between 0 and μ_{2j*}.

Another important parameter to measure is the portion of each component in β. We define $u = \mathrm{Re}(\beta)/\mathrm{Im}(\beta)$. It can be verified that u links capillary vector and surface energy by $\Xi = \gamma\sqrt{1+u^2}$. We choose u to represent mechanics. First, it is a real scalar instead of a complex number β or vector $\mathbf{\Xi}$. The main consideration is that we are expected to discuss the topology of the figure indicating the relationship between mechanics and geometry. Hence, the absolute value of h is less important than its curvature. Similarly, u, which erased the magnitude effect brought by isotropic tension γ_0, is a better parameter to represent mechanics. Notice that there is a natural invariant point in $\kappa - u$ plot where $\kappa = 2q\mu_{2*}$ and $u = 0$.

We use eight representative points whose locations are given by Fig. 3–10 to evaluate mechano-geometry relations. We compare $h - x$ pattern (left lower inset), the winding pattern of β in $\mathbb{C}^1$ (middle inset shown as imaginary i versus real $\mathbb{R}$ components of β) and $\kappa - u$ (right inset) in $\mathbb{R}^2$. They represent geometry, mechanics, and mechano-geometry relations, respectively. Numerical results are shown in Fig. 3–11. The numbers 1-8 correspond to anchoring conditions shown in Fig. 3–10.

To avoid ambiguities, the following content are discussed within one period only, unless otherwise specified. Firstly, both β and $\kappa - u$ are closed curves, corresponding to the fact that surface relief pattern is periodic. Another conclusion we draw is that

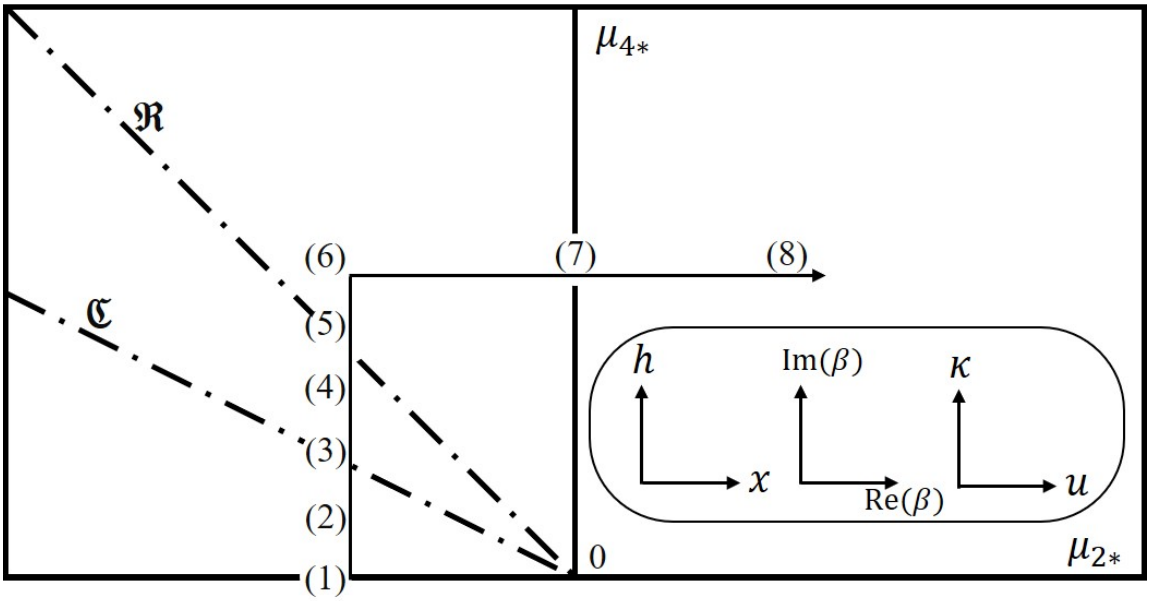

Figure 3–10: The first and second quadrant of Λ_4. $\mathfrak{R}$ is the resonance line while $\mathfrak{C}$ is the critical line. (1) to (8) are eight points chosen for further discussion in Fig. 3–11 and Fig. 3–12 to relate geometry ($h(x)$), mechanics (imaginary part of β as a function of its real $\mathbb{R}$ part) and mechano-geometry (curvature κ as a function of stress ratio $u = \mathrm{Re}(\beta)/\mathrm{Im}(\beta)$).

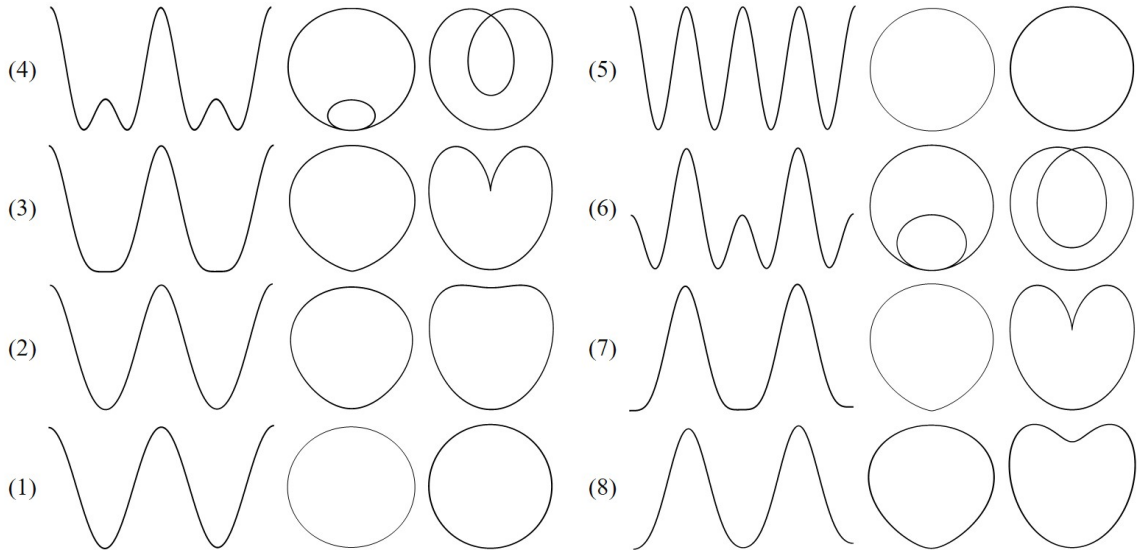

Figure 3–11: The comparison of $h-x$ (geometry), β (mechanics) and $\kappa-u$ (mechano-geo relationship), for eight (1-8) conditions indentified in Fig. 3–10. In (1-4) the left column is h, the middle is β and on the right we find $\kappa - u$; the same applies to (5-8). In (4) we see that double wrinkling corresponds to inner loops (crossings) in stress and curvatures-stress loops.

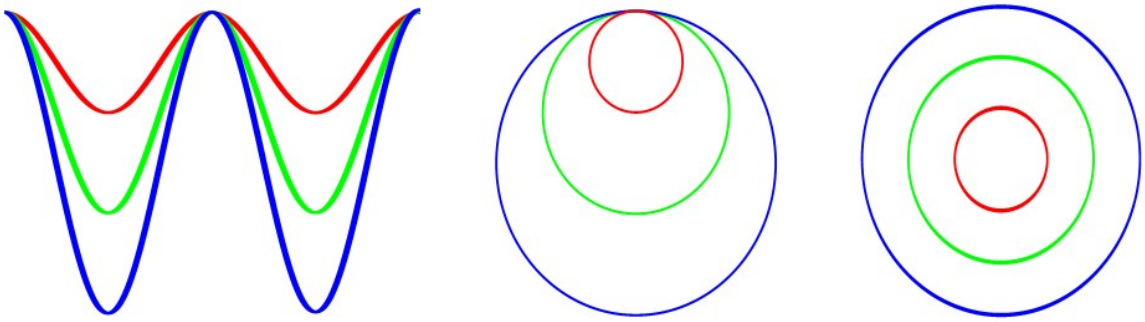

Figure 3–12: Magnitudes of surface profile $h(x)$ (left), Lamé stress curve β (middle) and curvature-stress ratio loop $\kappa - u$ (right) and how they change along the resonance line $\mathfrak{R}$ while maintaining their topology ($3 \times \mu_{\text{Red}} = 2 \times \mu_{\text{Green}} = \mu_{\text{Blue}}$). Moving radially in the anchoring diagram (Fig. 3–10) only changes amplitudes. This figure only shows half the period $P_0/2$.

the number of wavelengths in the $h - x$ profile is exactly the winding number W_p of β and $\kappa - u$ loops. A generalized proposition holds: the number of peaks (or valleys) equals $2 \times W_p$. We may find a contradiction that condition (5) (lying along the resonance line $\mathfrak{R}$) does not match this proposition from observing Fig. 3–11 at first glance, since the number of winding for β and $\kappa - u$ is 1, instead of 2 corresponding to 4 peaks in $h - x$ profile. Nevertheless even if this contradiction seems true, we just need to modify the proposition to: W_p of $\beta : [0, 1] \to \mathbb{C}$ is half of the peaks in the surface relief. If we move along s on the $h - x$ profile, β actually rotates twice under condition (5) by Eq. (3.52). The two crossings overlap since they are identical. These two identical crossings is the reason why 4 peaks are identical along $\mathfrak{R}$ in Λ_4.

Point (3) and (7) demonstrate another special condition. What we observed from β and $\kappa - u$ paths is that those paths have an apparent sharp point (actually it is smooth). It reminds us that the two plateau area (actually not flat) shown in $h - x$ profile too. It can be verified that this sharp point in β or $\kappa - u$ paths corresponds

to the 2 plateau areas in $h-x$ profile. If we observe β from (2) to (4), (3) is exactly the point when the emergence of a crossing starts to appear from a smooth path. If we observe $h-x$ in the same way, we find that (3) is exactly the point when $h-x$ starts to generate another small wrinkling structure.

If we are moving along $\mathfrak{R}$, $h-x$, β and $\kappa-u$ should only change magnitudes rather than topology. This is demonstrated by Fig. 3–12. An interesting phenomenon is that there is an invariant point for β while for $\kappa-u$ the path changes proportional with respect to its central point. The invariant point in β is $\mathrm{Re}\beta=0$ and $\mathrm{Im}\beta=1$ as discussed in Tab. 3–2. But for u, the invariant has been erased.

We can extend our discussion to arrive at a general result. Recall that $\tilde{h}=\sum_{j=1}^{n}\tilde{h}_{2j}$ where $\tilde{h}_{2j}=\frac{1}{q}\mu_{2j*}\sin^{2j}qx$, and $\beta=\sum_{j=1}^{n}\beta_{2j}$. A surface relief can be seen as a superposition of sub-relief $\tilde{h}_{2j}$, where each one is dependent on μ_{2j*}. Similarly, β can be seen as the summation of sub-beta β_{2j}. We bring another structure to the h profile and β topology each time we add another non-vanishing anchoring coefficient μ_{2j*}. Each pattern of surface relief has an inverse pattern (just switch the sign of $\boldsymbol{\mu}$ or P_0, as shown in Sec. 3.3.1) and they add pointwise to flat surface (where $\boldsymbol{\mu}=\mathbf{0}$). For β, we assign a direction to the path such we define the positive direction to be the trend of the movement of $(\boldsymbol{\Xi}_{\parallel},\boldsymbol{\Xi}_{\perp})$ when x is increasing in $h(x)$. We also assign the starting point as the point where $x=0$ ($\beta=i$ at this point). If we switch the sign of $\boldsymbol{\mu}$ or P_0, we won't reverse the direction of β. However, we reverse the velocity to this point. The reversed β and the original one can add to zero too (where $\boldsymbol{\mu}=\mathbf{0}$, see the bottom left figure of Fig. 3–14).

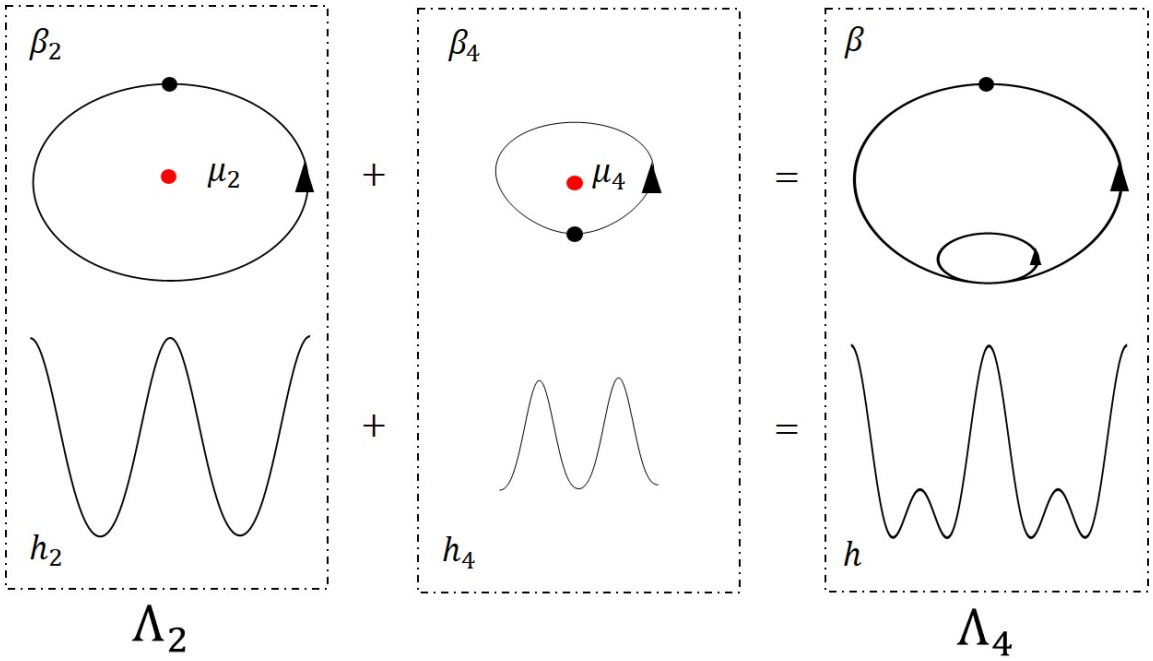

Figure 3–13: A sketch explaining how $h(x)$ and β can be seen as a direct superposition of their components in quartic model. Here, red point represents the attracting point introduced by each anchoring coefficient. Black point represents the starting point, which is also the point where β_2 and β_4 are glued together.

We use a quartic model in Fig. 3–13 to demonstrate this fact. The surface pattern and β in Λ_4 can be seen as a direct superposition of that in Λ_2, and that brought by μ_4. Previously we have shown that 2-wavelength pattern can only be found in certain area in the second and fourth quadrant (see Fig. 3–3). Now we can explain this phenomenon easily with Fig. 3–13. In those two quadrants, μ_2 and μ_4 have the opposite sign. They assign opposite starting velocity to the β_2 and β_4 path with same starting point ($\beta = i$ at this point). Hence, the net result is when two starting points glued together and satisfy the algebra such that the imaginary part and real part are added separately. Fig. 3–14 shows a summary of stress loops superposition and the resulting Limaçons, corresponding to five conditions of Fig. 3–10. The underlying phenomena are:

Condition (2), $|\mu_{4*}| < |\frac{1}{2}\mu_{2*}|$: The magnitude of μ_4 is too small to generate another loop. W_p still remains at 1 due to μ_{2*};

Condition (3), $|\mu_{4*}| = |\frac{1}{2}\mu_{2*}|$: This condition corresponding to critical line, β_4 generated by μ_{4*} is larger, and is the critical point across which β exhibits a jump from $W_p = 1$ to $W_p = 2$;

Condition (4): $|\frac{1}{2}\mu_{2*}| < |\mu_{4*}| < |\mu_{2*}|$: The effect of μ_{4*} becomes greater enough to generate another loop, thus $W_p = 2$. And this small loop corresponds to μ_{4*};

Condition (5), $|\mu_{4*}| = |\mu_{2*}|$: The small loop created by μ_{4*} increases and now is able to overlap with the big loop generated by μ_{2*}, so $W_p = 2$;

Condition (6), $|\mu_{4*}| > |\mu_{2*}|$: The effect brought by μ_4 is so large such that the role between μ_{2*} and μ_{4*} exchanges. If we fix the invariant point in μ_{2*}, then in order to increase the μ_{4*} loop, the final result must be the case shown as (6) in Fig. 3–14,

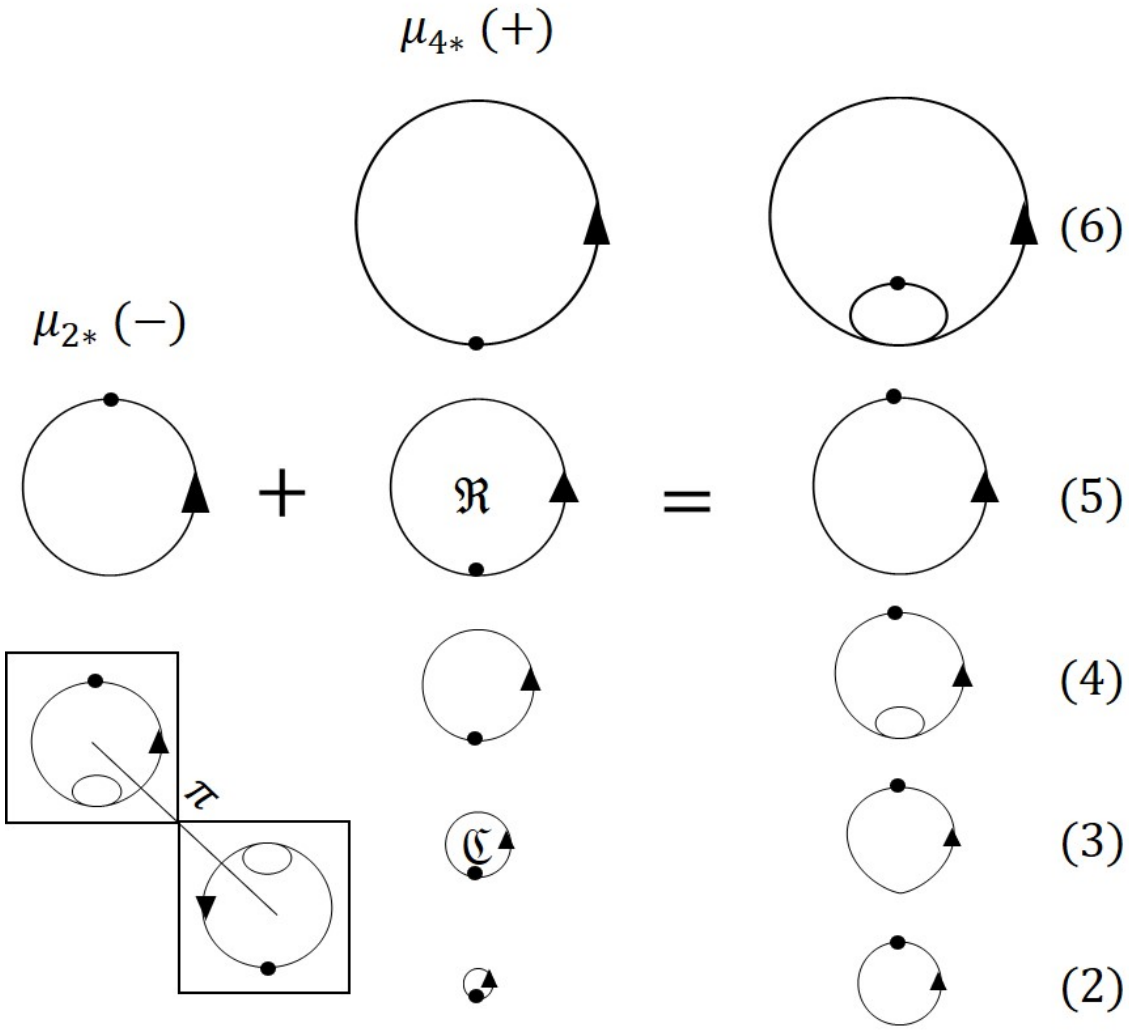

Figure 3–14: Stress loop superposition and resulting Limaçon curves. A summary of how five conditions of β_2 and β_4 in the second quadrant of Λ_4. The number on the right represents its corresponding position in Fig. 3–10. And the black point on the loop represents the starting point, which is the first invariant point in Tab. 3–2, and the point where β_2 and β_4 are glued together. The subfigure on the bottom left represents how the π rotation symmetric point (fourth quadrant) behave.

where the starting point now moved to the smaller loop. Hence, if we observe (4) and (6), the only difference is where the starting point is, so the surface profiles $h(x)$ for (4) and (5) are just a phase shift apart.

In the first and third quadrant, μ_2 and μ_4 assign same starting points to β paths, therefore the net effect is just a larger Lamé curve instead of creating a two wave-length surface pattern. The third and fourth quadrant are symmetric to the first and second quadrant, thus can be analyzed by similar way. In the bottom left subfigure of Fig. 3–14, we can see that the symmetric point on the fourth quadrant with respect to that on the second quadrant corresponds to a β curve which is also a π rotation with respect to that of the second quadrant, while maintaining the same winding number. What is more, winding number does not change its sign when we are moving on Λ_4, and this will be explained in Appendix 3.E.

A more mathematical statement, that confirms the numerical results of Fig. 3–11, is that from the Abelian group of surface patterns $h(x)$ (geometry) with operation $+$ to the Abelian group of complex capillary vector parameter β (mechanics) with directed loop addition, there is a map $Y(h \to \beta)$ which preserves group structure. This map $Y(h \to \beta)$ is called a homomorphism, and is the fundamental mechano-geometry relation of this paper.

In partial summary, we established a link between the topology of the Lamé stress curves and the geometric surface relief and used superposition principles to explain the generation of double wrinkling by taking into account the circulation direction in the stress loops. The mathematical homeomorphism result finds direct applications when assigning stress fields to wrinkled surfaces.

Matrix Representation of Mechano-Geometry Relation

Since a rotation matrix $\mathbf{R}(a)$ transforms a vector counterclockwise by angle of a and can be expressed by

$$\mathbf{R}(a) = \begin{bmatrix} \cos a & \sin a \\ -\sin a & \cos a \end{bmatrix} \tag{3.60}$$

The special rotation matrix $\mathbf{R} = \mathbf{tk} - \mathbf{kt}$ we introduced in Eq. (3.18) is just $\mathbf{R}(\frac{\pi}{2})$. Rewriting the Cahn-Hoffman capillary vector and stress vector in matrix form we have

$$\begin{bmatrix} \boldsymbol{\Xi} & \mathbf{T}_v \end{bmatrix} = \begin{bmatrix} \mathbf{k} & \mathbf{t} \end{bmatrix} \cdot \underbrace{\begin{bmatrix} \gamma & \partial_\theta \gamma \\ -\partial_\theta \gamma & \gamma \end{bmatrix}}_{\mathbf{Y}} \tag{3.61}$$

where the Jacobian transformation matrix $\mathbf{Y}$ contains the information of both mechanics (γ) and geometry (∂_θ). $[\mathbf{k}\ \mathbf{t}]$ represents pure geometry, and $[\boldsymbol{\Xi}\ \mathbf{T}_v]$ represents pure mechanics. Hence, $\mathbf{Y}$ is a matrix representation of this mechano-geometry relation. An observation from Eq.(3.60) and Eq. (3.61) yields the following identity

$$\mathbf{Y} = \gamma\sqrt{1+u^2}\mathbf{R}(\operatorname{arccot} u) = \Xi\mathbf{R}(\operatorname{arccot} u) \tag{3.62}$$

This relation can be shown in Fig. 3–1. The area spun by $\mathbf{T}_v$ and $\boldsymbol{\Xi}$ is just a rotation of the area spun by $\mathbf{k}$ and $\mathbf{t}$ scaled by Ξ with angle $\operatorname{arccot} u$. Matrix $\mathbf{R}(a) \in \mathrm{SO}(2)$ and can be represented by

$$\mathrm{Diag}\mathbf{R}(a) = \begin{bmatrix} \cos a - i\sin a & 0 \\ 0 & \cos a + i \sin a \end{bmatrix} = \begin{bmatrix} \overline{e^{ia}} & 0 \\ 0 & e^{ia} \end{bmatrix} \tag{3.63}$$

which reminds us the matrix form $\mathbf{B}$ in Eq. (3.49) by observing the similarity between Eq. (3.49) and Eq. (3.63). Hence $\mathbf{Y}$ can also be decomposed in the similar way of $\mathbf{B}$

$$\mathbf{Y} = \gamma\mathbf{I} + \partial_\theta\gamma\mathbf{R} \tag{3.64}$$

Compare the decomposition of $\mathbf{Y}$ with Eq.(3.48), we found that $\mathbf{Y}$ and $\mathbf{B}$ provide the same information. The eigenvalues of $\mathbf{Y}$ is simply

$$\lambda_\pm = \underbrace{\gamma\sqrt{1+u^2}}_{\text{stretch}} \cdot \underbrace{[\cos(\operatorname{arccot} u) \pm i \sin(\operatorname{arccot} u)]}_{\text{rotation}} \tag{3.65}$$

with eigenvectors

$$\mathbf{V}_{\lambda_+} = \begin{bmatrix} i & 1 \end{bmatrix} t \text{ and } \mathbf{V}_{\lambda_-} = \begin{bmatrix} -i & 1 \end{bmatrix} t \tag{3.66}$$

where t is any non-vanishing real constant. Ξ is the Pfaffian of $\mathbf{Y}$. $\mathbf{Y}$ transforms geometry to mechanics, so $\mathbf{Y}^{-1}$ reverses this process. To ensure $\mathbf{Y}^{-1}$ exist, we need $\det\mathbf{Y} \neq 0$ which always holds due to $\gamma > 0$ and $u \geq 0$.

In partial summary, we show that a simple non-singular rotation-dilation Jacobian transformation matrix (Eq. (3.64)) incorporates the geometry/mechanics relations. In practice, fast matrix solvers can be used for any anchoring model order to find stresses from geometry and vice versa.

3.6 Conclusions

This paper presents a comprehensive formulation, analysis, and characterization of surface wrinkling in cholesteric liquid crystals, as precursors of the ubiquitous biological plywoods found in nature. The central focus of the paper is to establish all the possible links between wrinkling geometry and mechanical stresses methods that

emphasize scaling laws, topological invariants, and parameter-free generic features of geometry and mechanics. Details of the mathematical foundations were shifted to the appendices and whenever possible contact with real applications were made. For wrinkling to occur, the surface tension must be anisotropic, and generic anchoring models of increasing order were considered.

The shape equations for wrinkled cholesteric surfaces were developed using capillary pressure (Eq. (3.19)), capillary vector (Eq. (3.29)), and least action (Eq. (3.31)) models. They all converge to the same equation by emphasize different aspects of wrinkling, such as the fundamental role of director capillary pressure in causing wrinkling. Also the pendulum analogy (Sec. 3.2.3) common in capillary models is shown to exist in this anisotropic surfaces. Using linearization (Sec. 3.2.4), we find important insights to wrinkling geometry, geometric symmetry and chirality. Importantly we show how a change in the sign of the cholesteric pitch changes the surfaces. Since the motivation of the work is to eventually correlate geometry to optical, tribological, wetting, and cell growth functionalities, we characterized the moments of the surface geometry, in particular the arithmetic mean, kurtosis, and skewness, and obtained anchoring parameters relations that maximize or minimize these functions. In particular, for a quartic anchoring model we found that the applications important kurtosis-skewness curve is a universal parameter-free bifolium, whose extrema can be found by tuning anchoring (Fig. 3–6).

The wrinkling mechanics was characterized by polar capillary pressure plots that unequivocally show that dilation pressure is essentially balanced the driving director

pressure. Also we establish a connection with classical Lamé stress curves for materials with 2-D stresses. Introducing a complex capillary number whose real component is the negative of the bending stress and whose imaginary component is the normal (dilation) stress we find that our anchoring-driven wrinkling generates Limaçon stress loops that generalize the simpler Lame ellipses. The topological charge of this stress loop in terms of a winding number is found in terms of any anchoring model (Fig. 3–8). Equally important the maximim winding numbers reflects the bending stress landscape, since the higher it is the more sign changes we find in this important stress component. Finally synthesis all results in Fig. 3–11, establishing the connections between surface relief, Lamé stress loops, and curvature-stress ratio Limaçons. The mechano-geometry connections is shown to be a rotation-dilation Jacobian matrix whose spectral decomposition involve stress information.

Finally we synthesize the geometry, mechanics, mechano-geometry relations into a flow-chart that reveals their interconnections. At the center we find the surface tension γ and capillary vector $\mathbf{\Xi}$ and from these we valuate pressures, stresses, and curvature. Reflecting the various shape equation formulations we can find curvature κ in two different ways. Finally the surface relief h is found from curvature or in the linear approximation from anisotropic tension.

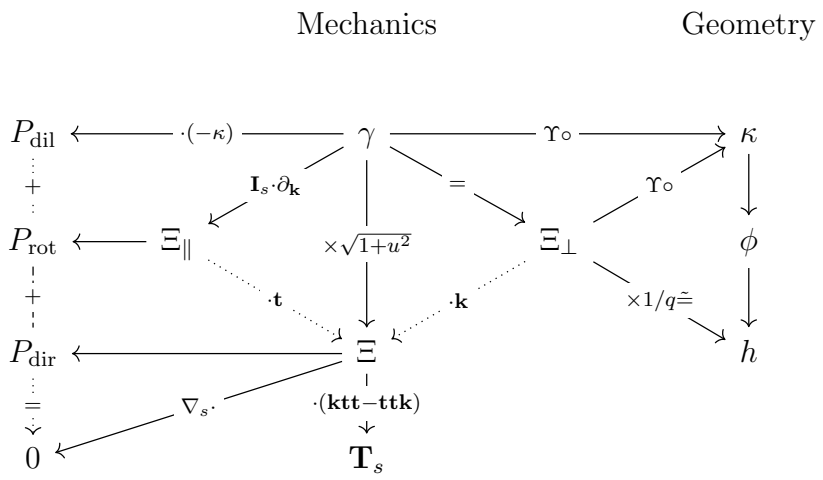

where $\tilde{\equiv}$ connecting two parameters represent that they are equivalent within linear region.

Taken together these results provide a comprehensive picture of surface wrinkling by anchoring mechanisms that can in the future be extended to 2-wave vector wrinkling, nematic and smectic liquid crystals, bulk elasticity corrections, transient emerging pattern formation, and active liquid crystals and chiral mass transfer [46, 47, 48, 49, 50].

REFERENCES

[1] P. J. Willcox, S. P. Gido, W. Muller, and D. L. Kaplan. Evidence of a cholesteric liquid crystalline phase in natural silk spinning processes. *Macromolecules*, 29:5106–5110, 1996.

[2] M. Mitov. Cholesteric liquid crystals in living matter. *Soft Matter*, 13:4176–4209, 2017.

[3] A. D. Rey. Liquid crystal models of biological materials and processes. *Soft Matter*, 6:3402–3429, 2010.

[4] A. P. C. Almeida, J. P. Canejo, S. N. Fernandes, C. Echeverria, P. L. Almeida, and M. H. Godinho. Cellulosebased biomimetics and their applications. *Adv. Mater.*, 30:1703655, 2018.

[5] N. Noroozi and D. Grecov. Numerical simulation of flow and structure in nematic liquid crystalline materials between eccentric cylinders. *J. Non-Newton Fluid*, 208:1–17, 2014.

[6] V. Sharma, M. Crne, J. O. Park, and M. Srinivasarao. Bouligand structures underlie circularly polarized iridescence of scarab beetles: A closer view. *Mater. Today: Proc.*, 1:161–171, 2014.

[7] F. Carrión, G. Martínez-Nicolás, P. Iglesias, J. Sanes, and M. Bermúdez. Liquid crystals in tribology. *Int. J. Mol. Sci.*, 10:4102–4115, 2009.

[8] B. Jerome. Surface effects and anchoring in liquid crystals. *Rep. Prog. Phys.*, 54:391–452, 1991.

[9] H. Yokoyama and H. A. van Sprang. A novel method for determining the anchoring energy function at a nematic liquid crystalwall interface from director distortions at high fields. *J. Appl. Phys.*, 57:4520–4526, 1985.

[10] A. D. Rey. Capillary models for liquid crystal fibers, membranes, films, and drops. *Soft Matter*, 3:1349–1368, 2007.

[11] P. Rofouie, Z. Wang, and A. D. Rey. Two-wavelength wrinkling patterns in helicoidal plywood surfaces: imprinting energy landscapes onto geometric landscapes. *Soft Matter*, 14:5180–5185, 2018.

[12] Z. Wang, P. Rofouie, and A. D. Rey. Surface anchoring effects on the formation of two-wavelength surface patterns in chiral liquid crystals. *Crystals*, 9:190, 2019.

[13] A. Cheong and A. D. Rey. Texture dependence of capillary instabilities in nematic liquid crystalline fibres. *Liquid Crystals*, 31:1271–1284, 2004.

[14] A. D. Rey. Line tension vector thermodynamics of anisotropic contact lines. *Phys. Rev. E*, 69:041707, 2004.

[15] A. Cheong and A. D. Rey. Cahn-hoffman capillarity vector thermodynamics for liquid crystal interfaces. *Phys. Rev. E*, 66:021704, 2002.

[16] D. W. Hoffman and J. W. Cahn. A vector thermodynamics for anisotropic surfaces. *Surf. Sci.*, 31:368–388, 1972.

[17] R. W. Ogden. Principal stress and strain trajectories in non-linear elastostatics. *Q. Appl. Math.*, 44:255–264, 1986.

[18] J. G. Ramsay and M. I. Huber. *The Techniques of Modern Structural Geology: Folds and Fractures*. Academic Press, 1987.

[19] Y. K. Murugesan, D. Pasini, and A. D. Rey. Defect textures in polygonal arrangements of cylindrical inclusions in cholesteric liquid crystal matrices. *Soft Matter*, 9:1054–1065, 2013.

[20] P. Rofouie, D. Pasini, and A. D. Rey. Nano-scale surface wrinkling in chiral liquid crystals and plant-based plywoods. *Soft Matter*, 11:1127–1139, 2015.

[21] P. Rofouie, D. Pasini, and A. D. Rey. Multiple-wavelength surface patterns in models of biological chiral liquid crystal membranes. *Soft Matter*, 13:541–545, 2017.

[22] B. Bhushan. *Modern Tribology Handbook*. CRC Press, 2001.

[23] P. Rajitrangson S.D. Cho, B. A. Matis, and J.A. Platt. Effect of er, cr: Ysgg laser, air abrasion, and silane application on repaired shear bond strength of composites. *Oper. Dent.*, 38:E58–E66, 2013.

[24] A. Riveiro, A. L. B. Maçon, J. del Val, R. Comesaa, and J. Pou. Laser surface texturing of polymers for biomedical applications. *Front. Phys.*, 6:16, 2018.

[25] M. F. Ayad, N. Z. Fahmy, and S. F. Rosenstiel. Effect of surface treatment on roughness and bond strength of a heat-pressed ceramic. *J. Prosthet. Dent.*, 99:123–130, 2008.

[26] W. K. Schief, A. Szereszewski, and C. Rogers. The lam equation in shell membrane theory. *J. Math. Phys.*, 48:073510, 2007.

[27] A. D. Rey. Marangoni flow in liquid crystal interfaces. *J. Chem. Phys.*, 110:9769–9770, 1999.

[28] P. Yue, J. J. Feng, C. Liu, and J. Shen. Interfacial forces and marangoni flow on a nematic drop retracting in an isotropic fluid. *J. Colloid Interface Sci.*, 290:281–288, 2005.

[29] R. Meister, H. Dumoulin, M.-A. Hallé, and P. Pieranski. The anchoring of a cholesteric liquid crystal at the free surface. *J. Phys. II*, 6:827–844, 1996.

[30] A. Rapini and M. Papoular. Distorsion d'une lamelle nématique sous champ magnétique conditions d'ancrage aux parois. *J. Phys. Colloq.*, 30:C454–C4–56, 1969.

[31] A. A. Sonin. *The Surface Physics of Liquid Crystals*. Gordon and Breach Publishers, 1995.

[32] I. W. Stewart. *The Static and Dynamic Continuum Theory of Liquid Crystals: A Mathematical Introduction*. CRC Press, 2003.

[33] A. D. Rey. Tension gradients and marangoni flows in nematic interfaces. *Phys. Rev. E*, 60:1077–1080, 1999.

[34] A. D. Rey. Viscoelastic theory for nematic interfaces. *Phys. Rev. E*, 61:1540–1549, 2000.

[35] A. D. Rey. Thermodynamics of soft anisotropic interfaces. *J. Chem. Phys.*, 120:2010–2019, 2004.

[36] A. D. Rey. Mechanical model for anisotropic curved interfaces with applications to surfactant-laden liquid-liquid crystal interfaces. *Langmuir*, 22:219–228, 2006.

[37] P. Rofouie, D. Pasini, and A. D. Rey. Tunable nano-wrinkling of chiral surfaces: Structure and diffraction optics. *J. Chem. Phys.*, 143:114701, 2015.

[38] A. D. Rey. Nematic contact lines and the neumann and young equations for liquid crystals. *J. Chem. Phys.*, 111:7675–7684, 1999.

[39] O. F. A. Gutierrez and A. D. Rey. Extracting shape from curvature evolution in moving surfaces. *Soft Matter*, 14:1465–1473, 2018.

[40] B. Bhushan. *Introduction to Tribology.* John Wiley Sons, 2013.

[41] J. R. Munkres. *Topology.* Pearson, 2017.

[42] E. V. Shikin. *Handbook and Atlas of Curves.* CRC Press, 1995.

[43] A. Urzica and S. Cretu. Simulation of the non-gaussian roughness with specified values for the high order moments. *J. Balk. Tribol. Assoc.*, 19:391–400, 2013.

[44] N. Tayebi and A. A. Polycarpou. Modeling the effect of skewness and kurtosis on the static friction coefficient of rough surfaces. *Tribol. Int.*, 37:491–505, 2004.

[45] D. K. Wainwright, G. V. Lauder, and J. C. Weaver. Imaging biological surface topographyin situandin vivo. *Methods Ecol. Evol.*, 8:1626–1638, 2017.

[46] M.G. Forest, P. Phuworawong, Q. Wang, and R. Zhou. Rheological signatures in limit cycle behaviour of dilute, active, polar liquid crystalline polymers in steady shear. *Phil. Trans. R. Soc. A*, 372, 2014.

[47] A. Sokolov, A. Mozaffari, R. Zhang, J. J. de Pablo, and A. Snezhko. Emergence of radial tree of bend stripes in active nematics. *Phys. Rev. X*, 9:031014, 2019.

[48] J. Zhao, U. Gulan, T. Horie, N. Ohmura, J. Han, C. Yang, J. Kong, S. Wang, and B. B. Xu. Advances in biological liquid crystals. *Small*, 15:1900019, 2019.

[49] H. R. Brand, H. Pleiner, and D. Svenek. Dissipative versus reversible contributions to macroscopic dynamics: the role of time-reversal symmetry and entropy production. *Rheol.*, 57:773–791, 2018.

[50] D. A. Beller, M. A. Gharbi, A. Honglawan, K. J. Stebe, S. Yang, and R. D. Kamien. Focal conic flower textures at curved interfaces. *Phys. Rev. X*, 3:041026, 2013.

CHAPTER 4
Conclusion

This thesis presents mathematical modelling, analysis, characterization and validation of the geometry and mechanics of surface wrinkling found in biological plywoods and cholesteric liquid crystals.

In Chapter 2, we presented a rigorous model based on nonlinear nemato-capillarity shape equation and its linear approximation. We discussed the role that three capillary pressures (dilation, rotation, and director pressure) play in wrinkling phenomenon also their relationships to surface curvature, from which we build the mechano-geometry relationship in terms of capillary pressures. Key discovery and contribution of this chapter are why and how the surface energy landscape is imprinted on the geometric landscape, such that more interaction energy harmonics lead to wrinkling of increasing complexity.

In Chapter 3 we investigate systematically higher-order wrinkling models intending to identify anchoring material parameter envelopes high the highest impact on geometric landscapes and mechanical fields through the use of scaling laws, complex analysis, and topological measures. We presented two complementary methods yielding the same shape equation. The linearization of these two methods also give the same linear model as the one we proposed in Chapter 2. We evaluated how the topology of the capillary complex number, which is defined through the capillary vector, affects the surface wrinkling patterns. We found that the winding number of the

capillary complex number is a very important invariant, which not only indicates the number of waves of surface profiles within one period in chirality, but also the petal lobes shown in the capillary pressures polar plot we discussed in Chapter 2. Hence, from this chapter, we build the mechano-geometry relationship in terms of capillary vectors, as well as mechano-mechanics relationship (between capillary pressures and capillary vectors).

In summary, we established a comprehensive mathematical model that allows us to describe, characterize and control surface geometry and surface mechanics. We also evaluated its linear approximation and found the essential link between geometry and mechanics. We concluded that the winding number of capillary complex number loop is the core concept from which we can categorize different surface wrinkling patterns, which are widely found throughout nature. This model shows three different perspectives discussed in Chapter 2 and 3, from which we can understand the capillary pressures, capillary vectors, energy, and surface stress tensor. At the same time, the symmetry properties of different parameters evaluated in parametric space serve as a simple mathematical tool for scientists who are investigating surface geometry and reveal the geometro-mechanics of biological plywoods and cholesteric liquid crystals.

Appendices

The appendices for this thesis are attached here or go to the next url: https://drive.google.com/file/d/0B126tJxvSoFdcmdoMkc5TzdaVVdubThxNjd3RXR5MXFzME5z/view